MULTISCALE INVESTIGATION OF THE COMPRESSION FAILURE IN LAMINATED CFRP COMPOSITES WITH AND WITHOUT Z-PIN REINFORCEMENTS

By

Alexander L. Faupel

Dissertation

Submitted to the Faculty of the

Graduate School of Vanderbilt University

in partial fulfillment of the requirements

for the degree of

DOCTOR OF PHILOSOPHY

in

Civil Engineering

August 9, 2024

Nashville, Tennessee

Approved:

Caglar Oskay, Ph.D.

Doug Adams, Ph.D.

Steve Clay, Ph.D.

Ravindra Duddu, Ph.D.

Haoxiang Luo, Ph.D.

Soli Deo gloria

ACKNOWLEDGMENTS

I would like to offer my sincerest gratitude to Dr. Caglar Oskay, who has consistently provided clear guidance as my research and academic adviser for the past 5 years. I have greatly benefited from his patient insistence on rigor and understanding in all of my work. He has been an honest mentor with whom I believe I have received the best training I could have asked for. I am grateful for the exciting, challenging, and rewarding projects we have undertaken, as well as the opportunities to present the work at professional conferences and in journal articles. I have become a better engineer and researcher because of my time at Vanderbilt and have gained confidence to tackle important problems related to computational mechanics and composite materials.

I also want to extend deep thanks to Dr. Stephen Clay at the Air Force Research Laboratory (AFRL) who has generously shared his time and expertise to improve the research presented in this dissertation, and serve on my doctoral committee as well. He has gone up and beyond required duties to provide abundant resources for experimental investigations and support for an internship at the AFRL. He helped me gain a well-rounded experience during my PhD training and aided me during my career search as well.

I am very grateful to Drs. Adams, Duddu, and Luo for serving on my doctoral committee. Through formal teaching, critical examination, and casual conversation they have helped me improve my knowledge-base, research outcomes, and communication skills. I am motivated by the standard of excellence they convey in their specific areas of expertise and the resulting high professional standing they hold among peers.

Beyond these advisers, I am grateful to many other people specifically at the AFRL and the FIRST laboratory who have put forth tremendous effort to help me. Most of all to Austin Land who besides performing experiments with the utmost attention to detail suffered my frequent phone calls, text messages, questions, and evolving requests. Phil Knoth, Wes Ault, Dewayne Gray, Tony McFall, Dustin Comer, Rick Polson, Jason Miller, Brian Smyers, and Vipul Ranatunga also supported the experimental campaigns which contribute so much to this dissertation. I would also like to thank James Ratcliffe at NASA Langley for helpful guidance on aspects of this work. These fellow engineers and technicians helped me generate meaningful information and gain valuable hands-on experience with composites-related fabrication, non-destructive inspection, and testing methods.

This dissertation process has been like an expedition and I am so thankful for the many family members and friends who are eager to see the fruit from the labor. Foremost, I am forever grateful to my wife, Ali, as she has loved me through long work days and celebrated achievements along the way. She has been my greatest encourager and always ensured that I had what I needed to put forth my best effort every day. The most grueling work days were made better because of phone calls, walks, or meals with her. Our son, Xander, was a welcome addition to our home in 2023 and he has been an extra encouragement to achieve

this milestone. Particular thanks are also due to my parents, Chris and Terri, who laid a foundation for this life path by providing for our family and encouraging me to pursue my interests as an engineer. My parents, along with my brother, Matt, have taught me to be inquisitive and strive for excellence. I am also thankful for refreshing times spent with the Martin and Stallings families as well as dear friends at Edgefield Church.

TABLE OF CONTENTS

LIST OF TABLES

LIST OF FIGURES

CHAPTER 1

Introduction

1.1 Motivation

Understanding how advanced composites behave under critical conditions is necessary for effective implementation of these materials in aerospace structures. Common design involves advanced laminated carbon-fiber reinforced polymer (CFRP) configurations that offer outstanding in-plane performance by tailoring layups of unidirectional plies for expected load conditions such as flight maneuvers or landing. Among the characteristics of CFRP laminates, compression strength is a critical weakness. Experimental results show compression strength in the longitudinal direction up to 40% less than tensile strength in unidirectional configurations [46, 168] and 15-35% less in multidirectional laminate configurations [175]. Experimental analyses indicate that the compression behavior of laminates is complicated due to the presence of multiple failure mechanisms which include kink banding, splitting, delamination, fiber cracking, fiber-matrix debonding, and matrix cracking [75, 130, 148, 149, 155, 156, 171], some of which interact during the loading process. The ultimate failure in multidirectional laminates is typically induced by the propagation of the dominant kink band across a 0 degree lamina [19, 22, 45, 163], but prominent splitting is also consistently observed prior to failure in notched specimens at the notches and within multiple laminae of different directions [19, 22, 45]. Matrix cracking and delaminations may additionally be present and have been observed connecting to kink bands [19, 22, 45].

Other complications may also be present in composites which are evaluated in order to meet airframe structural certification requirements. One such complication is the presence of existing regions of material failure, or damage, which can be hard to detect and weakens the structural response. Test conditions including compression-after-impact (CAI) are used to measure the residual strength of a damaged composite which aids the assessment of the damage tolerance of a laminate. Under CAI conditions, the interlaminar properties are a crucial weakness and associated with delamination-driven failure [57, 84, 161, 184] that primarily emanates from the pre-existing damage. Technologies proposed to arrest delamination growth and increase the CAI residual strength include through-thickness reinforcements. A form of through-thickness reinforcement called z-pinning is found to reduce the extent of delamination during compression loading and increase the residual CAI strength of an impacted composite sample by more than 50% in [135, 184]. While the influence of z-pins on residual strength is promising, delamination and other CAI failure mechanisms in the presence of z-pins are not yet fully understood.

It is crucial to understand the primary compression failure mechanisms in composites and have prediction tools to aid in the design of structures to meet damage tolerance objectives. Multiscale computational modeling is a class of advanced numerical approach which enables us to understand the failure process and interaction of mechanisms across size scales while taking advantage of computing resources. This dissertation presents multiscale investigations of the compression response of laminated CFRP composites with and without z-pins undertaken using state-of-the-art computational damage analysis models and experimental methods. Physics-based prediction of the composite response is accomplished by integrating state-of-the-art multiscale and cohesive zone models in finite element analyses. Experimental campaigns are used to support the development, calibration, and validation of the computational models. Damage progression predictions supplement experimental results and demonstrate advancements in modeling capabilities to predict compression failure in laminates with and without z-pins.

1.2 Literature Review

1.2.1 Compression Failure in Unidirectional Composites

Foundational experiments on compression behavior of CFRPs reveal some key features of kink band failure. Soutis et al. [148] report that in both notched and unnotched laminated plates with varying layups the compressive failure is linked to inelastic microbuckling in the longitudinal plies. In Kyriakides et al [97] and Vogler and Kyriakides [170] the importance of initial fiber misalignment (or "imperfection") amplitude on compressive strength is demonstrated. Moreover, it is observed that post-failure, deformation of the composite was localized into kink bands which formed at inclinations with respect to the longitudinal and transverse directions of the loading. The measurements for kink band width in carbon fiber reinforced plastics (CFRPs) are reported in the range of $5-40$ times the fiber diameter [97, 110, 143, 156, 173]. Moran et al. [110, 111] investigated the formation and propagation of kink bands in more detail, and reported the process of band broadening as the kink band propagates in graphite-thermoplastic composites (e.g. PEEK matrix material). The experimental imaging illustrates the kink band failure process to include excessive shear straining of the matrix material near the imperfection zone, fiber buckling, and tensile failure of buckled fibers forming the boundary of the kink band.

Further understanding of kink band formation and propagation has been derived from theoretical models. The general history for compressive strength prediction traces from Rosen's model [138] that considers the elastic buckling of adjacent fibers in phase with one another, "microbuckling", instigating deformation of the matrix material in shear. Argon's model [5] incorporated the local maximum initial fiber misalignment angle along with the in-plane shear strength of the matrix to predict compressive strength. More closely considering fiber rotation, Budiansky [32] incorporated the effect of fiber tensile failure and Budiansky and Fleck [33]

and Fleck et al. [66] improved upon these theories and presented an elastic-perfectly plastic model where the development of a physical kink band is linked to the nonlinear relationship between fiber longitudinal modulus, matrix shear strength, and fiber diameter.

The nonlinear analytical descriptions and sensitivities of the failure mechanism have been studied using mesomechanical approaches that resolve fiber and matrix materials and incorporate fiber waviness where the fiber orientation varies in a sinusoidal fashion along the composite longitudinal direction. Studies utilizing direct numerical simulations include Yerramalli and Waas [180] where the positive effect of fiber diameter - and thus bending stiffness, on the compressive strength is confirmed using a 3D finite element simulation of a small cylindrical section of composite material comprised of purely elastic fibers and J_2 theory of plasticity matrix behavior. Bishara et al. [27] performed analyses with a single 3D row of composite material modeled as linear elastic fibers that fail under normal tensile strain and an elastic-plastic matrix with isotropic hardening. Naya et al [115] also directly simulate fibers surrounded by a plastically behaving matrix but arranged according to a statistical distribution in a column-like domain and modeled with a commercial continuum damage code, additionally including cohesive-frictional interfaces between the fibers and matrix. The contributions of the microstructure and initial fiber misalignment angle to the kink band process are simulated in detail, however parametric studies are carried out using a simplified single fiber model to obtain compression strength and elastic modulus. Other simulation results link the experimentally observed stages of the kink band process to matrix yielding in areas of imperfection and indicate the effect of initial fiber waviness locality on compressive strength. Bergan et al. [20] present a model connecting fiber rotation with mesoscopic compression failure by incorporating kink band width predicted from a micromechanical simulation as an input parameter. This model requires numerical schemes such as element deletion to obtain a load drop indicative of material failure and accurately captures kink band kinematics.

Criterion-based compression failure models that are influenced by or account for kink banding have also been proposed. In Pinho et al. [129], where kink band failure in the ply occurs according to a bound of the longitudinal composite strength and geometry-dependent calculations of in-situ shear strengths. Camanho et al. [36] presented an invariant-based criterion in the frame of localized fiber waviness which claims local transverse failure of the matrix as compression kink band failure. Alternatively, Wilhelmsson et al. [174] predicted failure of the composite material in shear due to maximum "defect severity" utilizing observations in an experimental database. While criterion-based models idealize the consequences of kink bands in predicting failure at the macroscale, these models do not resolve the mesoscale mechanisms associated with kink banding.

1.2.2 Compression Failure in Multidirectional Laminates

Recent experimental studies shed some light into the compression failure interactions in laminated CFRP composites. Physical testing of compression specimens provided some understanding of the order of occurrence of failure mechanisms in composite laminates of varying layups and configurations. The ultimate failure is typically induced by the propagation of the dominant kink band across a 0 degree lamina [19, 22, 45, 162]. Prominent splitting is also consistently observed prior to failure in notched specimens at the notches and within multiple laminae of different directions [19, 22, 45]. Matrix cracking and delaminations are present and observed connecting to kink bands [19, 22, 45].

Several computational damage and failure analysis techniques have been employed to model failure mechanisms associated with the compression response of multidirectional CFRP composite laminates. Among the compression failure mechanisms, kink bands have been shown to strongly influence the compression strength of composites [97, 110, 143, 148, 156, 173]. Kink banding is an instability phenomenon [5, 33, 66, 97, 110, 111] and numerical studies suggest a strong link between fiber misalignment, mechanical properties of the constituent materials, and the resulting compression strength [60, 170, 180]. Modeling approaches for kink band failure span direct numerical simulations [27, 115, 180] that resolve the composite constituents at the mesoscale, continuum damage models that track fiber rotation and incorporate shear nonlinearity at the mesoscale [20, 21], multiscale modeling that concurrently evaluates failure processes in resolved materials microstructures across the macroscale domain [60], and models based on macroscale failure criteria by including effects of shear nonlinearity and pressure [129] or critical fiber misalignments [36, 174]. Other mechanisms (i.e., splitting, delamination, matrix cracking, and fiber-matrix debonding) are not unique to compression loading and are typically observed under other loading conditions as well [116, 133]). Fracture mechanics-based approaches such as cohesive zone modeling (CZM) [15, 20, 115, 163] and extended finite element method [53, 79], continuum damage mechanics [15, 37, 163], multiscale methods such as the eigenstrain based homogenization method [30, 31, 50, 51], multiscale discrete damage theory [123, 152, 153], and criterion-based failure models [36, 186], among others have been employed to study the aforementioned failure mechanisms. Fiber fracture is a consequence of the bending experienced in microbuckling and/or kink band formation [97] and has been included using strength [16, 36] or curvature criteria [60].

Recent computational investigations provide information on the interactions between the failure mechanisms throughout the loading process [22, 28, 132]. Prabahakar et al [132] investigated several unnotched laminate layup configurations. The onset of kink bands was predicted just prior to the ultimate load, whereas delaminations were predicted to fully form after kink band onset. This study also showed that increasing interlaminar shear strength results in delayed kink band initiation and increased laminate compression strength,

pointing to interaction between interlaminar damage state and kink band initiation. Bishara et al [28] investigated the progression of failure in unnotched $[+45/90/-45/0]_{2S}$ specimens. Delaminations were predicted to fully form early in the process at 90-45 degree ply interfaces near the edges of the specimen (at approximately 77% of the ultimate load). Kink bands initiated immediately prior to the ultimate load away from these delaminations. Matrix cracking in the 45 and 90 degree plies were also predicted post-ultimate load. Additional delaminations were predicted at the 0-90 and 0-45 degree ply interfaces connecting to the ends of the formed kink band. Bergan et al [22] studied the progression of damage in 3 different open-hole layups which exhibited 3 different effective stiffnesses. Initial splitting and matrix cracking are predicted around 75% of the respective ultimate load in all specimens, followed by kink band initiation around 97-99%. The early onset damage features exhibit differences in initial size and growth. Long initial splits were predicted in the stiffest laminate and are accompanied by a small amount of delamination prior to failure. In contrast, delaminations were predicted with size matching short splits prior to ultimate load in the least stiff laminate. The results of this investigation show variation of failure mechanism initiation time, initial size, and growth among specimens consisting of the same material. The aforementioned studies point to uncertainties in compression failure mechanism interactions and how these interactions influence overall compressive performance.

1.2.3 Delamination in the Presence of Z-pins

Experimental investigations in the literature show that z-pins enhance the delamination resistance of composite laminates [29, 43, 54, 72, 109, 125, 125–128, 134]. Interlaminar fracture properties reach much higher values in z-pinned laminates compared to unpinned laminates. Two topics that have been highly examined in published literature are: the ability of z-pins to bridge the interlaminar crack forming between ply surfaces, and the associated pull-out mechanism which results in energy dissipation. Additional damage mechanisms unique to interlaminar reinforcements like z-pins also include shearing and bending of the reinforcements as well as ploughing through material as sliding of adjacent plies takes place under Mode II conditions [42].

Examination of single-pins or pin-arrays in half-laminates show the influence of loading conditions (i.e. mode-mix), as well as the geometry and arrangement of the z-pinned laminate (i.e. layup, thickness, z-pin volume fraction and embedded length) on the mechanisms governing z-pin failure [29, 134, 179]. Other standardized interlaminar fracture (ILF) experimental configurations have been used to investigate the z-pinned interface failure mechanisms including Double Cantilever Beam (DCB) [29, 43, 54, 72, 109, 125, 125, 126, 134], End-notched Flexure (ENF) [43, 125, 127], End-Loaded Split [109], and Mixed-mode Bend (MMB) experiments [109, 128, 139]. These experiments show that the laminate interface failure in the presence of z-pins is nonlocal resistance from multiple pins contribute to the overall behavior as they are

engaged when the matrix delamination crack advances. The Mode I fracture toughening effects of z-pins are evident in DCB tests. As specimens are being opened and when the specimens have completely fractured, images show z-pins mostly intact after pulling out from one half of the test specimen [125, 126]. Images displaying z-pin conditions after ENF tests have been reported in Ref. [43, 126, 127] and show that Mode II loading results in z-pin failure involving interfacial debonding, splitting, and shear fracture.

The z-pin length that is embedded in the composite also has an effect on failure mechanisms. Under Mode II interlaminar loading, failure changes from only pull-out to partial-pull and shear fracture, and finally strict shear fracture with no pull-out as the embedded length of the z-pin is increased. While resisting in shear, the z-pins "plough" some of the substrate laminate material prior to failure. Under mixed-mode conditions (e.g., in MMB [128] or approximate shear [43] tests), the z-pin fibers are susceptible to fracture and splitting.

Much of the computational modeling research related to z-pinned composites focuses on interlaminar behavior with use of existing or novel interface element formulations that are employed to account for the effective behavior in the presence of z-pins. The formulations include cohesive zone models (CZM) [25, 26, 52, 107, 109, 134, 141], embedded finite elements [29], and continuum constitutive models [47]. The CZM framework was established for predicting the initiation and progression of delamination in composites under mixed-mode loading [39]. This capability incorporates material strength-based criteria for predicting the onset of delamination failure and fracture mechanics to predict delamination propagation. It is a commonly employed analysis tool for simulating delamination in composite structures with and without pre-existing delamination, and admits general interface constitutive laws expressed by traction-separation relationships. CZM is commonly implemented in a finite element model with continuum elements [25, 26, 52, 107, 109, 134] and rod-type elements [141] or discrete nonlinear springs [54]. The constitutive behavior is described by traction-separation laws (TSL) consisting of an initial linear elastic response followed by one or two stages of softening until interface failure, which includes bilinear [25, 26, 109, 134] or trilinear [52, 107, 141] forms. Some models use an average response [107, 141] for a given distribution of z-pins and the z-pin locations are not discretely accounted for while in other cases the model is assigned to elements matching the physical spatial distribution of z-pins in the laminate configuration [25, 26, 52, 54, 109, 134]. There may be one TSL [25, 26, 54, 134] or two TSLs [52, 109] at the same location to model the behavior of both matrix delamination and the effects of z-pins.

Existing methods to calibrate the CZMs assign constitutive law properties based on results from direct finite element simulations of z-pinned structures [25, 52, 181], analytical systems of equations describing the kinematics and kinetics of a single z-pin bridging two plies [26, 107, 109], flatwise-tension (FWT) or other single z-pin experimental configurations [1, 29, 134], and DCB tests [54, 134]. Direct numerical simulation can provide high fidelity predictions of the z-pin failure process and results can be used to derive

apparent interface properties. With this method, important effects such as thermal residual stresses at the z-pin - lamina interface behavior are included which play a dominant role in the onset of z-pin pullout as studied in Refs. [160, 181]. The drawbacks to direct numerical simulation include overcoming convergence issues with finite element simulations as reported in Ref. [52] and the computational cost associated with performing analyses over all possible loading scenarios. The analytical methods proposed in [1, 26] can also account for important behavior such as z-pin pullout, z-pin fracture, snubbing, and ploughing by calibrating parameters related to lamina response and z-pin - lamina interface frictional properties. The problems are solved numerically by incrementing applied displacements to find the overall mechanical response under every mode-mix of interest. One drawback is that matrix debonding has not been incorporated. The FWT and other single z-pin experimental results used in Refs. [1, 29, 134, 181] provide direct information on apparent z-pin crack bridging properties but do not include effects of the matrix interface. Though not standardized, the test equipment employed in Refs. [179, 181] allows studying z-pins under many mixed-mode conditions. The inherent structural response (as opposed to a material response) of z-pinned laminates under mixed-mode conditions has been studied with ILF experiments. Refs. [54, 134] propose using the area under the DCB load-displacement results curve to define the apparent interlaminar fracture toughness associated with one or more rows of z-pins. Analytical approaches to predict delamination resistance in DCB, ENF, and MMB z-pinned composite configurations are also proposed in Refs. [35, 105]. The proposed approaches add descriptions of z-pin bridging to the typical fracture mechanics derivation used to calculate fracture toughness in ILF experiments but are not verified by comparison to experimental results.

1.2.4 CAI in Z-Pinned Laminates

Multiple authors have performed experimental investigations to examine delamination in z-pinned laminates. Results from CAI analyses indicate that z-pins toughen the delamination response of laminates under CAI conditions [57, 135, 141, 184]. The studies focus on the CAI response of laminate plates with impact located on a rectangular array of z-pins, following standardized test methods [6, 7]. In these studies, z-pinned laminates of 4 and 6 mm thickness (32 and 48-ply layups) take longer to fail and reach higher strengths under identical impact and compressive load conditions compared to an unpinned sample [135, 184]. The failure process analyses in these studies are limited to qualitative observations - e.g., the z-pinned specimens are reported to exhibit reduced interface opening on the edges in Ref. [184]. One quantitative factor which is reported and related to the apparent strengthening of the z-pinned specimens is the size of impact damage area. The projected impact damage area measured using ultrasonic C-scans is considerably smaller in z-pinned specimens compared to unpinned specimens subjected to the same impact conditions in Refs. [67, 68, 135, 184]. CAI was also studied with impact located on unpinned material within a z-pinned

"frame" configuration in Ref. [135]. The CAI strength in this case was very similar to the unpinned configuration. Ref. [67, 68] conducted post-CAI damage analysis using X-ray images of 2.5 mm thick (8 ply layups). The images show a more localized transverse damage pattern in z-pinned specimens, although the strength is the same as the unpinned specimens subjected to identical impact and CAI loading conditions. The consistent strength between z-pinned and unpinned specimens is attributed to a tradeoff of weakened lamina properties and the Mode I fracture toughening effect of z-pins which restrict the separation of sublaminates which are susceptible to buckling [56, 137]. Lamina property weakening is due in large part to pins acting as a defect in the composite material - increasing fiber waviness and introducing resin pockets which alter the distribution of fibers in the ply [112]. Elastic and strength properties have been shown to depend on z-pin diameter, spacing, and placement. The longitudinal compression strength and modulus are up to 10% lower compared to unpinned [44, 112, 151, 176]. Flexural strength is approximately 20% lower than unpinned laminates in Ref. [44] while the flexural modulus was reported as unchanged.

Progressive damage analyses have been performed to better understand CAI failure and are reported in Refs. [15, 41, 71, 74, 101, 147, 154, 157, 158, 177]. The studies include many efforts to predict structural behavior of impacted but unreinforced laminates. There are multiple research areas related to the computational models used in the studies. These areas include the modeling of plies and interfaces, as well as the initial damage state. Due to the presence of delaminations at many plies and interfaces the problem is computationally challenging. Proposed techniques for representing plies includes using combinations of shell elements [71, 147, 157], continuum shell elements [15, 41, 101], and solid elements [74, 154, 157, 158, 177]. The interfaces in these investigations are modeled with CZM (continuum or contact surfaces). Many of the modeling approaches neglect or indirectly account for kink-band formation which is a dominant damage mechanism during compression failure of fibrous composites (see e.g., Refs. [86, 97, 156]) and also present in z-pinned composites [112, 151]. Impact damage has been incorporated by directly simulating the impact event using dynamic finite element analysis in Refs, [41, 101, 158]. Simulation of dynamic impact events in composites are known to exhibit complex phenomena such as wave dissipation and wave dispersion [80–82] as well as thermal effects [183] which could affect the overall damage state following the impact event. Another approach is to prescribe simplified damage patterns based on experimental observations and idealizing impact damage with elliptical or "peanut-shaped" debonded regions through the thickness [3, 15, 74, 119, 154]. A method to more precisely model the delaminations using ultrasonic C-scan or X-ray CT images without performing the impact simulation is also proposed in Ref. [59]. Due to the size of the CAI problem - which includes large deformation and material nonlinearities, explicit finite element simulations are performed using mass scaling to speed up the analysis compared to implicit simulations. Methods such as selective damage mapping [15] and adaptive introduction of CZM elements [87] have also

been proposed which can reduce the number of degrees of freedom in the analysis. The open literature does not include the computational analysis of CAI of z-pinned composite laminates, however there are investigations on structural configurations with z-pins including composite stringer-stiffener configurations without pre-existing delaminations in Refs. [2, 24, 64, 164].

1.3 Research Objectives

The overarching goal of this dissertation is to understand and predict the compression failure mechanisms in CFRP composites at different scales and in the presence of z-pin reinforcements using state-of-the-art multiscale computational models and experimental methods. The research objectives and underlying tasks to fulfill this goal are as follows:

1. Understand and predict compression kink band failure in composites of different scales
   (a) establish a reduced-order multiscale compression kink band model (KBM)
   (b) validate the KBM and study the interplay of kink bands with sub-critical failure mechanisms in an experimental specimen
2. Understand the compression-after-impact failure mechanisms in z-pinned composites
   (a) develop and calibrate an interface model for predicting delamination in the presence of z-pins
   (b) conduct experimental and computational studies on the damage arrestment capability of z-pinning under CAI conditions

1.4 Dissertation Organization

The details, results, and discussions of the tasks are organized into four additional chapters. Chapter 2 entails the development and verification of a reduced-order multiscale compression kink band model. The novel contribution of this model is the concurrent linking of microstructural behavior to the macroscopic strength prediction. Parametric studies show how physical properties such as fiber waviness and matrix constituent properties influence failure predictions.

The kink band model is validated and used to study the interplay of kink bands with sub-critical failure mechanisms in a computational-experimental analysis of a double-edge notched laminate configuration in Chapter 3. The experimental aspects of the analysis contribute new information on the compression failure process in a multidirectional laminate. The computational model is calibrated using additional experiments, and damage progression is predicted to match the experimental results while highlighting the importance of splitting and matrix cracking on the nucleation, progression, and interaction with kink bands on the overall load-strain response.

An interface model for predicting delamination in z-pinned composite laminates is presented in Chapter 4. The design and results of an experimental campaign are also presented which supports calibration of the trilinear constitutive law under mixed-mode conditions. The calibration procedure offers an advantage over existing approaches in the literature by using standardized or simple macroscopic experimental configurations which are commonly employed to characterize mixed-mode interlaminar fracture toughness of unpinned composites. Experimental results provide additional understanding of delamination in the presence of z-pins and z-pin failure mechanisms.

Computational modeling of CAI in z-pinned composites has not been addressed in the open literature. Chapter 5 presents a computational analysis using existing models to predict the effect of z-pins on CAI failure in a standard residual strength test configuration. New experimental results are also presented where the design of the specimens are unique compared to the literature and contribute new information to help evaluate the damage arrestment capability of z-pins under CAI conditions.

Some of the work has been reported in journal or conference articles. The content in Chapter 2 has been reported in Ref. [60]. The content in Chapter 3 has been reported in a conference article [62], and also reported in Ref. [63]. Part of Chapter 5 has been reported in a conference article [61].

CHAPTER 2

Multiscale Compression Kink Band Model

The multiscale nature of failure in long fiber composite materials by compression kink banding is depicted in Fig. 2.1. Material properties and morphological features at several length scales affect the nucleation and propagation characteristics of compression kink bands. Among them, fiber waviness has a pronounced effect on the overall compression strength of the lamina as analyzed by Fleck et al.[66], Vogler et al.[169] and others. The wavelengths associated with fiber waviness observed in CFRPs are in the range of 70-800 times the fiber diameter in the composite [97, 102]. The kink band itself, where fiber and matrix cracking, debonding, and severe matrix deformation coexist, is generally restricted to a width of no greater than a few hundred μm (mesoscale) [33, 170]. The kink band width is sensitive to the fiber diameter, which is approximately 5-10 μm - an order of magnitude smaller than the kink band width (microscale). On the other hand, the size of the structural component or specimen is several orders of magnitude larger than the kink band width (macroscale).

The significant disparity between the scales involved in the kink band induced failure allows the applicability of scale-separable multiscaling principles to this problem (e.g., computational homogenization [49, 65]). The proposed modeling approach is a nonlocal generalization of the Eigenstrain-based reduced order computational homogenization modeling (EHM) [49, 121, 150]. The remainder of this chapter provides an overview of "local" EHM, and generalize it to a nonlocal formulation. The specific features of the nonlocal compression kink-band model are then discussed.

2.1 Eigenstrain-based Homogenization Model (EHM)

EHM is a multiscale progressive damage analysis approach for predicting the failure response of composites and other heterogeneous materials [31, 120, 178, 185]. The basis of the formulation is the computational homogenization theory [17, 73] coupled with transformation field analysis [58]. In EHM, certain information on the material microstructure such as localization operators, polarization tensors, influence functions and coefficient tensors [121] are computed by solving linear elastic microscale problems defined over the material unit cell or representative volume prior to the multiscale progressive damage and failure analysis of a composite structure. The microstructural information is bridged to the macroscopic scale through a reduced order microscale model. The nonlinear analysis and history dependent reduced order microstructure problem is tightly coupled with the structural scale analysis, which are concurrently evaluated (a separate reduced order model is evaluated and tracked at each quadrature point of the macroscale discretization). The precomputed

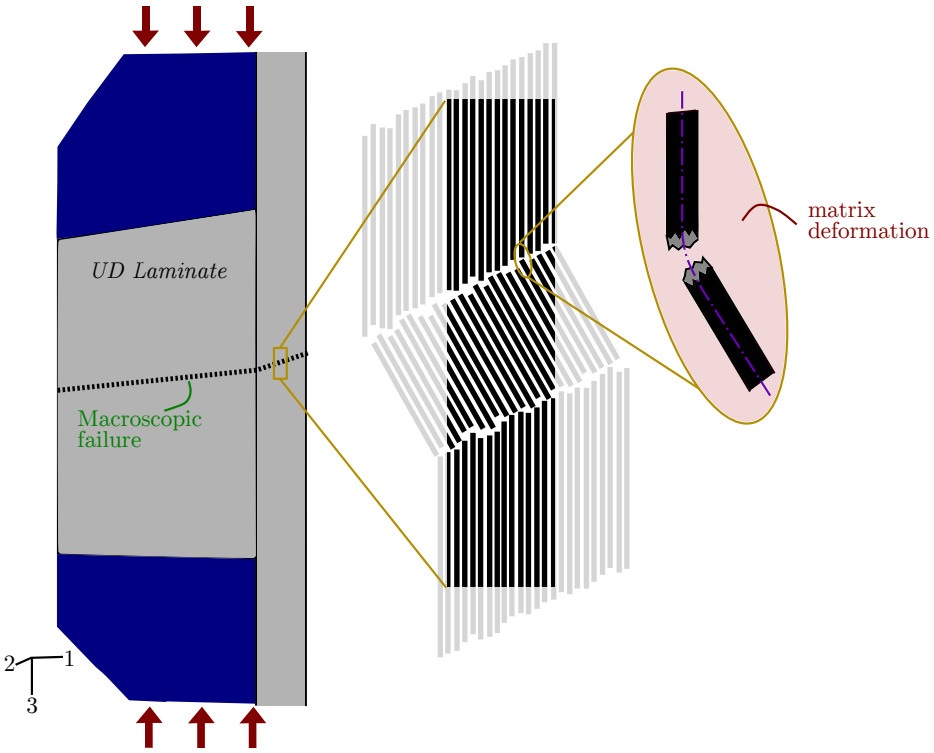

Figure 2.1: Observations of macroscopic compression failure in UD specimens include kink band formation that is linked to significant deformation and fiber curvature. (see e.g., [75, 156, 173])

coefficient tensors along with internal state variables are employed to homogenize or localize the stress and strain fields. The reader is referred to Refs. [31, 121] for details of the EHM formulation. The static force

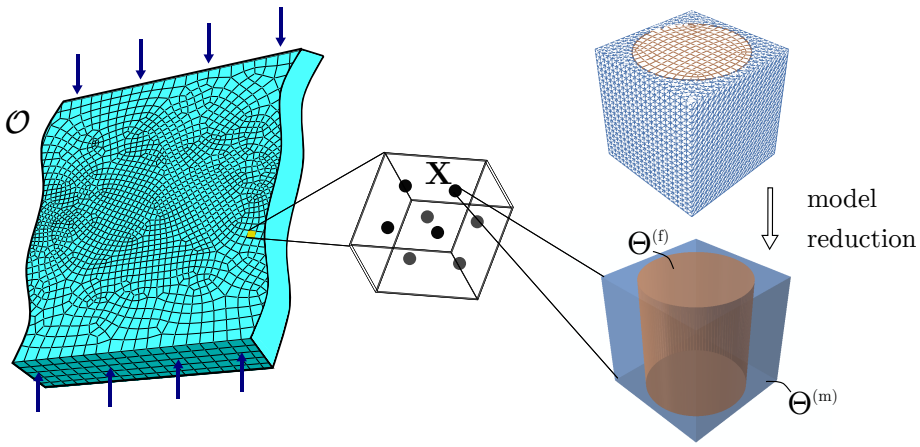

Figure 2.2: The multiscale modeling approach using EHM for fiber kinking employs a reduced-order microstructural response.

equilibrium at the macroscopic scale is expressed as:

$$\nabla \cdot \bar{\boldsymbol{\sigma}}(\mathbf{x},t) = 0; \;\; \mathbf{x} \in \mathscr{O}; \;\; t \in [0,t_0] \tag{2.1}$$

where, $\bar{\boldsymbol{\sigma}}$ denotes the macroscopic (i.e., homogenized) Cauchy stress; $\mathbf{x}(\mathbf{X},t) \in \mathscr{O}(t)$ is the position vector that parameterizes the current configuration of the macroscopic domain, $\mathscr{O}$, with the macroscopic reference (i.e., material) coordinates, $\mathbf{X}$, as illustrated in Fig. 2.2. We consider the evolution of the current configuration since kink band formation is driven by macroscopic instability, and a large-deformation formulation at macroscale is necessary to capture the instability. The macroscopic boundary conditions are expressed as

$$\bar{\mathbf{u}} = \hat{\mathbf{u}}(\mathbf{X},t); \; \mathbf{X} \in \Gamma_u^0 \tag{2.2}$$

$$\bar{\mathbf{P}} \cdot \mathbf{N} = \hat{\mathbf{t}}(\mathbf{X},t); \; \mathbf{X} \in \Gamma_t^0 \tag{2.3}$$

in which, $\bar{\mathbf{u}}(\mathbf{X},t)$ denotes the macroscopic displacement field; $\hat{\mathbf{t}}(\mathbf{X},t)$ and $\hat{\mathbf{u}}(\mathbf{X},t)$ are respectively the prescribed tractions and displacements applied on boundaries Γ_t^0 and Γ_u^0 of the undeformed configuration, $\mathscr{O}^0 := \mathscr{O}(0)$; $\mathbf{N}$ is the unit outward normal to Γ_t; and $\bar{\mathbf{P}}$ is the macroscopic first Piola-Kirchoff stress. Considering the macroscopic deformation gradient, $\bar{\mathbf{F}} = \partial \bar{\mathbf{u}} / \partial \mathbf{X} - \boldsymbol{\delta}$ (with $\boldsymbol{\delta}$ the second order identity tensor), we employ the logarithmic measure to track macroscopic strain, $\bar{\boldsymbol{\varepsilon}}$:

$$\bar{\boldsymbol{\varepsilon}} = \ln \bar{\boldsymbol{V}} \tag{2.4}$$

where, $\bar{\boldsymbol{V}} = \sqrt{\bar{\mathbf{F}}\bar{\mathbf{F}}^T}$ is the left stretch tensor. Considering the brittle characteristics of the constituents of the composite, the large deformations observed in the composite specimen are due to large rotations coupled with small microscopic distortions up to the onset of failure. A local coordinate system is attached to the microstructure that rotates with the macroscopic rotation such that the microstructural stresses are not affected by the rigid body motion of the microstructure (i.e., the co-rotational frame is used). Progressive damage accumulation that leads to macroscopic instability and failure is modeled using continuum damage mechanics approach. The constitutive response of the composite constituents (i.e., fiber and matrix) is described by damage variables. By this representation and microstructural model order reduction through EHM, the Cauchy stress, $\hat{\bar{\boldsymbol{\sigma}}}$, in the co-rotational frame is expressed as:

$$\hat{\bar{\boldsymbol{\sigma}}} = \sum_{\Delta=1}^{n} \left\{ \left[1 - \omega^{(\Delta)} \right] \left[\bar{\mathbf{L}}^{(\Delta)} : \hat{\bar{\boldsymbol{\varepsilon}}} + \sum_{\alpha=1}^{n} \bar{\mathbf{P}}^{(\alpha\Delta)} : \boldsymbol{\mu}^{(\alpha)} \right] \right\} \tag{2.5}$$

in which $\hat{\bar{\boldsymbol{\varepsilon}}}$ is macroscopic strain rotated to the co-rotational frame, $\omega^{(\Delta)}$ denotes a part-average damage variable associated with a subdomain (or part) of microstructure $\Theta^{(\Delta)} \subset \Theta$ (Θ denotes the domain of the microstructure) and taken to be constant within $\Theta^{(\Delta)}$; $\boldsymbol{\mu}^{(\Delta)}$ is the part-average inelastic strain field induced by the damage in the microstructure subdomain, Δ; $\bar{\mathbf{L}}^{(\Delta)}$ and $\bar{\mathbf{P}}^{(\alpha\Delta)}$ are coefficient tensors computed using the influence functions and elastic properties of the constituents. The partitioning of the material morphology into subdomains and the spatially piece-wise constant approximation for damage and damage-induced inelastic strain fields constitute the order reduction strategy. While Fig. 2.2 illustrates partitioning of the microstructure into the matrix and fiber phases, other partitioning strategies are also possible as explored in Refs. [102, 150]. The kinematic equation that relates the inelastic strain coefficients to the macroscopic strain is expressed as:

$$\sum_{\Delta=1}^{n} \left\{ \left[1-\omega^{(\Delta)}\right] \left[\hat{\mathbf{A}}^{(\alpha\Delta)} : \bar{\boldsymbol{\varepsilon}} + \sum_{\gamma=1}^{n} \hat{\mathbf{B}}^{(\alpha\Delta\gamma)} : \boldsymbol{\mu}^{(\gamma)} \right] \right\} = 0, \quad \forall \alpha = 1,...,n \tag{2.6}$$

in which $\hat{\mathbf{A}}^{(\alpha\Delta)}$ and $\hat{\mathbf{B}}^{(\alpha\Delta\gamma)}$ are additional coefficient tensors. This system of equations for the reduced order model is closed by defining evolution equations of the part-average damage variable, $\omega^{(\Delta)}$, which is driven by the local damage history variable, $\kappa^{(\Delta)}$. At a fixed, but arbitrary macroscopic material point:

$$\omega^{(\Delta)} = \Phi(\kappa^{(\Delta)}); \;\; 0 \leq \Phi \leq 1 \tag{2.7}$$

The scalar damage variable $0 \leq \omega^{(\Delta)} < 1$ indicates the current damage state of the composite constituent occupying $\Theta^{(\Delta)}$; the limits $\omega^{(\Delta)} = 0$ and $\omega^{(\Delta)} \to 1$ respectively indicate no damage and complete loss of load carrying capacity within the subdomain of the microstructure. The part damage variable evolves according to the monotonic damage evolution function:

$$\Phi(\kappa^{(\Delta)}) = \frac{\arctan(a^{(\Delta)}\langle \kappa^{(\Delta)} - \kappa_0^{(\Delta)} \rangle - b^{(\Delta)}) + b^{(\Delta)}}{\frac{\pi}{2} + \arctan(b^{(\Delta)})} \tag{2.8}$$

in which $a^{(\Delta)}$, $b^{(\Delta)}$, ${\kappa_0}^{(\Delta)}$ are the material parameters that define the failure behavior of the composite constituent occupying $\Theta^{(\Delta)}$ (i.e., matrix or fiber), and the Macaulay brackets, $\langle \cdot \rangle$, enforce the threshold for the onset of inelastic evolution of damage. The part damage history variable is computed as:

$$\kappa^{(\Delta)} = \max_{0 \leq \tau \leq t} \{ \upsilon^{(\Delta)}(\mathbf{X}, \tau) \} \tag{2.9}$$

taking the value of the maximum damage equivalent strain, $\upsilon^{(\Delta)}$, in the loading history. The damage equivalent strain is defined as:

$$\upsilon^{(\Delta)} = \sqrt{\frac{1}{2}\hat{\boldsymbol{\varepsilon}}^{(\Delta)} : \widehat{\mathbf{L}}^{(\Delta)} : \hat{\boldsymbol{\varepsilon}}^{(\Delta)}} \tag{2.10}$$

which is a function of the local principal strains, $\hat{\varepsilon}^{(\Delta)}$, and the elastic modulus tensor, $\widehat{\mathbf{L}}^{(\blacksquare)}$, rotated to the principal directions. The evolution equations that drive the progressive failure of the composite constituents defined in Eqns. (7)-(10) are macroscopically local in character. This means that the damage evolution within subdomain $\Theta^{(\Delta)}$ at a macroscopic material point is driven by the state of strain and the damage history variable of that macroscopic material point alone. As further explained below, we propose a nonlocal generalization of this approach to better control the thickness of the compression kink band.

2.1.1 EHM for Fiber Kinking

The EHM model as employed to idealize compression kink banding is illustrated in Fig. 2.2. Experimental investigations demonstrate a number of failure processes that either contribute to or result from compression kink bands, including nonlinear shear deformation and damage in the matrix concentrated in the kink band region, fiber fracture (particularly along the edges of the kink band) and fiber-matrix debonding [173]. The microstructure is idealized as a periodic and square unit cell. In view of the fact that the kink band zone exhibiting significant matrix deformation and failure is much larger than the size of the unit cell, we employ an EHM model that consists of 2 parts (i.e., $n = 2$) and considers uniform damage accumulation in the matrix and fiber subdomains of the unit cell. It is also possible to incorporate the progressive debonding mechanism [49, 123], along the fiber-matrix interface, but we exclude this effect to retain simplicity of the model. It is noteworthy that a majority of prior investigations considered elastic-plastic (see e.g. Ref. [66]) or elastic-viscoplastic ([169]) matrix behavior in direct numerical simulation of compression failure. The current study employs a continuum damage model that exhibits a nonlinear hardening behavior followed by material softening. While plasticity was shown to be sufficient to model kink bands, we contend that the relatively brittle matrix response (even considering nonlinear shear effects) could be better captured by a model that incorporates matrix failure.

2.2 Gradient-based Regularization

Initiating from a region of high fiber waviness, localized buckling of the fibers promoted by nonlinear deformation of the matrix yields a kink band region that is many fiber diameters wide [33]. This region is marked by significant fiber rotations, reduced stress carrying capacity, and shear deformation in the matrix. Early analytical studies in Refs. [66, 169] have shown that the width of the kink band is strongly affected by fiber diameter, which controls fiber bending rigidity. This effect has been also studied using direct numerical sim-

ulations [180]. EHM and other first order homogenization methods cannot directly account for fiber bending at the microscale. While higher order homogenization [14, 85] formulations could capture this effect, several computational complications have so far limited their use. Instead, we propose a nonlocal extension of the EHM model to control kink band width in multiscale simulations. Let $\omega^{(\mathrm{m})}(\mathbf{x},t)$ denote the damage state of the matrix subdomain of the unit cell associated with a fixed but arbitrary position on the current configuration, $\mathbf{x}$ at time t. The damage variable is re-written as a function of a *nonlocal* equivalent damage variable, $\bar{\kappa}^{(m)}(\mathbf{x},t)$ as:

$$\omega^{(\mathrm{m})} = \Phi(\bar{\kappa}^{(\mathrm{m})});\ \ 0 \leq \Phi \leq 1 \tag{2.11}$$

In contrast with $\kappa^{(\mathrm{m})}$ in Eqn. 3.3, which is a local history variable, $\bar{\kappa}^{(\mathrm{m})}$ is a field variable, the spatial variation of which is governed by the following expression:

$$\bar{\kappa}^{(\mathrm{m})}(\mathbf{x},t) - {L_0}^2\nabla^2\left[\bar{\kappa}^{(\mathrm{m})}(\mathbf{x},t)\right] = \hat{\kappa}^{(\mathrm{m})}(\mathbf{x},t); \tag{2.12}$$

in which L_0 is a length scale parameter, and ∇^2 denotes the Laplacian operator. $\hat{\kappa}^{(\mathrm{m})}$ is defined as:

$$\hat{\kappa}^{(\mathrm{m})}(\mathbf{x},t) = \min\{\kappa^{(\mathrm{m})}, \kappa_c\} \tag{2.13}$$

where κ_c denotes the value of the local history variable when full damage is reached (i.e., $\Phi(\kappa = \kappa_c) = 1$). Since Φ defined in Eqn. 3.4 only asymptotes to unity, a value slightly less than unity is used to define κ_c (i.e., $\Phi(\kappa_c) = 1 - \varepsilon$) in the numerical implementation. Neumann boundary conditions are enforced to evaluate the nonlocal equation:

$$\nabla\bar{\kappa}^{(\mathrm{m})} \cdot \mathbf{n} = \mathbf{0} \tag{2.14}$$

where $\mathbf{n}$ is the unit outward normal to the domain boundaries.

The numerical evaluation of the proposed nonlocal EHM model solves for two cardinal unknown variables at the macroscopic scale, which are the macroscopic displacements, $\bar{\mathbf{u}}$, and the nonlocal damage history field, $\bar{\kappa}$. The primary idea behind the use of the nonlocal equation is to spatially distribute the effect of $\kappa^{(\mathrm{m})}$ localized at a position coordinate, $\boldsymbol{x}$, to a neighborhood around $\boldsymbol{x}$. The size of this neighborhood is dictated by the length scale parameter, L_0, which is therefore directly correlated with, but not necessarily equal to, the kink band width. The dissipative effect of the nonlocal equation is illustrated in Fig. 2.3. The figure illustrates the analytical solution of the one-dimensional version of Eqn. 3.5 $\left(u(x) - L_0^2 d^2u(x)/dx^2 = \delta(x)\right)$, for which the right hand side (i.e., local variable) is set to the Dirac delta distribution centered at $x = 0$. The figure illustrates how the source (i.e., right hand side) is spatially smoothened out with increasing value of

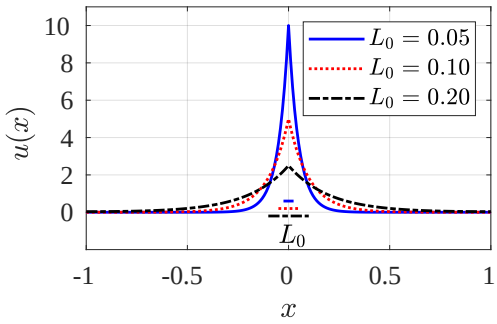

Figure 2.3: The effect of the length scale parameter on the unknown field, $u(x)$, for 3 values of L_0.

the length scale parameter.

In order to give a physical meaning to the length scale parameter, L_0, we turn to the work of Fleck et al.[66]. For a kink band with a kink band angle, $\beta = 0$, Fleck et al.[66] analytically computed the band width as:

$$\frac{w}{d} = \frac{\pi}{4}\left(\frac{E}{2\tau_Y}\right)^{\frac{1}{3}} \tag{2.15}$$

where d denotes the fiber diameter, E is the modulus of the composite along the fiber direction, and τ_y is the composite shear strength. Our numerical simulations described below suggest a linear relationship between the length scale parameter in the nonlocal equation and the kink band width as follows:

$$L_0 = aw + b = \frac{ad\pi}{4}\left(\frac{E}{2\tau_Y}\right)^{\frac{1}{3}} + b \tag{2.16}$$

where, a and b are model parameters, the calibration of which is presented below. Extension of the analytical expression of kink band width with non-zero band angles is provided in Refs. [33, 143]. A relationship could be obtained for the aforementioned and other analytical relationships in a similar way.

After the onset of full damage in the matrix (i.e., $\omega^{(\mathrm{m})} \approx 1$) and consequently the kink band formation, the value of the local history variable, which is a measure of local deformation, could increase substantially in the band. This results in a very large local source term in the nonlocal equation and leads to convergence issues in its numerical evaluation. In order to alleviate these issues, the source term is not allowed to increase beyond the critical value, κ_c as indicated by Eqn. 3.6.

The classical nonlocal damage formulations with gradient type regularization are known to exhibit an expansion of the damage region even after complete failure is observed [131]. Under tensile loading, growth of the damage region is spurious. In the current compression case, this effect results in a steady state broadening of the kink band after the onset of instability. Interestingly, experimental observations do point to a physical

band broadening phenomena as observed in Refs. [110, 111, 170]. However the experimental observations refer to an increase of kink band width of a propagating band, and at a fixed spatial position does not grow. We adopt a technique presented by Poh et al.[131] to control the growth of the kink band after it is formed. It is expected that fully damaged matrix material no longer carries load, and the nonlocal influence of a critically damaged material point on its neighborhood should diminish. Spread of the kink band is controlled by dynamically setting the length scale parameter to reduce as matrix damage evolves (referred herein as the Variable Length Scale formulation or VLS).

$$L(\mathbf{x},t) = g\left(\omega^{(\mathrm{m})}(\mathbf{x},t)\right) L_0 \tag{2.17}$$

$$g = \sqrt{\frac{(1-R)\exp\left(-\eta\,\omega^{(\mathrm{m})}\right) + R - \exp\left(-\eta\right)}{1-\exp\left(-\eta\right)}} \tag{2.18}$$

where, R and η are numerical constants that control the evolution of the length scale parameter as a function of matrix damage. The constant L_0 in Eqn. 3.5 is replaced by L. Figure 4 illustrates the variation of the length scale parameter as a function of the history and damage variables. The length scale parameter decreases sharply only when the damage parameter becomes close to unity, whereas it is approximately constant for low states of damage.

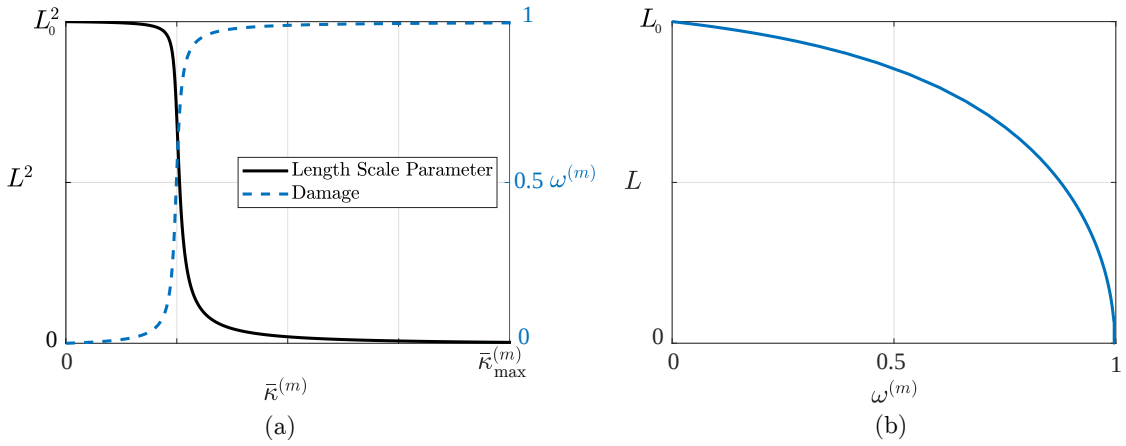

Figure 2.4: (a) Degradation of the length scale parameter and accumulation of damage; (b) relationship between the length scale parameter and damage.

2.3 Fiber Breakage

Fibers in the kink band region undergo bending and ultimately break in tension during unstable localized buckling. In this study, we propose a simple curvature-based criterion to describe fiber break at the macro-

scopic scale. Let $\theta^{'}(\mathbf{x},t)$ denote the orientation of the fiber at the reference macroscopic coordinate, $\mathbf{x}$.

Fiber curvature is then described as $\rho = d\theta^{'}/dz$, where z is the direction along the fiber. The fiber damage model is described as follows:

$$\omega^{(f)} = \begin{cases} 0 \text{ if } \rho < \rho_{crit} \\ 1 \text{ if } \rho \geq \rho_{crit} \end{cases} \tag{2.19}$$

where, ρ_{crit} is a critical curvature value.

It is important to note that the curvature is also a nonlocal value as it requires the spatial gradient of fiber orientation. Details of the computational implementation is discussed below.

2.4 Numerical Implementation

The nonlocal damage formulation presented above was implemented along with the EHM model to predict the compression failure behavior of a unidirectional composite. The model solves the additional partial differential equation (Eqn. 3.5) for the nonlocal equivalent damage scalar variable, $\overline{\kappa}$, fully coupled with the macroscopic stress equilibrium problem (Eqn. 2.1). Conveniently, this coupled system of equations is analogous to that of a coupled thermo-mechanical problem since Eqn. 3.5 can be recast in the form of the steady-state heat equation with a temperature-dependent and nonlinear source term: r.

$$\nabla^2 \left[L^2 \bar{\kappa}(\mathbf{x},t) \right] = r(\mathbf{x},t) \tag{2.20}$$

where, r denotes the source term, which is a function of the damage history variable.

$$r(\mathbf{x},t) = \hat{\kappa}(\mathbf{x},t) - \bar{\kappa}(\mathbf{x},t) \tag{2.21}$$

By leveraging this form for the nonlocal equation, the multiscale reduced order system was implemented in the commercial finite-element software Abaqus. The proposed implementation algorithm is adapted from the work of Seupel et al.[144] and summarized in Fig. 2.5. Given the unit cell geometry and 2-part reduced order model partitioning shown in Fig. 2.2, the coefficient tensors are computed at the preprocessing stage (see Crouch and Oskay[49] for details of coefficient tensor computations). The coefficient tensors along with the model parameters that describe damage evolution within the composite constituents are inputs to the multiscale nonlocal reduced order system. The multiscale system is evaluated by the thermomechanical analysis capability in Abaqus, which solves the macroscale equilibrium and the nonlocal equations in a tightly coupled manner. The evolution of the reduced order microscale problem is treated as stress update and implemented using the user supplied material behavior capability (UMAT). This incremental-iterative update procedure

returns the macroscopic Cauchy stress, the tangent stiffness, and the local history variable. The local history variable $\hat{\kappa}$, which forms part of the source term of the nonlocal equation, is passed to the HETVAL subroutine, where the total source term, r, is calculated and returned along with the gradient terms for Jacobian computation. Incremental evaluation by the nonlinear solver updates the displacement and nonlocal history

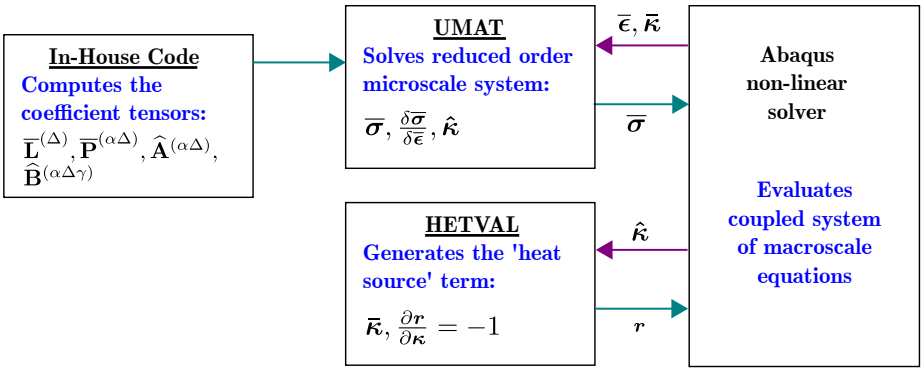

Figure 2.5: Computational procedure for nonlocal damage model.

variable (i.e., temperature) fields. To complete the thermal analogy, the nonlocal variable changes in the case that the heat source solution is nonzero. The "conductivity" of the material (according to the thermal analogy) corresponds to the length scale parameter. The VLS model, where a solution dependent length scale parameter is considered, is implemented by tabulating the temperature-dependent isotropic thermal conductivity property of the material definition (tabulating L dependency on $\bar{\kappa}$ according to Eqn. 3.10). An alternate form to tabular data entry is the use of user supplied material behavior for the thermal problem (using UMATHT).

2.4.1 Fiber Break Routine

Fiber break is incorporated as an online procedure in the user supplied subroutine by updating global variable arrays of the material point orientations during the simulation. For each element of the macroscopic discretization, the neighboring elements along the fiber direction, and distances to neighboring element centroids are calculated at the beginning of the analysis. The orientation of an element centroid during an increment is calculated as the average of the orientations at the material points belonging to that element. The orientation values are extracted by performing polar decomposition on the current deformation gradient in the local frame (a tutorial for obtaining the relevant information from Abaqus is provided by [118]). The curvature is approximated using a first order finite difference scheme based on the element-wise information

at the end of every increment. The primary equations implemented in this routine are as follows:

$$\rho(\tilde{\mathbf{x}},t) = \left| \frac{\theta'(\tilde{\mathbf{x}},t) - \theta'(\tilde{\mathbf{x}}^{\text{neighbor}},t)}{z(\tilde{\mathbf{x}},0) - z(\tilde{\mathbf{x}}^{\text{neighbor}},0)} \right| \tag{2.22}$$

$$\theta'(\tilde{\mathbf{x}},t) = \cos^{-1}\left(\frac{tr(\mathbf{R}(\tilde{\mathbf{x}},t)) - 1}{2} \right) \tag{2.23}$$

$$\bar{\mathbf{F}} = \bar{\mathbf{V}} \cdot \mathbf{R} \tag{2.24}$$

θ' is a calculation for absolute orientation relative to the initial configuration (see e.g., [77]), and the definition for z is the same as in Section 2.3. The neighboring centroid position with respect to an element centroid $\tilde{\mathbf{x}}$ is denoted $\tilde{\mathbf{x}}^{\text{neighbor}}$. $\mathbf{R}$ is the rotation matrix which relates the orientation of the current configuration to the initial local frame. $\bar{\mathbf{F}}$ and $\bar{\mathbf{V}}$ are the deformation gradient and the left stretch tensor in the current configuration as defined in Section 2.1. Once critical curvature is reached for an element, the fiber stiffness is set to zero, i.e. $\omega^{(\text{f})} = 1$.

2.5 Mesoscale Investigations

2.5.1 Problem Setup

Verification of the proposed multiscale model for modeling kink band formation is performed using a mesoscale configuration of a uni-directional composite shown in Fig. 2.6. The mesostructure is subjected to displacement-controlled loading at one end along the z-direction. The lateral faces of the structure are assigned periodic boundary conditions. The geometry and boundary conditions allow the investigations to focus particularly on the onset of kink banding (i.e., initiation). The dimensions of the mesostructure domain are indicated in Fig. 2.6. Analyses are undertaken with the discretized column geometry made of C3D8T linear hexahedral solid elements. The solution proceeds with automatic time stepping and constant stabilization throughout the loading. Both force and heat flux equilibrium states are solved at the macroscopic domain according to the coupled thermo-mechanical analysis scheme described in Section 2.3.

The unit cell idealizing the microstructure of a generic graphite fiber/toughened epoxy material system shown in Fig. 2.2 with a 65 percent fiber volume fraction is employed to construct the EHM model. The elastic properties of the transversely isotropic fiber and the elastic and damage properties of the isotropic matrix are adopted from Ref. [31] and summarized in Table 2.1. The fibers are taken to behave elastically unless broken. The damage evolution parameters were set in such a way that the resulting composite properties under shear and tensile loading are in reasonable agreement with the corresponding strengths reported from v-notch shear and three-point bend tests outlined in Ref. [46]. $\kappa_0^{(\text{m})}$ is selected to be zero so that damage evolution occurs for $\bar{\kappa}^{(\text{m})} > 0$. The remaining parameters, η and R, are numerical constants and the values were set to control

the nonlocal damage effect and result in the relationships shown in Fig. 2.4.

Table 2.1: Elastic and damage parameters of the material constituents

Elastic Parameters			Damage Parameters		
Parameter	Unit	Value	Parameter	Unit	Value
$E_1^{(f)}$	GPa	12.45	$a^{(\mathrm{m})}$	$\mathrm{MPa}^{-1/2}$	1.5
$E_3^{(f)}$	GPa	257.4	$b^{(\mathrm{m})}$	N/A	2.5
$G_{13}^{(f)}$	GPa	146.0	$\kappa_0^{(\mathrm{m})}$	$\sqrt{\mathrm{MPa}}$	0.0
$\nu_{12}^{(f)}$	N/A	0.291	η	N/A	-2
$\nu_{31}^{(f)}$	N/A	0.206	R	N/A	-0.006
$E^{(\mathrm{m})}$	GPa	3.70			
$\nu^{(\mathrm{m})}$	N/A	0.377			

In order to introduce fiber waviness, a general fiber misalignment angle expression based on the material coordinate in the fiber layup direction is used. The element orientation function, ψ, is expressed in a trigonometric form similar to that found in other kink band analyses [27, 169]:

$$\psi(x,y,z) = \tan^{-1}\left(\tan(\psi_0)\sin\left(\frac{\pi z}{l}\right)\right) \tag{2.25}$$

where z is the material coordinate in the fiber direction and l is the half-wavelength of the function ($l =$ 0.5 mm in this example). The *misalignment angle* stated in this work refers specifically to the maximum initial misalignment angle ψ_0, which is prescribed at mid-height of the specimen. The local material orientation at each quadrature point in the initial frame is perturbed by the angle determined in Eq. 5.9 and introduced using the user subroutine, ORIENT, in Abaqus, where we supply the array of direction cosines for the desired material directions with respect to the global coordinate system.

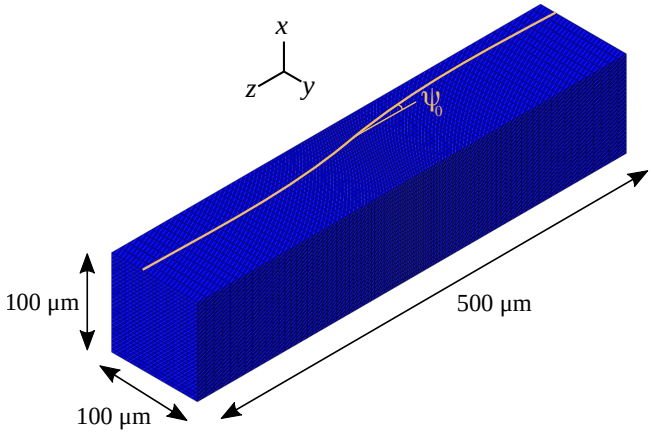

Figure 2.6: Mesoscale problem domain configuration (the gold line is a schematic of the fiber orientation).

2.5.2 Mesh Sensitivity Analysis

In this section, we investigate the mesh size sensitivity of the regularized and unregularized EHM formulations for capturing kink band initiation. The unregularized formulation refers to the evaluation where damage evolution is driven by the local history variable and the nonlocal equation is not included in the implementation. The mesoscale sample is discretized using three different mesh densities. For efficiency, mesh refinements are considered particularly at mid-height, where the highest misalignment and hence the kink band is expected to originate. The coarse mesh has uniform element lengths of 10 µm from end-to-end and the fine mesh has element lengths tapering from 10 µm at the ends to 3 µm across the entire middle 150 µm long section of the domain. The maximum misalignment angle, ψ_0, is set to 2°.

Figure 2.7a shows the damage contours at the onset of kink band formation as predicted by the unregularized formulation using the fine and coarse meshes. The contours indicate that the predicted kink band width is dependent on the mesh size (a single layer of elements fails). Fiber break occurs at the failed element which forms the kink band with both meshes. The stress-strain behavior is shown in Fig. 2.8a and is identical between meshes. Introducing gradient-based regularization to capture nonlocal damage in the material results in a thicker kink band as shown in Fig. 2.7b-c. Fiber breaks occur simultaneously in two equal thickness regions to form the kink band. The coarse mesh and fine mesh simulations predict the kink band width $w \approx$ 80 µm (or 10 times the fiber diameter), with a 1 µm difference due to the resolution limitation of the coarse mesh (width predictions can be made in multiples of element size). The stress-strain behavior predicted using the regularized model is nearly identical for both meshes as shown in Fig. 2.8b.

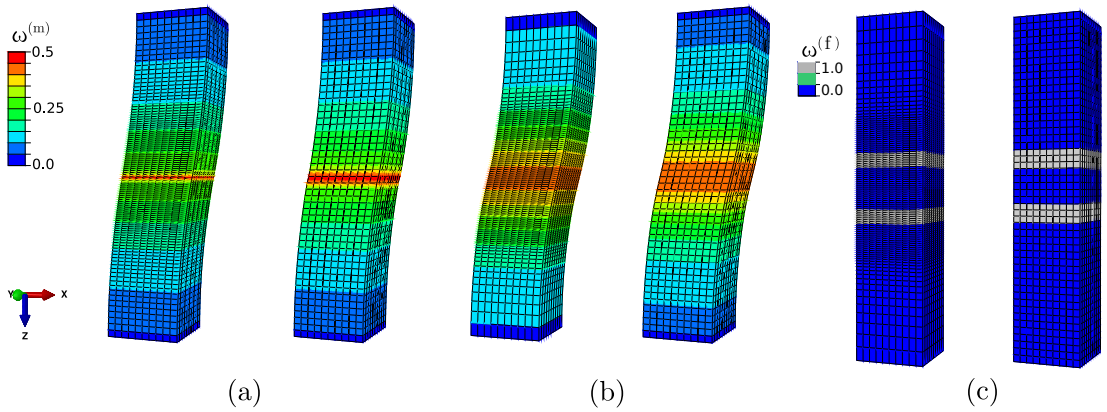

Figure 2.7: Sensitivity of damage development to mesh size with the (a) local and (b) nonlocal damage model formulation ($L_0 = 31.7\ \mu m$); (c) sensitivity of fiber-break prediction to mesh size (nonlocal damage model).

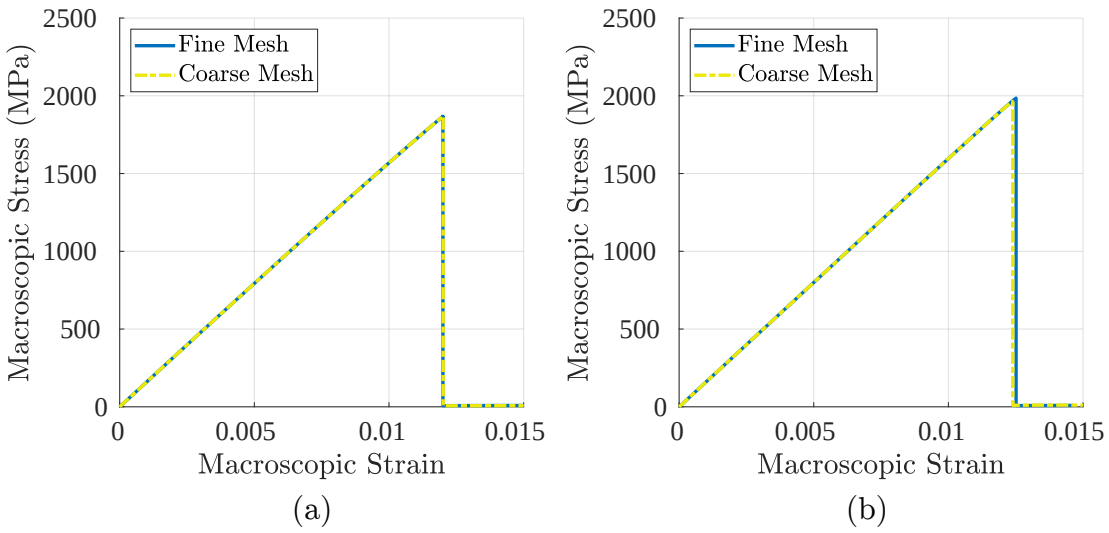

Figure 2.8: Sensitivity of the structural response to mesh size with the (a) local, and (b) nonlocal damage model formulations.

2.5.3 Kink Band Morphology

2.5.3.1 Kink Band Width Control

A parametric study is undertaken to investigate the effect of the length scale parameter on controlling the width of the kink band. As explained in the section, *Fiber Breakage*, the kink band width is dictated by the distance between locations that experience the critical tensile strain for fiber breakage, which are determined based on fiber curvature. The evolution of curvature during the load history along the length of the mesoscale domain is demonstrated in Fig. 2.9. The material segment exhibits a slight gradient in curvature at lower loads, but localized peaks develop at two locations as the load increases. The critical curvature is reached in the vicinity of the maximum load, the fibers break at peak curvature locations, and the kink band width stays constant thereafter. In the current study, the kink band width is defined as the distance between the element centroids that experience fiber breaks. Simultaneously, we observe the stress fields and matrix material behavior. The contour plots in Fig. 2.10a-b display the shear stress of the homogenized material and matrix damage state during the softening stage (macroscopic stress = 1959 MPa). In the region of matrix softening, the in-plane shear stress, $\bar{\boldsymbol{\tau}}_{xz}$, has reached the strength of the homogenized material when loaded in simple shear (approximately 90 MPa). The deformed and initial states of the highlighted elements near and inside the kink band are displayed in Fig. 2.10c, where the deformed elements are translated and clearly have lateral surface normals oriented at an angle compared to horizontal. In fact, periodicity causes the elements to have a form which resembles that of simple or pure shear state in the xz-plane. The greatest shear deformation is experienced in the element near mid-height with a ratio of shear to longitudinal strain: $\bar{\boldsymbol{\gamma}}_{xz}/\bar{\boldsymbol{\varepsilon}}_{zz} \approx 1.92$. The

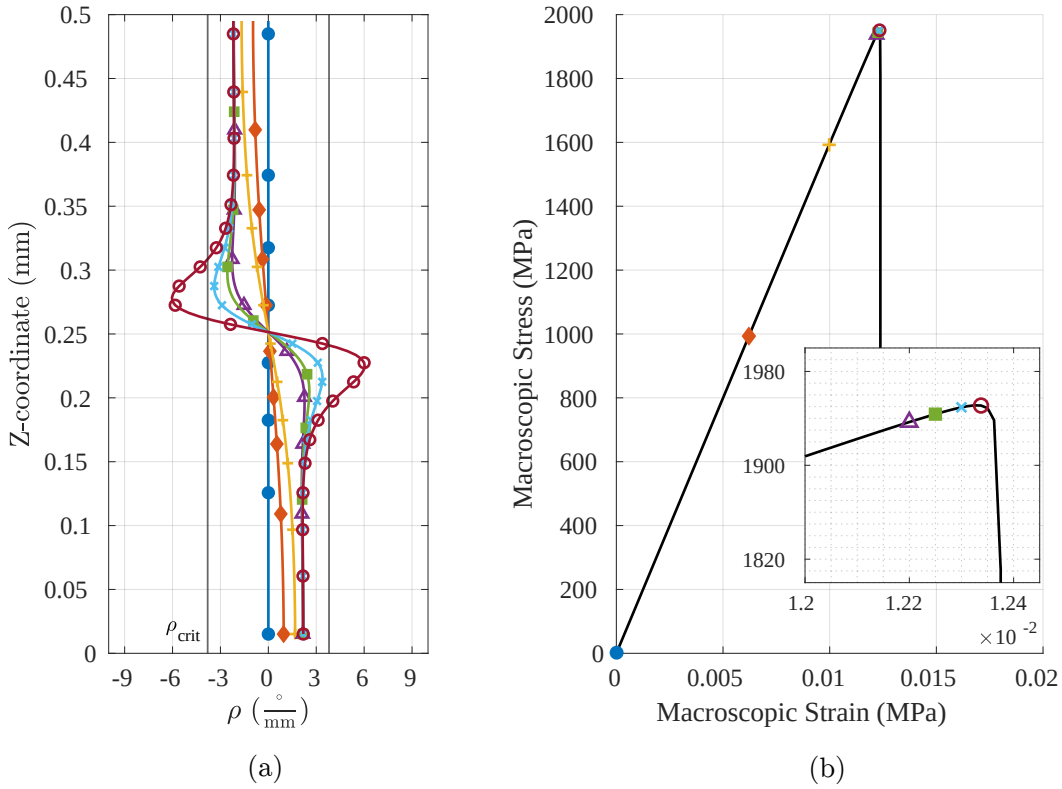

Figure 2.9: (a) Mesoscale curvature at select load levels. (b) Stress-strain response and select load levels. ($L_0 = 20\,\mu m$)

outermost highlighted elements are also experiencing a shear-dominated deformation but the ratio of straining is smaller, $\bar{\boldsymbol{\gamma}}_{xz}/\bar{\boldsymbol{\varepsilon}}_{zz} \approx 1.48$. The other normal and shear strain components are much smaller in all elements. Shear-dominated deformation in the kink band is consistent in all subsequent simulations and agrees with experimental observations like those of Vogler et al [169] where a softened external shear response signals the existence of a kink band. The value of the critical curvature is important since compressive strength is determined by the interplay between fiber breakage, matrix deformation and the buckling instability. As shown in Fig. 2.9, curvature peaks form prior to reaching the macroscopic strength, and quickly grow with localized deformation following the onset of buckling. If critical curvature occurs after the onset of buckling, matrix strength dictates the compressive strength of the composite. If critical curvature is reached prior to reaching the matrix deformation controlled buckling strength, sudden fiber breakage determines the composite strength. As a first order approximation, we use a simple bending formula to compute $\rho_{crit} = 2\sigma^f_{max}/E^f d$ ($\sigma^f_{max} = 4.25$ GPa is the fiber tensile strength, $E^f = 280$ GPa is the fiber longitudinal modulus, $d = 8\,\mu m$ is the fiber diameter) that results in a fiber reaching its tensile strength at 3.8 $^\circ$/mm. Using this criterion value, the relationship between the length scale parameter, L_0 and the resulting kink band width is shown in Fig. 2.11.

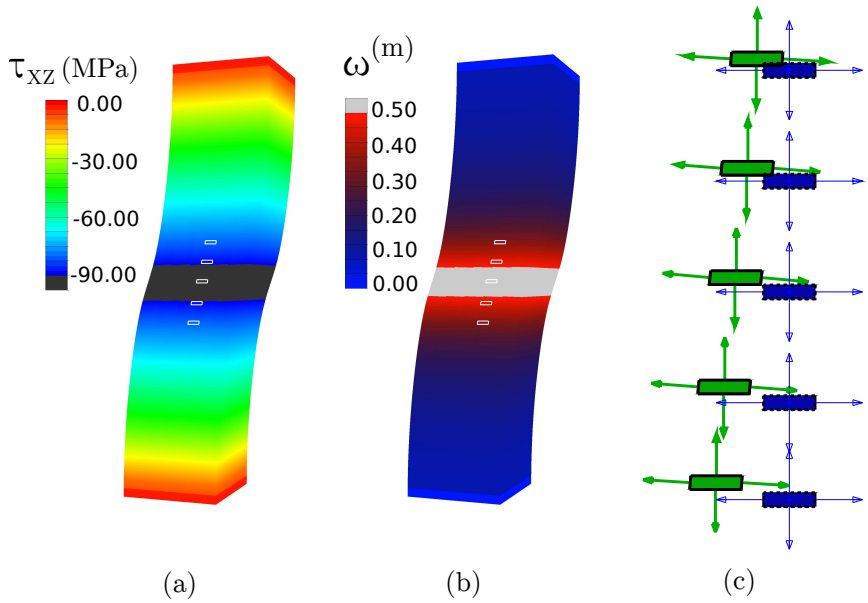

Figure 2.10: (a) Shear stress and (b) matrix damage during softening. (c) Parallel view of highlighted elements in deformed and initial state, including surface normal directions. ($L_0 = 20\,\mu$m, deformation 4x).

The linear correlation already indicated in Eqn. 2.16 is confirmed by the figure.

This linear relationship between the nonlocal length scale parameter and material properties allows us to control of the kink band width by adjusting the length scale parameter and using the linear relationship ($a = 1.21$, $b = 41.74$). The y-intercept in the figure indicates the predicted kink band width at the local limit, where the nonlocal model degenerates to the local model. The relative insensitivity of the linear relationship to the constituent and composite parameters is shown in Fig. 2.12. The kink band width predictions for four composite materials using the length scale parameter selection via Eqn. 2.16 are shown to agree with the results of the theoretical relationship Eqn. 2.15 in Fig. 2.12.

2.5.3.2 Misalignment Effects

The mesoscale investigations discussed thus far have included a misalignment form as expressed in Eqn. 5.9. With this waviness definition we are able to observe formation of a kink band. To account for uncertainty of the misalignment fields found in composites, the behavior of the model is investigated for variations of this damage localization feature. The effect of misalignment angle on strength is plotted in Fig. 2.13 for a range of misalignment angles corresponding to the magnitude of imperfections introduced during the composite specimen manufacturing process [159]. In the case of very small misalignment angle in the fibers, the response of the model is expected to be nearly elastic and consequently results in the highest strength prediction. The reduction in strength is attributed to the effect of the misalignment angle magnitude on instability initiation –

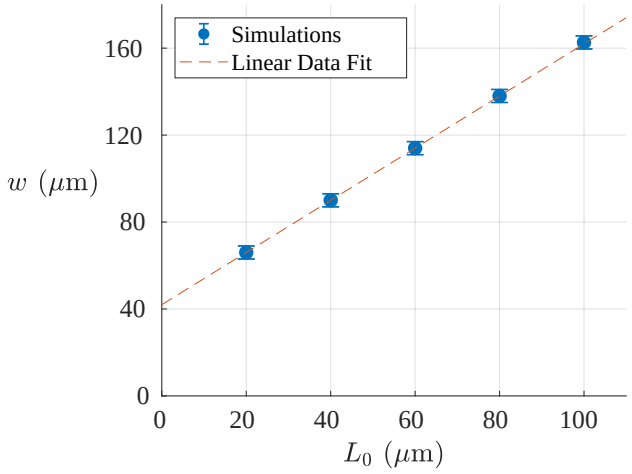

Figure 2.11: Relationship between nonlocal length scale parameter and kink band width.

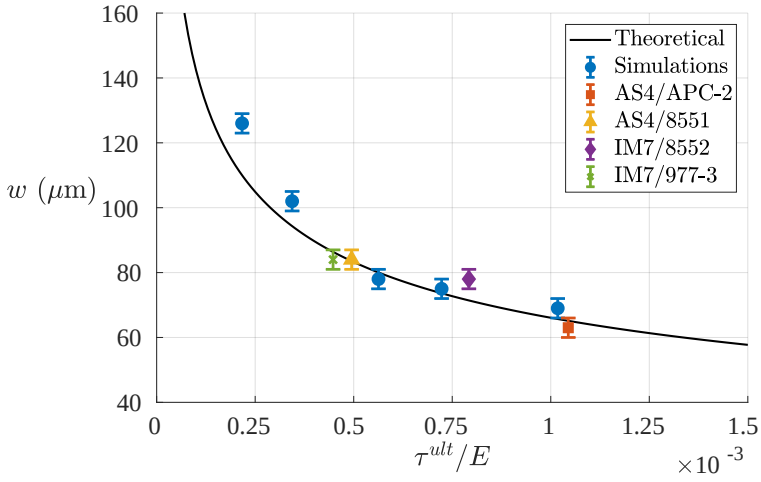

Figure 2.12: Kink band width predictions from simulations compared to analytical results, using calculated length scale value (material system properties referenced from Refs. [27, 31, 99, 170]).

a result that is consistent with the micromechanical analysis in Naya et al [115]. We additionally compare our predictions to the relationship provided by Budiansky and Fleck [33], where the kinking stress is a function of the composite shear properties and misalignment angle alone. The multiscale model predicts a similar but shallower slope for low misalignment angles. The relationship between kink band failure strength and misalignment angle reinforces the notion of instability due to matrix material failure. Larger initial misalignment implies that the composite material is rotated compared to the external compression and more susceptible to undergoing shear-dominated deformation.

In addition to studying the effects of magnitude of misalignment angle with the sinusoidal fiber mis-

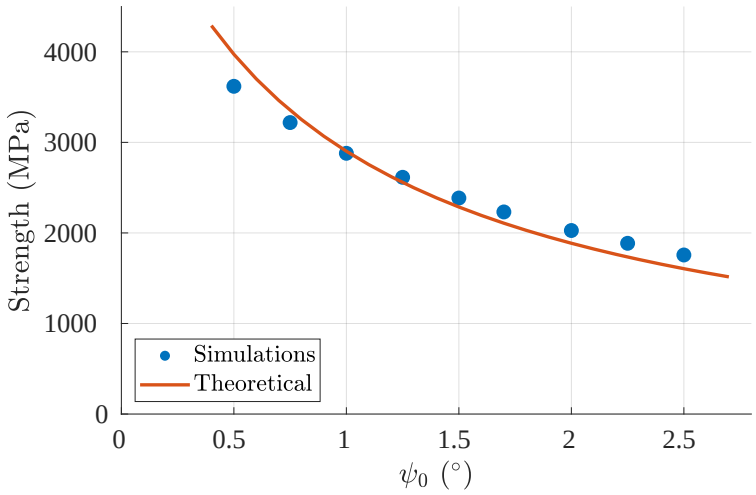

Figure 2.13: The effect of fiber misalignment angle on strength predictions, compared to Ref. [33].

alignment angle form we also explore how changing the shape of misalignment affects the compression strength. Initial fiber misalignment in the form of a Gaussian distribution is also considered: $\mathcal{N}(\mu,\sigma) = \frac{1}{\sigma\sqrt{2\pi}}\exp\left(-\frac{1}{2}\left(\frac{z-\mu}{\sigma}\right)\right)$. The general forms of fiber misalignment investigated are illustrated in Fig. 2.14a. Decreasing the standard deviation value shrinks the region of initial maximum misalignment, and the effect of this misalignment localization on compression strength is shown in Figure 2.14b. There is a significant decrease in compression strength as the region of misalignment is localized (Fig. 2.14b reports strengths relative to the sinusoidal misalignment case). This conclusion is consistent with trends observed in direct numerical simulations [27]. Interestingly, the analysis of Ref. [169] considers a similar sinusoidal misalignment field and concludes that additional spatially localized imperfections have negligible effect on kink band width and failure strength. The somewhat gradually distributed fiber misalignment form described by a maximum misalignment angle used in this study has proved sufficient to initiate kink band formation within the bulk material and therefore model predictions can be taken as conservative.

2.5.3.3 Shear Nonlinearity Effects

As presented in the model formulation section, the matrix material constituent of this EHM implementation has been modelled with degradeable properties according to an arctangent function for the damage potential. This material behavior neglects nonlinear shear effects that are found in plastic behavior of polymers, including cured epoxy resins. Examples of modified matrix behavior under shear are used in order to vary the nonlinearity of the microstructural model and are plotted in Fig. 2.15. As Fig. 2.15 shows, the initial shear modulus and ultimate strength values are constant in these cases, but the response shape through the

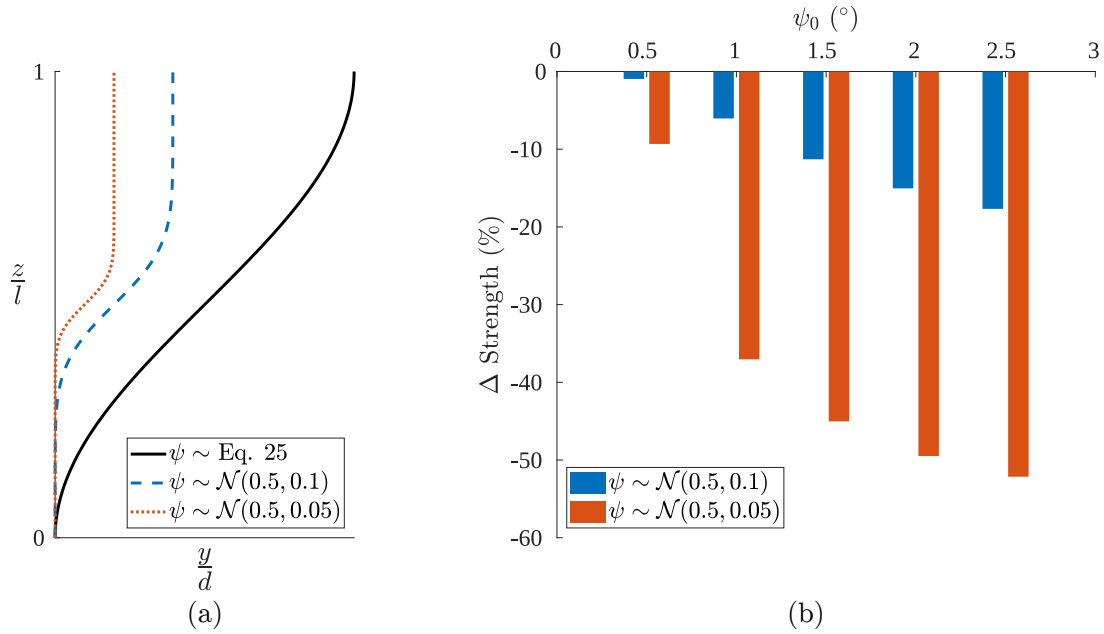

Figure 2.14: (a) Varied forms of initial fiber misalignment distribution. (b) Change in compression predictions with respect to sinusoidal fiber misalignment field.

ultimate strength varies from sharp (weak nonlinearity: $a^{(\mathrm{m})} = 190,\ b^{(\mathrm{m})} = 210$) to gradual (strong nonlinearity: $a^{(\mathrm{m})} = 0.58,\ b^{(\mathrm{m})} = 0.55$) softening and hardening behavior. The moderate case matches what has been used in the simulations presented thus far.

Simulations using the mesoscale problem setup are performed with all properties and parameters held constant while varying the shear nonlinearity behavior. The kink band results for the three cases are shown in Fig. 2.16. Since matrix damage of nearly 50% causes the instability leading to kink band formation, the material state corresponding to that value was examined. The weak nonlinear matrix behavior leads to a fairly

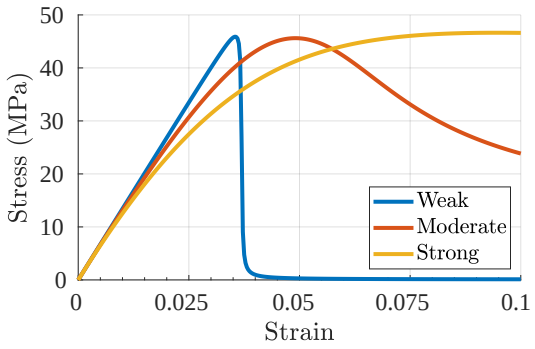

Figure 2.15: Example matrix shear behaviors ($L_0 = 31.7\,\mu\mathrm{m}$)

concentrated damage field prior to failure, wide bands of broken fibers, and $w \approx 51\,\mu m$. Conversely, applying strong shear nonlinearity results a broader damage field prior to kink band failure, concentrated locations of fiber break, and $w \approx 126\,\mu m$; recall that the moderate nonlinearity results in $w \approx 80\,\mu m$. In the strong nonlinearity case there are larger strains at locations further from the maximum initial misalignment, and the material in this relatively wide region rotates to be subject to shear-dominant strain under the compressive load. The trend of these results align with observations of composites with more ductile thermoplastic materials, which exhibit larger kink band widths (approximately 20 times the fiber diamater) [110, 170] compared to more brittle toughened epoxy matrix materials (approximately 10 times the fiber diameter) [27, 99]. Several experiments have been conducted on UD carbon fiber/epoxy composite configurations which produce high quality in situ and post mortem images of kink band morphology at the microscopic scale. The kink band forms displayed in Fig. 2.16 agree with experimental results in in Wang et al. [173] and Sun et al. [156] from composites containing standard modulus carbon fibers, and Gutkin et al. [75] from a composite containing intermediate modulus carbon fibers. The composite properties considered in this investigation most closely match those of Gutkin et al. [75], and the kink band width is shown to be less than $100\,\mu m$. The test procedures, equipment, and materials in these experiments are all different but fall under the category of UD carbon fiber/epoxy specimens under longitudinal compression. Briefly described, these are conducted with (a) a (standard) Combined Loading Compression (CLC) test fixture and single edge notched (SEN) plates [156]; (b) a Scanning Electron Microscopy (SEM) screw-driven test jig and SEN plates [75]; (c) uniaxial compression on waisted rods [173].

2.6 Conclusions

This chapter presented a multiscale model to predict the progression of damage in a fibrous composite under compression. Kink band formation is predicted with a nonlocal damage gradient regularization scheme coupled to a computational homogenization method in solving the macrostructural response. We are able to employ quasi-static analyses to investigate the instability-driven kink band failure mechanism. The kink band initiates due to matrix softening that results in the onset of buckling and is completely formed when fibers break as a result of localized curvature. Overall, the predicted effects of material properties and fiber misalignment angle on kink band width and failure strength corroborate analytical and experimental results in the literature. The effects of nonlinear shear behavior of the matrix material were also shown to contribute significantly to the kink band width and should be taken into account when calibrating the model to a specific matrix constituent material. Additional features of the presented multiscale approach are: (1) the homogenized model is able to capture various kink band widths without geometric representation of the fibers; and (2) only a small amount of mesh sensitivity is observed and the model also exhibits convergent predictions

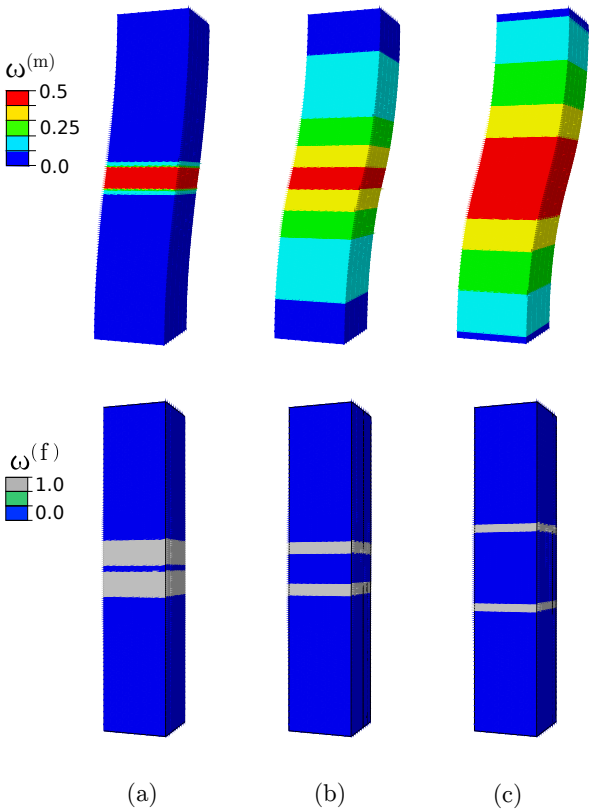

Figure 2.16: Matrix damage at kink band initiation, and fiber break fields corresponding to (a) weak, (b) moderate, and (c) strong nonlinear shear matrix response.

with an implicit FE analysis procedure, thereby allowing application of the model for simulation of experimental configurations. The proposed model holds the potential to be used in analysis of larger scale laminated structures as well. The multiscale approach allows discernment and efficiency in exploring the aspects that make up the kink band problem.

CHAPTER 3

Computational Analysis of the Failure Mechanisms of a Laminated Composite in Double-Edge Notch Compression Configuration

A recent experimental investigation performed on double-edge notched CFRP specimens provide additional insight into the progressive damage growth under quasi-static compressive loading [45]. The geometry and layup of the specimen resulted in stable damage progression which enabled detailed experimental characterization of failure onset and growth as a function of load amplitude. This chapter presents application of a multiscale computational model to study the onset, growth, and interplay of the failure mechanisms observed in the double-edge notched compression (DENC) experiments. A nonlocal multiscale model originally proposed in Ref. [60] is generalized to study laminated kink band formation and propagation. A CZM-based model is incorporated to study the effect of splitting on the compression performance of the DENC samples. The kink band and splitting models were calibrated based on a suite of experimental data and image analysis. DENC specimens were simulated with the calibrated model and a detailed analysis of how progressive splitting and kink band failure interacts to culminate in specimen failure is performed based on computational and experimental evidence. A unique contribution of this work is that it compares the predicted onset and progression of compression failure mechanisms to experimental data and images generated from specimens subjected to sub-critical loads.

3.1 Methods

3.1.1 Experimental

Experiments were performed at the Air Force Research Laboratory (AFRL) on CFRP laminates in a double-edge notch compression (DENC) configuration [45]. The DENC specimens were hand-laid with IM7/977-3 carbon/epoxy unidirectional pre-impregnated tape in a stacking sequence of $[0_3/+45/-45/90/0]_S$ and autoclave cured. Two notches were introduced by milling and were examined to ensure that no damage was introduced in the gage section. Tabs were bonded to both ends of the specimens using a two-part structural paste adhesive. The final specimen geometry and dimensions are shown in Fig. 3.1a-b. The reasons for choosing the layer arrangement and the notch geometry used in the experiments are discussed in Ref. [45]. The test procedure followed ASTM D6641 [10], where a constant displacement rate of 1.3 mm/min was applied to the gripped specimen using a combined loading compression test fixture. Load-displacement from the test machine was acquired in addition to local strains and displacements across the gage section between the notches measured using a virtual extensometer (VE) system as indicated in Fig. 3.1b. Both the test

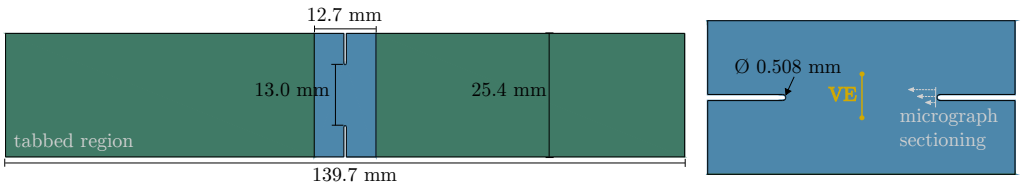

Figure 3.1: (a) Geometry and dimensions of the DENC test article, (b) detailed view of the gage section.

frame and VE data were captured at 10 Hz. Multiple other imaging techniques were employed to examine failure during testing. Optical images of the exterior surface in the gage section were captured throughout the test at 100 Hz using a digital camera. Microcomputed Tomography (μCT) scans were performed on damaged composite specimens with and without zinc-iodide dye penetrant using a Zeiss Xradia Versa 620 X-ray Microscope system equipped with a 160 kV transmission target X-ray source and a flat-panel detector. A series of optical objectives allowed multiple magnification levels. Micrographs were produced using a Nikon MM-60 table-top microscope, NIS-Elements D software, and a DS-Fi2 camera. Energy-event readings from acoustic emission sensors were used to define two load intervals for interrupting tests prior to ultimate load as well as an observable damage threshold. A grind/polish process was performed with these specimens and micrographs were obtained across the width of the specimens from one notch as indicated in Fig. 3.1b and described in [45]. No damage was detected in the test specimens when an acoustic energy jump (or event) was recorded with a value less than 10^{-13}J. The X-ray CT images provide additional detail on the internal extent of damage.

Additional property characterization experiments were performed on unidirectional 0 degree (UD) specimens. The experiments include compression loading of UD DENC specimens. Configuration, dimensions and test procedure for the UD DENC specimens are identical to the DENC specimens as shown in Fig.3.1, including specimen thickness. Other characterization experiments include shear loading parallel to the fiber direction of V-notch specimens, double cantilever beam (DCB), and end-notch flexure (ENF) configurations. The UD compression, DCB, and ENF tests were carried out at the AFRL. The V-notch tests were carried out at the Mechanics of Composite Materials Laboratory at Tel-Aviv University. The breakdown of experiments by calibration and analysis phase, the testing procedure followed, and the quantity of tests performed are shown in Table 3.1. The DENC experiments and results have been previously reported in [45]. Additional images generated during the experimental program but not included in [45] are used in the model calibration (Section 3.2.1) and analysis (Section 3.2.2).

Table 3.1: Breakdown of experiments.

Calibration			Analysis		
Experiment	Procedure	Qty.	Experiment (stop criteria)	Procedure	Qty.
UD DENC	[10]	4	DENC (Failure)	[10]	9
V-notch shear	[9]	5	DENC (Load Interval 1)	[10]	9
DCB	[11]	5	DENC (Load Interval 2)	[10]	16
ENF	[8]	5			

3.1.2 Numerical Modeling

3.1.2.1 Multiscale Compression Kink Band Model

A reduced order multiscale model proposed in [60] has been used to represent the compression kink-band failure behavior in the composite specimens. The model is based on the eigenstrain-based reduced order computational homogenization (EHM) approach which has been previously used to study progressive failure behavior of composites under a range of loading and environmental conditions [30, 31, 83, 122, 178]. The model keeps track of the failure processes associated with kink band formation at the scale of the microstructure coupled to a computational homogenization method in solving the macrostructural compression response. The evolution of nonlinear shear deformation and damage in the matrix concentrated in the kink band region are explicitly tracked. The length scale of the kink band (i.e., the kink band width) is captured by using a gradient-based nonlocal formulation. Full description and verification of the multiscale kink band model are provided in [60]. The constitutive relations for the multiscale kink band model are summarized below.

Under compression loading, the composite laminate undergoes localized instability induced by material imperfections (i.e., fiber misalignment or waviness). Kink bands form as a result of excessive deformation of the matrix and localized bending-induced fiber fracture near these regions of instabilities. The failure in the matrix is modeled using continuum damage mechanics. Upon onset of instability at the mesoscale, the fibers buckle and no longer contribute to load carrying capacity. For simplicity, explicit fiber fracture induced by local buckling is not considered in the model. The formulation described in Ref. [60] includes fiber breakage as well. Mesoscale analyses conducted with and without fiber breakage predict the same compression strength in UD specimens.

The localized large deformation behavior is captured using a co-rotational formulation, where a local coordinate system is attached to the microstructure that follows macroscopic rotation. In what follows, a superposed hat, $\hat{(\cdot)}$ indicates the corresponding field expressed in local coordinates, and a superposed bar, $\bar{(\cdot)}$ indicates a macroscopic quantity. At a given material point in the specimen, the macroscale Cauchy stress, $\hat{\bar{\boldsymbol{\sigma}}}$, in the co-rotational frame is expressed as:

$$\hat{\bar{\sigma}} = \left[1-\omega^{(\mathrm{m})}\right]\left[\overline{\mathbf{L}}^{(\mathrm{m})} : \hat{\bar{\varepsilon}} + \overline{\mathbf{P}}^{(\mathrm{mm})} : \mu^{(\mathrm{m})}\right] + \left[\overline{\mathbf{L}}^{(\mathrm{f})} : \hat{\bar{\varepsilon}} + \overline{\mathbf{P}}^{(\mathrm{mf})} : \mu^{(\mathrm{m})}\right] \tag{3.1}$$

in which $\hat{\bar{\varepsilon}}$ is the macroscopic strain; $\omega^{(\mathrm{m})}$ denotes the damage state within the matrix. The scalar damage variable evolves within $0 \leq \omega^{(\mathrm{m})} < 1$ with limits $\omega^{(\mathrm{m})} = 0$ and $\omega^{(\mathrm{m})} \to 1$ respectively indicating no damage and complete loss of load carrying capacity within the matrix. $\mu^{(\mathrm{m})}$ is inelastic strain induced by the damage process within the matrix. $\overline{\mathbf{L}}^{(\cdot)}$ and $\overline{\mathbf{P}}^{(\cdot)}$ are coefficient tensors that reflect the effect of microstructural morphology on determining the macroscopic stress state ([31, 121, 150]). The kinematic equation that relates the inelastic strain coefficients to the macroscopic strain is expressed as:

$$\left[1-\omega^{(\mathrm{m})}\right]\left[\hat{\mathbf{A}}^{(\alpha\mathrm{m})} : \bar{\varepsilon} + \hat{\mathbf{B}}^{(\alpha\mathrm{mm})} : \mu^{(\mathrm{m})}\right] + \left[\hat{\mathbf{A}}^{(\alpha\mathrm{f})} : \bar{\varepsilon} + \hat{\mathbf{B}}^{(\alpha\mathrm{fm})} : \mu^{(\mathrm{m})}\right] = 0; \quad \alpha = \mathrm{m}, \mathrm{f} \tag{3.2}$$

in which $\hat{\mathbf{A}}^{(\cdot)}$ and $\hat{\mathbf{B}}^{(\cdot)}$ are additional coefficient tensors.

This system of equations for the model is closed by defining evolution equations for the matrix damage variable. The matrix is taken to exhibit a nonlinear hardening behavior followed by material softening. The damage behavior is described as a function of the nonlocal damage history variable, $\tilde{\kappa}^{(\mathrm{m})}$:

$$\omega^{(\mathrm{m})} = \Phi(\tilde{\kappa}^{(\mathrm{m})}); \;\; 0 \leq \Phi \leq 1 \tag{3.3}$$

which evolves according to the monotonic damage evolution function:

$$\Phi(\tilde{\kappa}^{(\mathrm{m})}) = \frac{\arctan(a^{(\mathrm{m})}\langle \tilde{\kappa}^{(\mathrm{m})} - \kappa_0^{(\mathrm{m})} \rangle - b^{(\mathrm{m})}) + b^{(\mathrm{m})}}{\frac{\pi}{2} + \arctan(b^{(\mathrm{m})})} \tag{3.4}$$

where $a^{(\mathrm{m})}$, $b^{(\mathrm{m})}$, $\kappa_0{}^{(\mathrm{m})}$ are material parameters, and the Macaulay brackets, $\langle \cdot \rangle$, are used to enforce the threshold for the onset of inelastic evolution of damage.

When not regularized, continuum damage mechanics models localize damage to a region dictated by the size of the finite elements [4, 146]. The width of the compression kink bands on the other hand are dictated by fiber properties (e.g. fiber size [180] and longitudinal modulus [66]) and matrix properties (e.g. shear nonlinearity or "ductility" [16, 111]). The model employed in this study uses a gradient based regularization scheme to consistently capture the kink band width [60]. The nonlocal equivalent damage variable is expressed using

the following partial differential equation defined over the domain of the specimen parameterized by $\mathbf{x}$:

$$\tilde{\kappa}^{(\mathrm{m})}(\mathbf{x},t) - L^2\nabla^2\left[\tilde{\kappa}^{(\mathrm{m})}(\mathbf{x},t)\right] = \kappa^{(\mathrm{m})}(\mathbf{x},t); \tag{3.5}$$

in which L is a length scale parameter related to the size of the kink band width, and ∇^2 denotes the Laplacian operator. $\kappa^{(\mathrm{m})}$ is defined as:

$$\kappa^{(\mathrm{m})}(\mathbf{x},t) = \min\{\hat{\kappa}^{(\mathrm{m})}, \kappa_c\} \tag{3.6}$$

where κ_c denotes the value of the local damage history variable when full damage is reached (i.e., $\Phi(\hat{\kappa} = \kappa_c) \approx 1$). The local damage history variable is $\hat{\kappa}^{(\mathrm{m})}$ is defined as:

$$\hat{\kappa}^{(\mathrm{m})} = \max_{0\leq\tau\leq t}\{\upsilon^{(\mathrm{m})}(\tau)\} \tag{3.7}$$

taking the value of the maximum damage equivalent strain, $\upsilon^{(\mathrm{m})}$, in the loading history. The damage equivalent strain is defined as:

$$\upsilon^{(\mathrm{m})} = \sqrt{\frac{1}{2}\hat{\boldsymbol{\varepsilon}}^{(\mathrm{m})} : \widehat{\mathbf{L}}^{(\mathrm{m})} : \hat{\boldsymbol{\varepsilon}}^{(\mathrm{m})}} \tag{3.8}$$

which is a function of the local principal strains, $\hat{\boldsymbol{\varepsilon}}^{(\mathrm{m})}$, and the elastic modulus tensor, $\widehat{\mathbf{L}}^{(\mathrm{m})}$, rotated to the principal directions. Neumann boundary conditions are enforced to evaluate the nonlocal equation:

$$\nabla\tilde{\kappa}^{(\mathrm{m})} \cdot \mathbf{n} = \mathbf{0} \tag{3.9}$$

where $\mathbf{n}$ is the unit outward normal to the domain boundaries.

A drawback of the regularization scheme employed in this study is the observed expansion of the damage region under sustained loading even after the failure is reached within the specimen (see also, e.g., [69] for a discussion on this type of spurious growth). We note that this is unrelated to the observation reported on the growth of the kink band width as it propagates [111, 170], as the numerical simulations exhibit widening in parts of the kink bands that have already formed as well. The spurious spread of the kink band is controlled by degrading the length scale parameter as matrix damage evolves [131]:

$$L(\mathbf{x},t) = (c_1 w + c_2)\cdot g\left(\omega^{(\mathrm{m})}(\mathbf{x},t)\right) \tag{3.10}$$

$$g = \sqrt{\frac{(1-R)\exp\left(-\eta\,\omega^{(\mathrm{m})}\right) + R - \exp\left(-\eta\right)}{1-\exp\left(-\eta\right)}} \tag{3.11}$$

where, c_1 and c_2 are model parameters, and w is the observed kink band width; R and η are numerical

constants controlling the length scale degradation.

3.1.2.2 Cohesive Zone Model for Splitting

We consider a standard CZM described in Ref. [38]. Similar CZM models have also been used in modeling splitting in CFRP composites [76, 116, 167]. The traction-separation law follows a bi-linear form using a quadratic stress damage initiation criterion and linear softening slope enforced for critical fracture energy. Mixed mode state is expressed according to the Benzeggah-Kenane relationship [18]. Evolution of the damage variable for the ply interface is as described in [38].

3.1.2.3 Implementation Details

In EHM, a nonlinear analysis and history dependent reduced order microstructure problem is concurrently evaluated with the structural scale analysis. A separate reduced order microstructure model is evaluated and tracked at each quadrature point of the macroscale discretization. Simulations are performed using commercially available implicit finite elements analysis code, Abaqus/Standard. The microstructure in the analysis is idealized as a periodic and square unit cell with two parts representing the damageable matrix and the elastic fiber. The coupled macroscopic system of equations for equilibrium and nonlocal equations is implemented through the use of coupled thermo-mechanical solver. The nonlocal equation is enforced on the 0 degree plies only, as the critical kink bands are expected to occur on 0 degree plies. Matrix damage evolution is also considered in the non-zero degree plies to predict failure by transverse cracking [30, 31]. In this case, the length scale parameter is set to a small (near zero) value since the length scale parameter is associated with the kink band width. The full implementation workflow of the kink band model is detailed in Ref. [60] and is implemented in the same manner here for the nonlocal matrix damage using a user-defined material and auxiliary data passing subroutines. In-built Abaqus capabilities are used for CZM models of splitting.

3.1.2.4 Simulation Setup

The geometry, discretization and the boundary conditions used in the specimen simulations are shown in Fig. 3.2. The domain for the analysis is constructed to match the gage section of the DENC specimen. Boundary conditions corresponding to displacement control are applied on the numerical gage section top and bottom faces which are aligned to the ends of the gripped tabs on the experiment test articles. The plies composing the laminate are modeled by dividing the geometry into equal thickness layers matching the number of plies in the layup and assigning an initial material orientation that match the ply fiber directions. Computational expense is balanced with higher resolution of the failure mechanism predictions by partitioning the ply layers into elastic and damageable regions as shown in Fig. 3.2 and meshed with full-integration continuum elements.

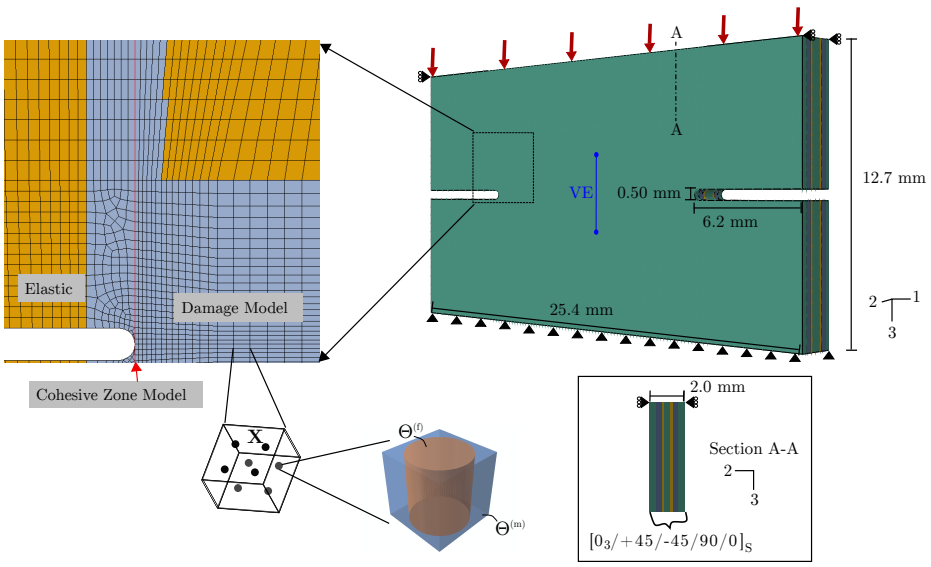

Figure 3.2: Analysis geometry, boundary conditions, mesh, and model assignment.

The mesh size is uniform in the thickness direction, where there are two elements for every ply (i.e. 28 elements through the thickness). The mesh is structured and elements lengths vary from approximately 70 µm in between the notches to 300 µm outside of the damageable region. While damage models without regularization are typically mesh-sensitive, the compression kink band model used in this study is regularized through the gradient-based regularization scheme with the kink band width serving as the nonlocal length scale. The mesh independence of the kink band model has been demonstrated in Ref. [60].

It is well known that the initial fiber misalignment strongly affects kink band onset, and unidirectional compressive strength is very sensitive to the maximum misalignment angle [97, 170]. Selection of misalignment parameters (and the other model parameters) are described in the model calibration section below. The 0 degree plies are prescribed an initial fiber misalignment by defining the integration point orientation with the expression:

$$\psi(z) = \psi_0 \sin\left(\pi\left(\frac{z-z_0}{l}+\frac{1}{2}\right)\right) \tag{3.12}$$

where, z is the material coordinate in the fiber direction, z_0 is the coordinate of the notch tip in the fiber direction, ψ_0 is the maximum initial misalignment angle, and l is the half-wavelength of the function. The expression represents a periodic form similar to the waviness in experimental observations [97, 124]. The variation in orientation corresponds to waviness in the transverse direction (1 axis in Fig. 3.2) and the maximum misalignment angle occurs at the notch tip. Provided that the misalignment half-wavelength is smaller than the fracture process zone, a phase shift in the assumed initial fiber misalignment (where maximum misalignment angle does not align with the notch tip) is not expected to significantly affect the onset of failure.

Splitting regions where cohesive traction can degrade are defined as longitudinal strips tangent to the notch tips in all 0 degree plies. Previous studies in the literature have also employed selectively placed splitting regions based on experimental observations when modeling edge- and center-notched specimens [76, 98, 133]. The splitting regions are meshed with full-integration continuum cohesive elements with uniform thickness of 0.1 μm and side lengths matching the ply mesh in the 2 and 3 dimensions. A linear elastic analysis indicates shear stress concentration in the plies occurring at locations near the notch end but not exactly on the notch tip. As is commonly observed with cohesive models, element lengths along the failure direction should be sufficiently small to capture the fracture process zone [55]. Furthermore, resolving the stress concentration is crucial for predicting split initiation. To address these concerns, a mesh convergence study including nominal element side lengths, h, in the 3 dimension ranging from 40 to 1 μm was performed. Convergence of the stress field is predicted with $h = 10\,\mu$m starting at approximately 70 μm from the center of the notch (mid-height of the specimen). The final simulation element size near the notches linearly increases to $h = 160\,\mu$m at a distance of 2 mm from the center of the notches.

3.2 Results and Discussion

3.2.1 Model Calibration

The calibrated values of the kink band and local damage model parameters as well as the sources of calibration data are listed in Table 3.2. The starting point for the calibration of the physical parameters were the values reported in [31] and the values in [60] were used for the numerical parameters, since these studies employed similar materials. UD DENC experiments were also used in model calibration. Specifically, the unidirectional compression modulus and strength of the specimens (shown in Table 3.3) obtained from the UD DENC tests were used in the calibrations. In these experiments, specimens exhibited brittle failure. Splitting ahead of the notch tips early on is observed which reduced the stress concentrations near the notch tips. The ligament between the notch tips following split formation exhibits a relatively uniform stress that is equal to the load divided by the cross-sectional area between the notch tips. The longitudinal fiber elastic modulus, $E_1^{(f)}$, was calibrated using the rule of mixtures (i.e. $E_{long} = V^{(f)}E_1^{(f)} + (1 - V^{(f)})E^{(m)}$, with 65% fiber volume fraction, $V^{(\mathrm{f})}$, and E_{long} is calculated from the mean linear regression of the load-virtual extensometer data between 0.5 microstrain and 2 microstrain divided by the cross-sectional area between the notch tips.

The UD specimen strength value (calculated as the mean ultimate load of the UD DENC experiments divided by the cross-sectional area between the notch tips) was then used to calibrate the maximum fiber misalignment angle. The model is calibrated by adjusting the maximum initial misalignment angle so that the predicted strength matches the specimen strength The procedure for misaligment angle calibration is as follows: Multiple mesoscale simulations of the UD material were performed by varying the misalignment

Table 3.2: Calibrated parameters of the kink band and local damage model (components designated in the local coordinate axes where the 1 direction designates the fiber direction).

Parameter	Unit	Value	Source	Parameter	Unit	Value	Source
$E_1^{(f)}$	GPa	305.0	UD DENC	$\nu_{12}^{(f)}$	N/A	0.206	[31]
$E_2^{(f)}$	GPa	12.45	[31]	$E^{(m)}$	GPa	3.70	[31]
$G_{21}^{(f)}$	GPa	146.0	[31]	$\nu^{(m)}$	N/A	0.377	[31]
$\nu_{23}^{(f)}$	N/A	0.291	[31]	ψ_0	$^\circ$	1.35	UD DENC
$a^{(m)}$	$\text{MPa}^{-1/2}$	22.5	V-notch Shear	η	N/A	-2.0	[60]
$b^{(m)}$	N/A	17.5	V-notch Shear	c_1	N/A	0.833	UD/V-notch
$\kappa_0^{(m)}$	$\sqrt{\text{MPa}}$	0.0	[60]	c_2	N/A	-35.0	UD/V-notch
R	N/A	-0.006	[60]	w	μm	42.8	DENC

Table 3.3: Experimental and model composite properties.

Property	Experiment	Experimental Mean (standard deviation)	Calibration Simulation Result
Longitudinal Compression Strength (GPa)	UD DENC	1.43 (0.18)	1.43
Longitudinal Compression Modulus (GPa)	UD DENC	206.9 (5.39)	203.0
Ultimate Shear Strength (MPa)	V-notch shear	58.8 (19.1)	55.7
Shear Modulus (GPa)	V-notch shear	6.44 (0.39)	6.40

angle. A least-squares function was fitted to the resulting strength vs. misalignment angle data. The calibrated misalignment angle is read from the fitted curve as the value that corresponds to the mean UD compression strength measured in the experiments. The calibrated misalignment angle is 1.35°. The half-wavelength of the misalignment function is set to $l = 0.5$ mm (approximately 71 times the fiber diameter), which is shown to be a sufficient localization of fiber misalignment for kink band initiation based on the analyses of [60, 102, 169] and the experimental observations in [97, 156].

The stress-strain behavior obtained from 90 degree V-notch experiments were used to calibrate the failure properties of the matrix. The shear chord modulus (computed at 1 microstrain and 2 microstrain) and the ultimate specimen shear strength predicted by numerical simulations and mean experimental results were matched by calibrating $a^{(m)}$ and $b^{(m)}$. The calibration simulations consisted of a mesoscale finite element (a section of composite material) subjected to simple shear. The calibration is performed manually. The outcomes of the calibration simulations are listed in Table 3.3 alongside the experimental values. Given the variability observed in the experiments, reaching a minimum of 95% accuracy in capturing the mean is deemed sufficient to conclude the calibration process. With the calibrated matrix parameters, the resulting transverse composite compression strength is 91 MPa (found by subjecting a mesoscale finite element to uniaxial transverse displacement conditions at the nodes). The value for w used in Eq.3.10 is chosen such that the simulated kink band width is equal to the average kink band width measurements taken from micrograph images of a DENC specimen. The experimental target values and calibration simulation results are presented in Table 3.3. The influence of model parameters on the kink band width and strength predictions is studied in detail in Ref. [60].

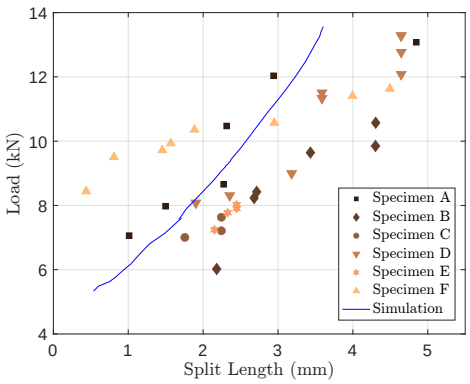

Figure 3.3: Experimental image analysis results overlaid with the calibration simulation result.

The parameters of the cohesive zone model for splitting are also calibrated based on experimental observations and prior data. Table 3.4 shows the mode I and mode II maximum traction and fracture energies used in the simulations. The maximum traction values are estimated in the normal and shear directions based on values used in the literature for carbon-epoxy laminates [134, 165]. The initial stiffness, k_{coh}, is set to 10^5 N mm^{-3} (about 27 times the matrix elastic modulus) on the diagonal components and zero on the off-diagonal components. The stiffness value is on the order of magnitude found to not significantly affect the compliance of the composite while also avoiding convergence issues in [166]. The critical fracture energies for splitting differ from those for delamination that are typically calibrated using double cantilever beam (DCB) and end notch flexure (ENF) tests. In particular, prior investigations determined that the critical mode II fracture energy for splits is approximately 25-40% [91, 116, 133] of measured G_{IIC}^{PC} from ENF tests (*PC* indicates the pre-cracked fracture toughness value). In accordance with these findings, we set G_{IIC}^{s} to be 1/4 the value of measured G_{IIC}^{PC} (=0.502 kJ/m^2). G_{IC}^{s} is set equal to G_{IC} from the DCB test results since other investigations indicate the split initiation and growth to be mode II driven fracture (see again [91, 116, 133]). The BK exponent, β, is set to 1.0 in the absence of critical fracture energy data for the IM7/977-3 material system under mixed-mode interlaminar or intralaminar conditions.

The model includes a pre-existing split ahead of the notch in the 0 degree plies as described above. A sensitivity study was performed to understand the effect of the length of the split introduced on the overall damage evolution behavior. In this study, the plies were assumed to remain elastic. This is consistent with experimental observations below, that indicate that splits are the first major damage event observed under compression. Fig. 3.3 shows the growth of the splits as a function of load amplitude based on the simulations and the experimental observations. The experimental observations are obtained from the analysis of optical images of the experimental DENC specimens. The initial split length and corresponding load level are tracked, providing a coarse representation of the split growth. Simulations were performed with pre-splits of

Table 3.4: Parameters of the cohesive zone model.

Parameter	Unit	Value	Source	Parameter	Unit	Value	Source
k_{coh}	N/mm^3	10^5	[103, 166]	G^s_{IC}	kJ/m^2	0.230	DCB
t^0_I	MPa	60	[134]	G^s_{IIC}	kJ/m^2	0.130	ENF
t^0_{II}	MPa	90	[165]	β	N/A	1.0	Estimate

lengths 0.125, 0.25, 0.50, 1.0, and 2.0 mm from the notch tip. The simulations recover the same curve regardless of the size of the initial split (the discontinuity at split length of 1.71 mm is due to combining results from simulations with short and long initial split lengths recorded from different mesh sizes) indicating that the growth behavior is not affected by the choice of the initial length.

An additional sensitivity analysis was performed to investigate the effect of fracture parameters for splitting on the rate of split growth. In this analysis, simulations were performed by setting G^s_{IIC} to values in the range of 0.10 to 0.20 kJ/m^2 and ultimate traction to values in the range of 90 to 180 MPa. The rate of split growth is found not to be affected significantly by G^s_{IIC} or the ultimate traction values. These parameters were found to have a stronger influence on the load at which splits initiate. This observation is consistent with those reported in [133]. Since the experimental data exhibits large variation, the splitting model is calibrated such that the crack growth curve fits through the mean experimental initial split length and load values. The slope of the load vs. split length predicted by the model falls within the observed experimental data as shown in Fig. 3.3.

3.2.2 Analysis of DENC Behavior

Simulation of the DENC specimen was performed using the calibrated model parameters, and the simulation results were analyzed along with the experimental observations. Figure 3.4a shows the envelope of load vs. strain curves from specimens ran to failure in addition to the interrupted tests and the calibrated simulation prediction. Simulated strains are computed by mimicking the virtual extensometer measurements. The base length of the virtual extensometer is 3.0 mm and the macroscopic strain is calculated as the difference between the average displacements of nodes within a 40 µm radius of the two extensometer ends. In Fig. 3.4b, the histograms for the observation of initial splits, kink bands, and failure in terms of load amplitude in the DENC experiments and simulation are shown. The predicted macroscopic force response is essentially linear until an unstable load drop suggesting an abrupt failure process. The maximum load prediction (13.8 kN) is within the range observed in the experiments (11.7-15.1 kN) and somewhat overpredicts the mean (13.1 kN). The experiment results exhibit a somewhat nonlinear macroscopic load-strain response and the strain at maximum load ranges from 0.37% to 0.54% (mean 0.46%) while the predicted strain at maximum load is 0.42%. The standard deviation of the failure loads and strains is also plotted on Fig. 3.4a.

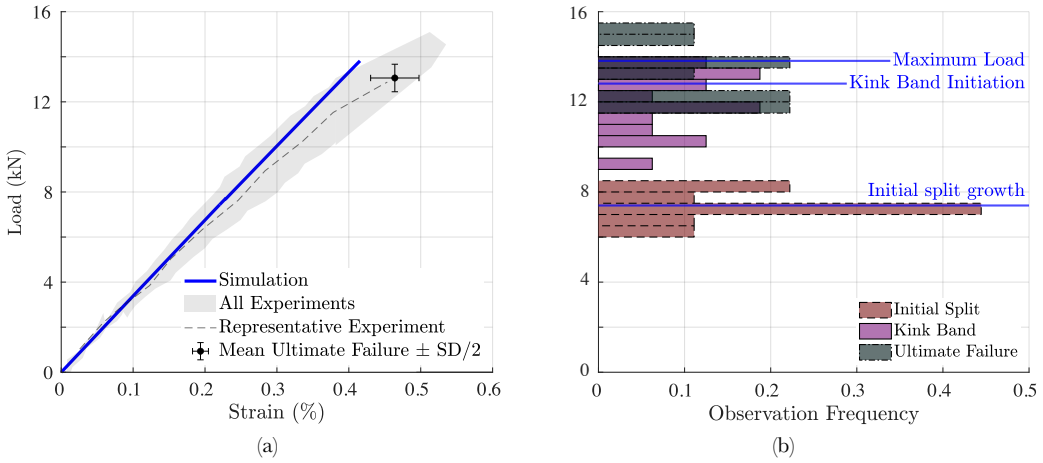

Figure 3.4: (a) Load-strain predictions compared to experimental results; (b) mechanism and failure observation loads (bars) and predictions (annotated solid lines).

Nonlinearity in the DENC experiments initiates early on and continues throughout the loading process until failure, as demonstrated by the representative experiment curve in Fig. 3.4. This nonlinearity is likely due to nonlinear shear effects, although additional mechanisms could be contributing to this behavior as discussed below. Other experimental studies in the literature report similar nonlinearity in the compressive stress-strain response of laminates [23, 99, 148] (e.g., in laminates with high volume fraction of 45 degree plies and when 0 degree plies are not at the mid-plane [99, 148]). The amount of nonlinearity varies with specimen size, presence of off axis plies, ply thickness, and layup.

In the DENC model, the matrix constitutive behavior was calibrated (as described in Section 3.2.1) based on 90 degree V-notch shear tests which exhibit a relatively brittle behavior (specimen failure around 1-2% shear strain). Other experiments including $\pm$ 45 degree tension and V-notch shear [31, 89] show higher ductility, which could better characterize the nonlinear shear behavior of the composite. For instance, Ref. [31] demonstrated an alternative matrix damage model which directly incorporates shear nonlinearity and uses both sets of shear tests to calibrate the matrix model.

Nonlinearity in the fiber behavior was also previously proposed to contribute to the observed nonlinearity of the overall compressive stress-strain curve [104, 145]. The model in Ref. [23] includes nonlinearity in the longitudinal lamina modulus using the empirical relationship from Ref. [93], however the importance of it in determining the nonlinear macroscopic response is not studied. Other studies on multidirectional laminates under compression incorporate fiber damage [22, 31] but predict fiber failure only above 90% of the ultimate load.

Acoustic emission sensors were used to provide additional information on the evolution of damage in the specimens. Acoustic energy-event histories from all of the experiments are shown in Fig. 3.5 where the events

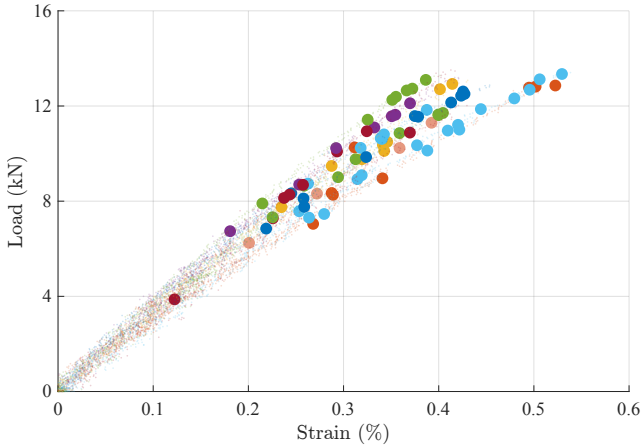

Figure 3.5: Acoustic energy-events during loading in all experiments. The large markers indicate acoustic events meeting or exceeding the observable damage threshold and the small markers indicate acoustic events below the threshold (each color represents a different test).

which meet or exceed the observable damage threshold are plotted with large opaque markers while smaller acoustic energy events are plotted with small faint markers. Smaller acoustic energy events are numerous and present throughout the entire loading process. The earliest damage event observed in the experiments is split formation at the range of 6-8.5 kN. There are relatively few and spread out observable damage events after the onset of nonlinearity. Images from specimens with these readings included evidence of one or more compression failure mechanisms.

Evidence of the failure mechanisms in the 45 degree plies of the test specimens is compared to model predictions in Fig. 3.6. Figure 3.6a shows damage regions in a failed specimen loaded to 13.2 kN. There is a longitudinally-extending damage feature at the left notch while a 45 degree feature present at the right notch. Higher magnification images of the left notch in Fig. 3.6b show details of the damage features observed from the same specimen scanned with dye penetrant introduced. The images include thin matrix cracking patterns in addition to a stepped failure propagation. The stepped feature shown in Fig. 3.6a is also present in Fig. 3.6b Detail 1 (labeled “I”) and likely consists of matrix cracks which migrate around fibers but might also include broken fibers. The saturated area in Detail 1 (labeled “II” in Fig. 3.6b) could be delamination or a dense field of matrix cracks parallel to the 45 degree fibers. In addition to the distinct crack originating at the bottom of the notch in Detail 2 (labeled “III”), there are multiple cracks parallel to the fiber direction above the notch location (labeled “IV”). The highlights oriented perpendicular to the fiber direction in this region are the results of cracks in the adjacent 45 degree ply. The X-ray CT images also include beam-hardening artifacts as indicated in the Fig. 3.6a-b. The artifacts in Fig. 3.6a are caused by the notch edge, which is parallel to the X-ray beam path and spans from the left to the right side of the image. The artifacts in Fig. 3.6b appearing

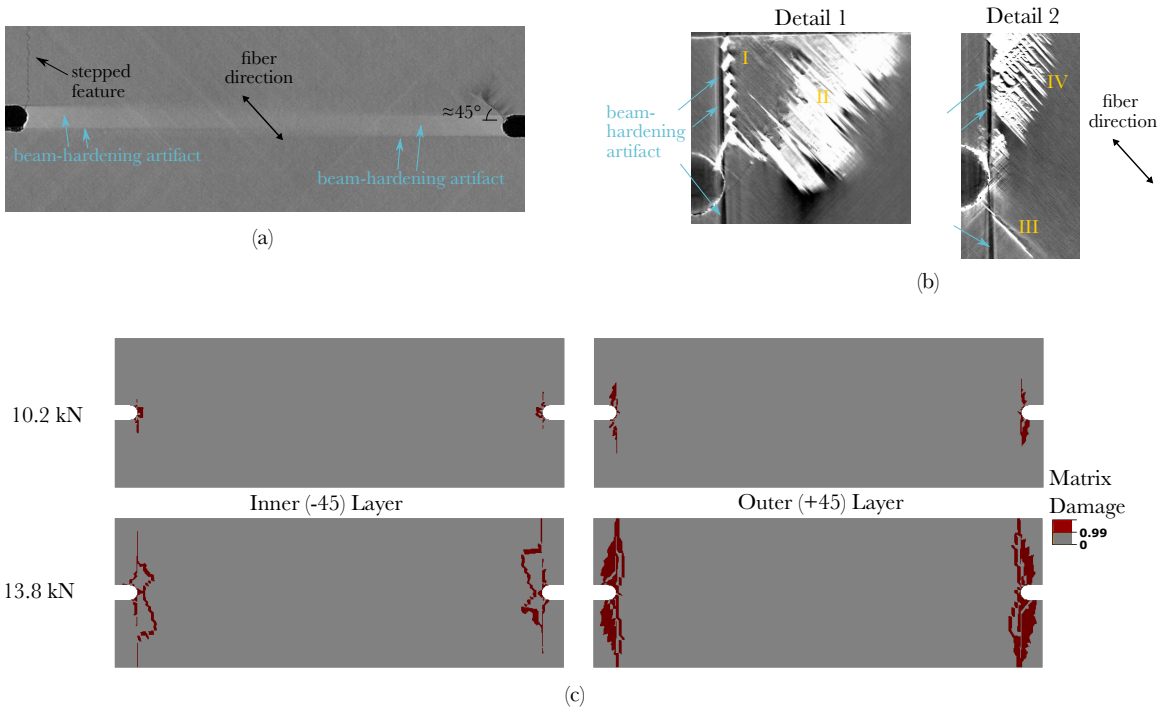

Figure 3.6: (a) Damage in 45 degree plies in an X-ray CT image. (b) Detailed images from scanning with dye penetrant. (c) Predicted damage patterns in the simulation.

as thick and dark vertical strips are caused by the presence of dye penetrant and large variations of the X-ray attenuation within the material of the scanned volume around the notch tip. In comparison, the model predicts matrix damage in the 45 degree plies as shown in Fig. 3.6c. Full matrix damage is present prior to 10.2 kN, and grows from the split. Distinct damage paths are predicted at the ultimate load of 13.8 kN, propagating in the space between the notches. The model also predicts damage along and behind the splits. Overall, the damage contours are similar to the experiment images with dye-penetrant which show a combination of distinctly isolated cracks in addition to different forms of less isolated damage features and paths.

Splitting is observed in the experiments as shown on a representative specimen in Fig. 3.7a and Fig. 3.7c. In the experiments, initial splits (as observed after the first significant AE reading) are 1-2 mm long. Additional splits also develop at higher loads. In the specimen shown in Fig. 3.7a, splitting occurs first on the right notch, followed by the formation of a second and longer split on the left notch. The two splits grow toward the gripped boundaries with increasing loading in a stepwise and non-uniform manner as shown in the datasets in Fig. 3.3. It is not clear if the splits extend under the grips which were not imaged. The simulation predicts a nearly symmetric (due to the symmetry of the numerical specimen) growth of splits at the notches starting at 7.4 kN. The arrows in Fig. 3.7b indicate the split ends and the length evolution is similar to Fig. 3.3. At the load amplitude of 13.3 kN the dominant splits in both the experiment and the simulation are near or at the

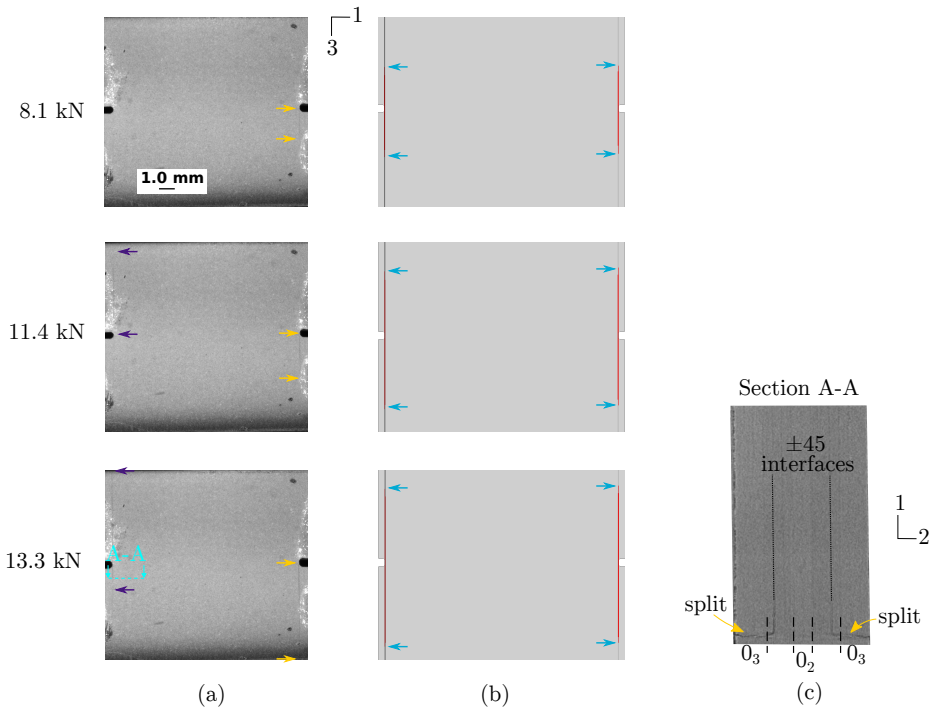

Figure 3.7: Split evolution in the exterior plies in the (a) experiments and (b) simulation (arrows indicate ends of the splits). (c) Through-thickness splitting in an X-ray CT image from the experiment.

gripped boundaries. The lack of symmetry of the split formation and growth in the experiments is attributed to nonuniformity in the material. The shear concentration site on the notch with the weakest material will be where the first split forms. Additional split nucleation and split growth is dictated by the stress redistribution thereafter. The highlighting from the dye penetrant in X-ray CT images in Fig. 3.8a-b demonstrates the most frequently observed splitting pattern in the 0 degree plies at loads over 13 kN. Splits are consistently present in the exterior plies and observed with much less frequency in the interior 0 degree plies. The simulation also predicts prominent splitting in the exterior plies, and the predicted split growth is smaller in the interior 0 degree layer as shown in Fig. 3.8c.

Figure 3.9 shows the longitudinal strain fields in the exterior and interior 0 degree plies during the simulation near the predicted failure load. The simulation predicts the onset of the kink band at the interior 0 degree ply around 12.8 kN (92.7% of the ultimate load). There is a progressive and steady propagation of the kink band from the onset until the ultimate load is reached. Concentration of higher magnitude longitudinal strains ahead of the notch tip is evident in the interior ply plots. The strains immediately above and below the formed kink band are relaxed behind the kink band front. The propagation then accelerates and instantaneously leads to specimen failure. In the experiments, the nucleation time of the kink bands cannot be determined with accuracy since kink band observations were made in interrupted tests, which were not taken to failure, since

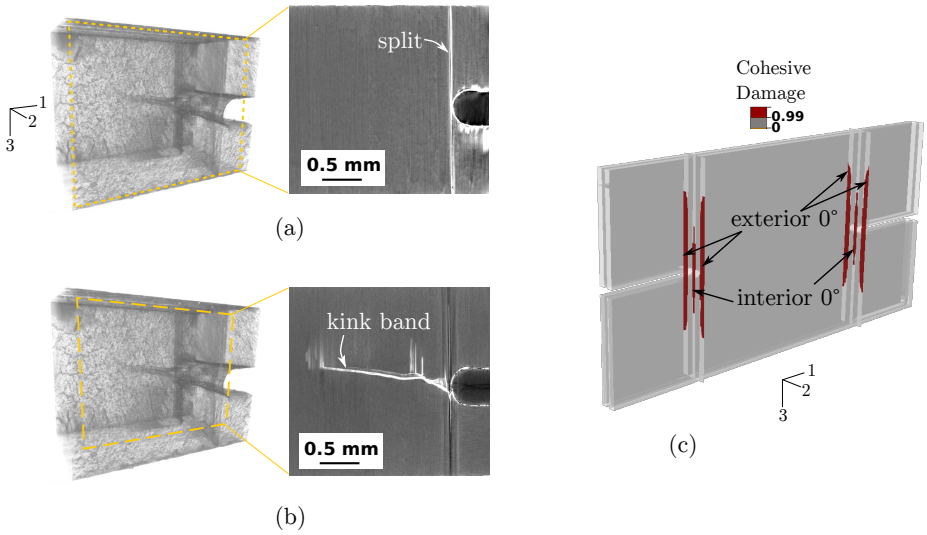

Figure 3.8: X-ray CT images of a dye penetrated specimen loaded to 13.2 kN showing (a) splitting in the exterior 0 degree ply and (b) kink band interior 0 degree ply. (c) Through-thickness splitting predicted at ultimate load.

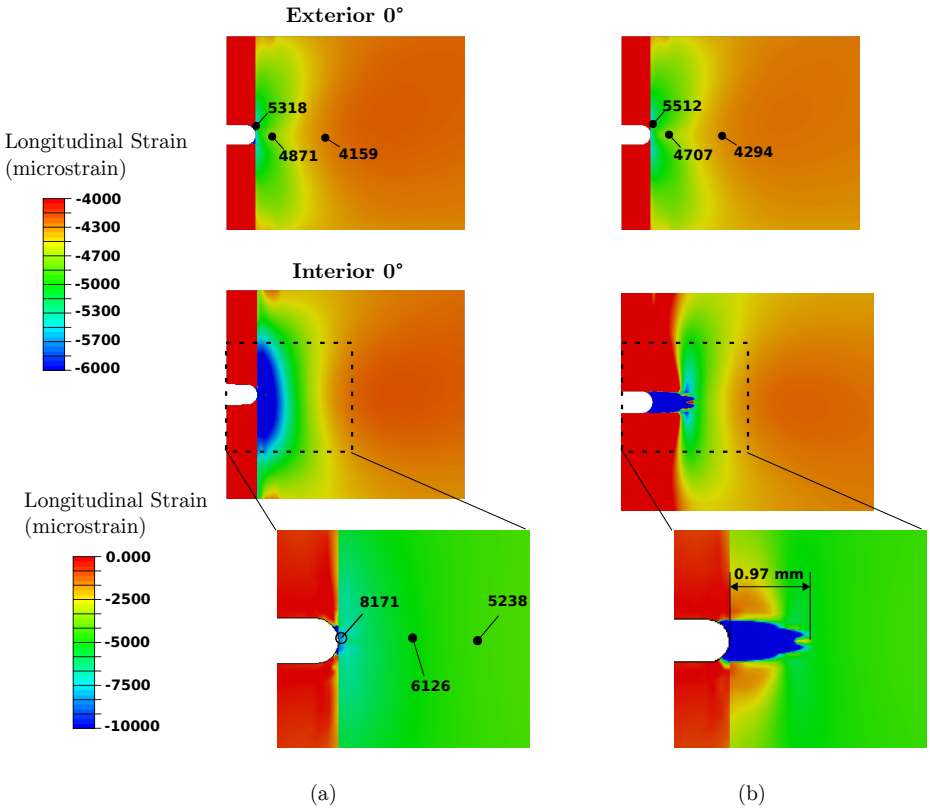

Figure 3.9: Predicted longitudinal strain fields in the 0 degree plies at (a) 92.7% of the ultimate load and (b) ultimate load. Strains are reported in the global coordinate system.

these specimens were sacrificed to sectioning for kink band characterization. Kink bands are observed in the experiments starting in specimens reaching loads of 10.6 kN and higher. The predicted macroscopic strain at kink band initiation of 0.38% lies towards the upper bound of strains experienced in the experiments at loads around 10.6 kN (0.29-0.40%). The large range of strains associated with observed kink band formation implies that there is variability in the failure onset time. The majority of specimens did not show formation or propagation of kink bands in the exterior 0 degree plies and an example of the through-thickness kink band presence is shown in Fig. 3.8a-b. The longitudinal strain in the middle 0 degree plies of the specimen is shown in Fig. 3.10a with close up profiles of matrix damage in the cross-section ahead of the notch (Section A-A) and at the kink band tip (Section B-B). The damage patterns reflect what is observed in the experiments, where micrograph sections show clear matrix cracking in the plus/minus 45 degree and 90 degree plies near the root of the kink band ahead of the notch as shown in the micrograph section Fig. 3.10b and only the kink band further away from the notch like shown in Fig. 3.10c. The experiment images in Fig. 3.10b-c clearly show that the primary kink band propagation occurs in the interior 0 degree ply only and additional numerical simulations we performed suggests that splitting affects the observed behavior. For instance, in the absence of splits the kink bands initiate in the exterior plies first, around 7.9 kN, and propagate ahead of later-initiating kink bands in the interior plies until failure. Suppressing splitting results in a significant under-prediction of the failure load (8.3 kN) and the strain at failure (0.33%) pointing to the relaxation induced by the splits. Splits forming 20-50 μm behind the notch tip increases the load and strain at failure but still under-predicts the experimental range.

X-ray CT images additionally suggest delamination between the 0 and 90 degree plies connected to the ends of the kink band as shown in Fig. 3.11a. The delaminations present at the 0-90 degree ply interface extend parallel to the kink band propagation and likely formed to accommodate the discontinuity induced by the kink band ends. These delaminations were not modeled explicitly in the simulations. Incorporating this mechanism with cohesive elements results in convergence issues and excessive computation times making the analysis infeasible. Zooming into the model prediction at the kink band tip, Fig. 3.11b-c show the shear strains in the through-thickness cross section. There is significant shearing (ε_{12} and ε_{23}) present at the 0-90 degree ply interfaces at the ends of the kink band. This information suggests that the onset of delaminations is likely shear driven. The 45 degree plies experience shearing (ε_{23}) as well, coinciding with the predicted matrix damage pattern in Fig. 3.10a, Section A-A, suggesting that the damage at the $\pm$45 degree interface visible in Fig. 3.11a and Fig. 3.7c is shear driven.

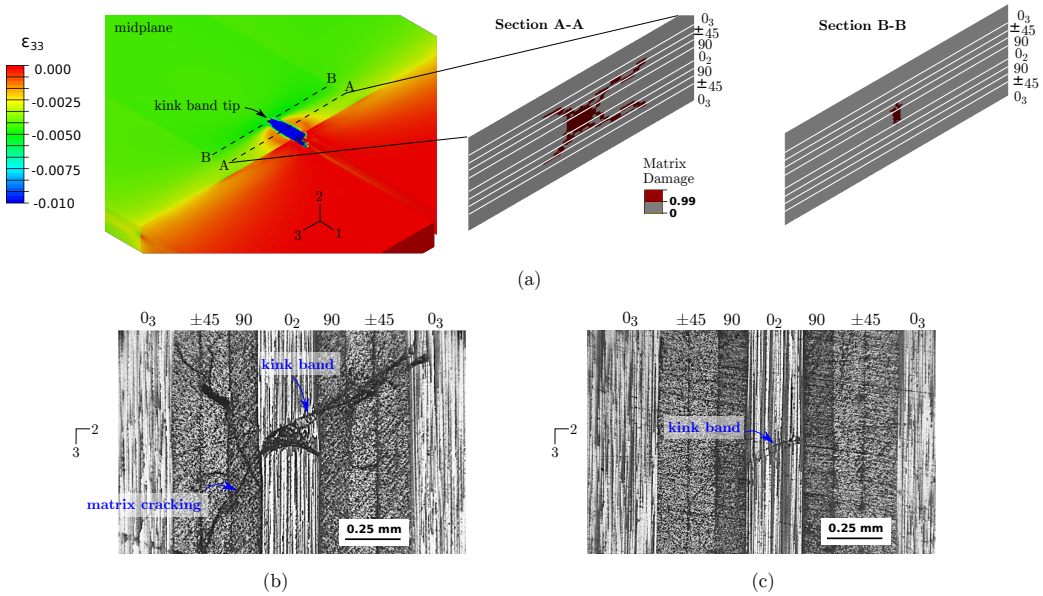

Figure 3.10: (a) Damage prediction in a cross-section parallel to the 2-3 plane. Micrographs of the same perspective in a specimen loaded to 12.9 kN located (b) just ahead of the notch and (c) at the kink band tip (approx. 2.1 mm ahead of the notch tip).

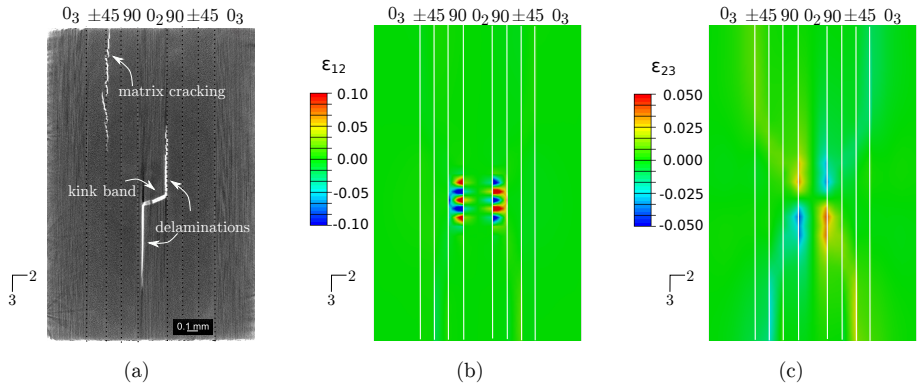

Figure 3.11: (a) X-ray CT image of the same perspective in Fig. 3.10 and within the kink band. Predicted shear strain (b) 1-2 and (c) 2-3. Strains are reported in the global coordinate system.

3.3 Conclusions

Analysis of images from DENC experiments provide some indication of the load levels where splitting and kink bands are present. Simulation results point to the capabilities of the multiscale modeling approach and enhance the understanding of these failure mechanisms in the DENC ultimate failure while greatly reducing computational cost compared to a direct numerical simulation of fibers and matrix. The lamina behavior in the model was calibrated using UD-DENC compression and V-notch shear properties. Measurements from micrograph and optical images were used to select parameter values related to kink band width and splitting behavior. The model predicts the DENC failure load within the range of experimental values and shows how the critical failure mechanism of kink bands occurring primarily on the interior of the specimen, and interior and exterior occurring subcritical damage features interact during the failure process. Among the consistently observed failure mechanisms, splitting is particularly important as the formation of splits directly alters the stress distribution around the notches. Matrix cracking in the 45 degree plies is predicted to accompany splitting just ahead of the notches in agreement with experimental cross-sectional images obtained from specimens loaded to ultimate failure. The onset of matrix damage is not clear from the experimental images but the model predicts early onset around the onset time of splits. Together, these precursors to ultimate failure contribute to the load range where instability of the inner 0 degree layer results in kink band initiation around 93% of the ultimate predicted macroscopic load and propagation between both notches. Splits not present or forming behind the notch tip result in an under-prediction of the experimentally observed kink band and ultimate loads.

The numerical predictions suggest that the simultaneous presence of matrix cracking, exterior ply splits and kink bands should be considered in modeling laminates with exterior 0 degree plies in order to accurately capture the apparent strength and failure propagation. Additionally, while delamination is not included in the final simulations due to excessive computational demand, significant shear straining is predicted at the 90-0 degree ply interfaces and 45 degree plies prior to ultimate load. Without predicting the progression of delamination, the model predicts kink band propagation as the cause of ultimate failure, matching experimental observations which also indicate the subcritical nature of delaminations (occurring at the interfaces bounding the primary kink band [45, 148]).

CHAPTER 4

Z-pinned Interface Model Development and Calibration

As presented in the literature review, z-pins have been demonstrated to increase delamination resistance in composites through mechanisms including z-pin pull-out, bending, and fracture. The failure mechanisms depend on the magnitude of axial and shearing stresses on the z-pin resulting from crack opening and sliding between the lamina on either side of the delamination, i.e. local interlaminar mode-mix. Even under relatively simple loading conditions, these complex failure mechanisms result in what could be described as a mixed-mode delamination at the laminate scale. Under pure Mode I conditions, the stress at failure onset is determined only by shear strength along the z-pin - lamina interface which is related to the length of the z-pin resisting pull-out. Failure occurs when the interface opens enough so that the z-pin is pulled out from the sub-laminate. Under mixed-mode conditions, the failure onset is the result of shear and bending resistance of the z-pins in addition to the z-pin - lamina interface strength. The separation at failure is a consequence of z-pin pull-out or z-pin fracture due to bending. Some degree of pull-out may occur prior to z-pin fracture. Failure onset under pure Mode II conditions is associated with shear resistance of the z-pins as well as the resistance of the laminate to ploughing. Shear strain at failure of the z-pin and the the distance into the laminate the z-pin has ploughed determine the separation at failure.

ILF experimental configurations provide the macroscopic response resulting from delamination in the presence of z-pins under averaged mode-mix conditions. These experimental configurations offer an advantage in that the influence of the matrix interface is included in the overall response, which is not the case in single z-pin characterization and FWT configurations (there is Teflon film in the interface except on the z-pin). Additionally, the influence of neighboring z-pins is also included, which can affect the local mode-mix. Results from ILF experiments have been used to verify and validate micromechanical models of z-pins but have not been used for calibration of a CZM for z-pinned interfaces. The current work presents the calibration and validation of a CZM for the prediction of delamination in z-pinned composite interfaces under pure and mixed-mode conditions. A trilinear constitutive law is employed to describe the delamination of z-pinned composites under any interlaminar mode-mix. Finite element models are constructed to match experiments performed on z-pinned CFRP composite specimens with delaminations at the mid-length of the z-pins and mid-height of the laminate thickness. DCB and ENF test configurations provide pure Mode I and Mode II delamination conditions while MMB and single leg bend (SLB) tests provide intermediate mode-mix delamination conditions. The constitutive law properties are calibrated using the macroscopic force-displacement experimental results and crack propagation observations. Analysis of the numerical and experimental tests

provide insights into mixed-mode delamination propagation in z-pinned composites.

4.1 Trilinear Constitutive Law

The constitutive law describes the z-pinned interface behavior in the form of a traction-separation relationship. This traction-separation law (TSL) is a function of interlaminar mode-mix, which is expressed in terms of the Mode I separation (normal to the interface plane), δ_{I}, and the Mode II separation (tangential to the interface plane), δ_{II}, by the following relationship:

$$B = \frac{\delta_{\mathrm{II}}^2}{\delta_{\mathrm{I}}^2 + \delta_{\mathrm{II}}^2} \tag{4.1}$$

Softening evolves as a function of the effective separation defined as $\hat{\delta} = \sqrt{\delta_{\mathrm{I}}^2 + \delta_{\mathrm{II}}^2}$. The two softening stages are stored in an effective traction variable, $\hat{t}$, and computed for a given mode-mix, B, using the following equations:

$$\phi^{(1)} = \frac{\hat{\delta} - \hat{\delta}_B^0}{\hat{\delta}_B^I - \hat{\delta}_B^0} \tag{4.2}$$

$$\phi^{(2)} = \frac{\hat{\delta} - \hat{\delta}_B^I}{\hat{\delta}_B^f - \hat{\delta}_B^I} \tag{4.3}$$

$$\hat{t}_B = \begin{cases} k\left(\hat{\delta} - \phi^{(1)}\hat{\delta}_B^I\right) + \phi^{(1)}\hat{t}^I, \ \hat{\delta}_B \leq \hat{\delta}_B^I \\ \hat{t}_B^I\left(1 - \phi^{(2)}\right), \ \hat{\delta}_B > \hat{\delta}_B^I \end{cases} \tag{4.4}$$

where $\hat{\delta}_B^0$, $\hat{\delta}_B^I$, and $\hat{\delta}_B^f$ denote the effective separation at damage onset, softening slope change, and interface failure (i.e. complete debond; there are two interlaminar surfaces free to move with respect to each other), respectively. The Mode I and Mode II traction components are then defined as follows:

$$t_{\mathrm{I}} = \hat{t}_B\sqrt{1-B} \tag{4.5}$$

$$t_{\mathrm{II}} = \hat{t}_B\sqrt{B} \tag{4.6}$$

The softening history is stored in the cumulative damage variable, $\Phi^{\max} = \max_{[0,\tau]}\{\Phi_B(\tau), \Phi^{\max}\}$, where the current time of loading is denoted by τ, and $\Phi^{\max} = 0$ prior to softening. The current damage is calculated

using the effective traction-separation response and degrades the traction components:

$$\Phi_B = 1 - \hat{t}_B/(k\hat{\delta}_B) \tag{4.7}$$

$$t_{\mathrm{I}} = (1-\Phi_B)k\delta_{\mathrm{I}} \tag{4.8}$$

$$t_{\mathrm{II}} = (1-\Phi_B)k\delta_{\mathrm{II}} \tag{4.9}$$

The traction-separation response also follows a linear unloading and reloading path from the tractions associated with maximum damage to the zero traction-zero separation state. Damage evolves when $\Phi_B(\tau) > \Phi^{\max}$. Mode I and Mode II energy components are calculated based on the current separation and maximum damage state by integrating under the reloading curve:

$$G_{\mathrm{I}} = \int_0^{\delta_{\mathrm{I}}} t_{\mathrm{I}}(\Phi^{\max})\, d\delta_{\mathrm{I}} \tag{4.10}$$

$$G_{\mathrm{II}} = \int_0^{\delta_{\mathrm{II}}} t_{\mathrm{II}}(\Phi^{\max})\, d\delta_{\mathrm{II}} \tag{4.11}$$

Using these definitions, the interlaminar mode-mix definition can also be expressed in the energy sense [39, 165]:

$$B = \frac{G_{\mathrm{II}}}{G_{\mathrm{I}} + G_{\mathrm{II}}} = \frac{\delta_{\mathrm{II}}^2}{\delta_{\mathrm{I}}^2 + \delta_{\mathrm{II}}^2} \tag{4.12}$$

Figure 4.1 illustrates the constitutive law for mixed-mode separations. The initial loading regime is controlled by an elastic constant, k (numerical parameter chosen to be large enough to provide a reasonable stiffness but small enough to avoid numerical problems, such as spurious traction oscillations [166]) and softening begins upon satisfaction of the damage initiation criterion

$$\left(\frac{\delta_{\mathrm{I}}}{\delta_{\mathrm{I}}^0}\right)^2 + \left(\frac{\delta_{\mathrm{II}}}{\delta_{\mathrm{II}}^0}\right)^2 = 1 \tag{4.13}$$

where δ_{I}^0, δ_{II}^0 are associated with damage onset of the unpinned interface under pure mode conditions (i.e. $\delta_{\mathrm{I}}^0 = t_{\mathrm{I}}^0/k$ and $\delta_{\mathrm{II}}^0 = t_{\mathrm{II}}^0/k$). The effective separation at damage onset is calculated according to the ratio of the interlaminar mode-mix displacements (see Ref. [107] for the derivation).

$$\hat{\delta}_B^0 = \left(\frac{1-B}{(\delta_{\mathrm{I}}^0)^2} + \frac{B}{(\delta_{\mathrm{II}}^0)^2}\right)^{-1/2} \tag{4.14}$$

Following Ref. [107], the intermediate critical separation, $\hat{\delta}_B^I$, is related to the physical interlaminar frac-

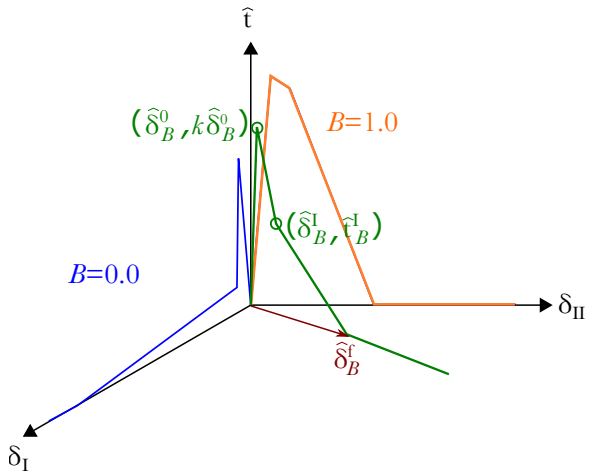

Figure 4.1: Trilinear TSL under any mode-mix condition.

ture toughness of unpinned specimens, $G_C^{(unp)}(B)$, and effective separation at damage onset as follows:

$$\hat{\delta}_B^I = \frac{2G_C^{(unp)}(B)}{k\hat{\delta}_B^0} \tag{4.15}$$

The effective traction, t_B^I, and separation at failure, δ_B^f, are associated with bridging mechanics/failure of the z-pins. These critical traction and separation parameters need to be calibrated for mixed-mode conditions.

4.2 Calibration of the Trilinear TSL

4.2.1 Experimental Method

4.2.1.1 Materials and Specimens

Calibration experiments were performed at the AFRL. To manufacture ILF test specimens, panels were hand-laid with 24 plies of UD IM7/977-3 prepreg tape using standard procedures and tools in an OEM-spec clean room. The outer dimensions are shown in Fig. 5.8a. Plies were tacked together using a non-stick roller and debulked under vacuum at approximately 120 degree Fahrenheit every 3 plies. After 12 plies, a 0.005 inch thick Teflon film is placed in the stack at a specified distance as shown in Fig. 5.8a. The final specimen configuration is depicted in Fig. 5.8b and designed with a region of orthogonally inserted z-pins. One set of panels was sent to a third party where T650-42/epoxy z-pins with D =0.51 mm diameter were inserted with a mechanical gurney at 64 pins/in^2 in the region indicated. Following z-pinning the panels were autoclave cured like the unpinned panels. The typical autoclave curve cycle used is shown in Fig. 4.3 including the low thermocouple temperature, vessel pressure, and bag vacuum pressure all on the same graph. After curing, it was observed that the z-pins were not orthogonal to the lamina surface and a manufacturing error that is present in all specimens.

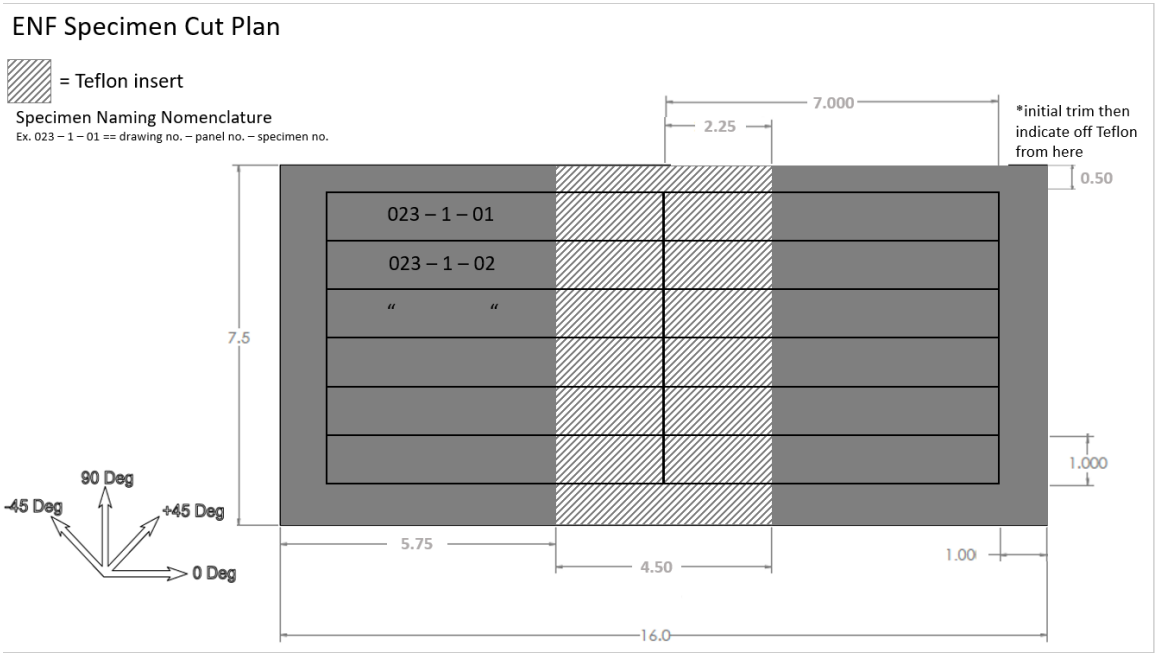

(a)

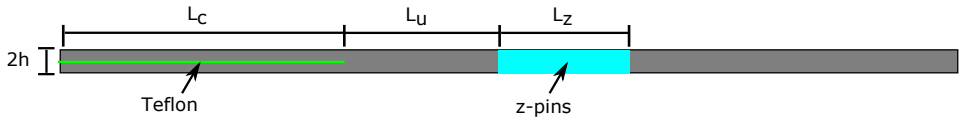

(b)

Figure 4.2: (a) Laminate panel cut plane and (b) specimen schematic.

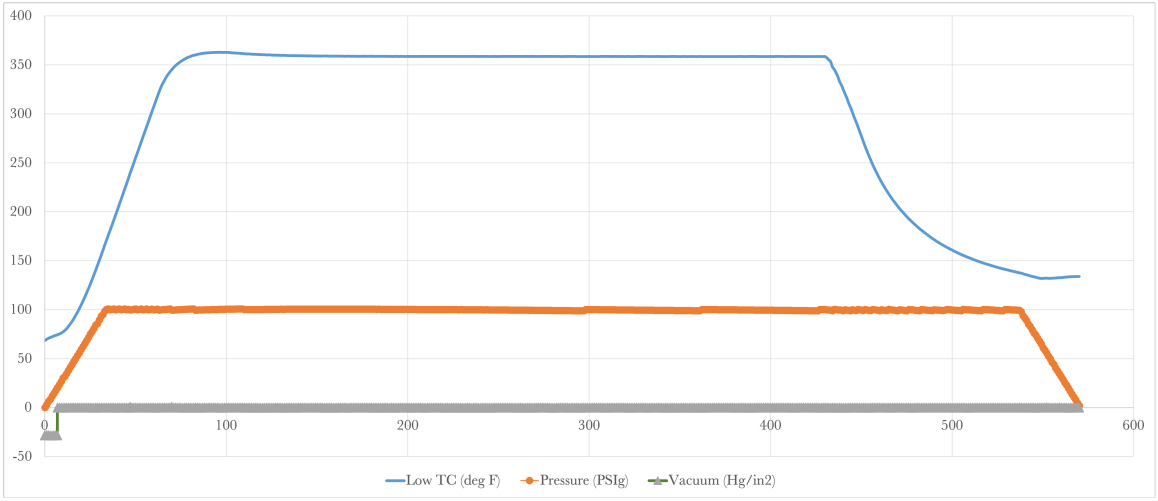

Figure 4.3: Laminate cure cycle.

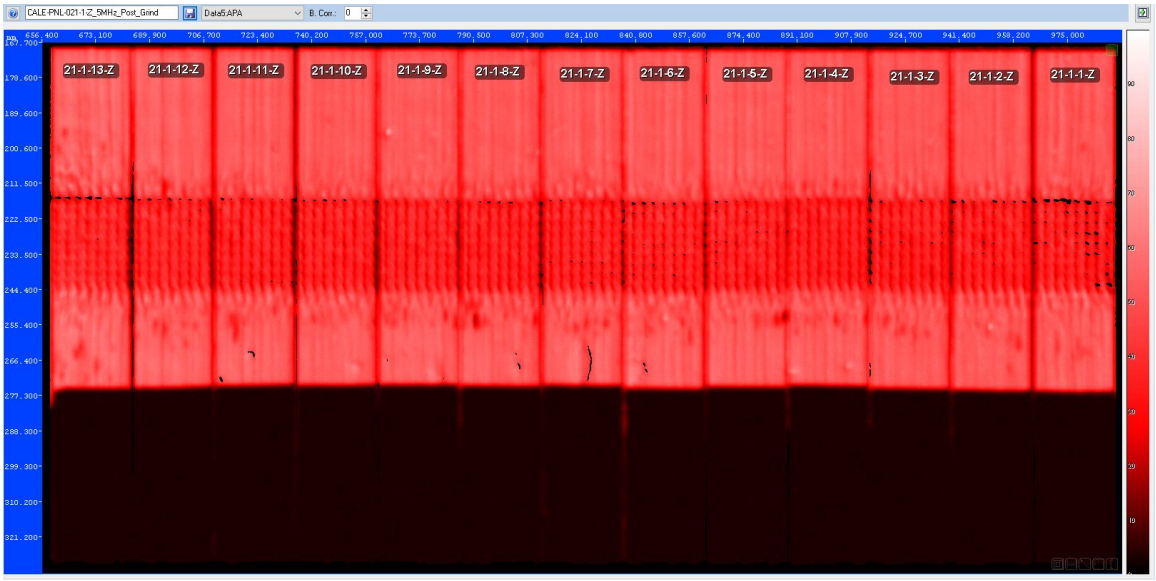

Figure 4.4: Ultrasonic c-scans of the excised specimens (panel 21).

A total of 26 specimens were excised from the unpinned panels and 26 from the z-pinned panels using water jet cutting with the dimensions shown in Fig. 5.8a-b. The specimens share the same nominal dimensions and fit the requirements of Double Cantilever Beam [11] (DCB), End-Notched Flexure [8] (ENF), and Mixed-Mode Bend [12] (MMB) configurations: 177.8 mm length by 25.4 mm width by $\approx$ 3.2 mm thickness (L x W x h). Ultrasonic C-scans were performed on the specimens to inspect for damage induced during the manufacturing process. Figure 4.4 shows some of the z-pinned specimens. The fully dark region shows the extent of the teflon film. The images showed no obvious inconsistency and the specimens were deemed acceptable (without defect). Each specimen was also measured. The maximum deviation from the specified dimensions is 0.381 mm for the specimens excised from one panel (L x W x h) and 0.254 mm for the specimens excised from the other panel (W x h); the length deviated by up to 2.4 mm in the second panel due to a biased water jet cut. Each specimen was painted on its edge and then laser etched with a 1 mm resolution scale, with marks approximately 1/8 inch wide.

Specimens were also prepared for unidirectional compression testing according to the Combined Loading Compression (CLC) test method [10]. The nominal dimensions of the specimens are 139.7 by 25.4 by 2.92 mm. The thickness is smaller than the ILF specimens due to a manufacturing error. The gage section is a z-pinned region 13 mm long and 25.4 mm wide. Tabs were applied to the remaining sections of the specimens.

Table 4.1: Characterization experiment test matrix.

Test	Qty. (Successful)	Stop Criterion
Unpinned Tests		
DCB	3 (3)	Fracture
ENF	5 (5)	Delamination at load roller
MMB	20 (14)	Delamination at load roller
Z-pinned Tests		
DCB	3 (1)	Fracture
ENF	3 (2)	Delamination at load roller
MMB	9 (4)	Delamination at load roller
SLB	4 (2)	Delamination through the z-pin field

4.2.1.2 Tests

To characterize Mode I properties, the DCB experiment was employed and the test procedure in [11] was followed using load blocks adhered to the specimen arms. The End Notched Flexure (ENF) experiment was employed to characterize Mode II properties following the test procedure in [8]. The configuration is essentially a 3-point bend setup. Mixed-mode properties were characterized using the MMB and Single Leg Bend (SLB) configurations. The MMB tests were conducted according to the procedure in [12] using piano hinges bonded to the specimen arms. The SLB tests were conducted like the ENF tests, but the specimen geometry is modified so that one end of the specimen is supported on the bottom of the upper arm while the other end is supported on the bottom arm. Table 4.1 summarizes the tests performed for the unpinned and z-pinned specimens, including quantity and stop criterion. Some tests were not successful due to bond failure between load introduction tabs and specimens, the crack did not advance. Table 4.2 shows the mode-mix, corresponding lever arm length, and quantity of accepted tests. Due to the manufacture of the specimens (space between teflon end and beginning of z-pin field), the parameters are adjusted from the standard for the z-pinned specimens. In particular, the initial delamination was fixed to $a = 25$ mm when hinges were bonded to 10 specimens. This leaves the z-pin field past the top load roller as shown in Fig. 4.5a. A larger span between the hinges and the top load roller which I designate L_1 is used so that some of the z-pin field lies ahead of the top roller as shown in 4.5b. The second span is kept equal to the standard value, $L_2 = 50$ mm. The fixture design according to the Appendix X.2 [12] limits the first span to $L_1 = 77.4$ mm. The equations used to relate length of the lever arm (see equation 5 in Section 11 of [12]) to the global mode-mix is no longer applicable and mode-mix is evaluated for different lever arm lengths using FE simulations. The model used for the simulation and results are discussed in the subsequent modeling methods section. The curves in Fig.4.6 show the mode-mix as the delamination propagates through the z-pin field. The non-steady mode-mix is also present using the standard configuration (see e.g. [95, 136]) and the constant decrease in mode-mix behind the load roller does not reflect consistent mode-mix conditions.

Table 4.2: Summary of the mixed-mode experiments.

Unpinned			Z-pinned		
B	Qty.	c (mm)	B	Qty.	c (mm)
0.20	5	95.73	0.148	2	35.0
0.40	5	49.83	0.279	2	25.0
0.60	5	35.63	0.453	2	N/A
0.80	5	27.13			

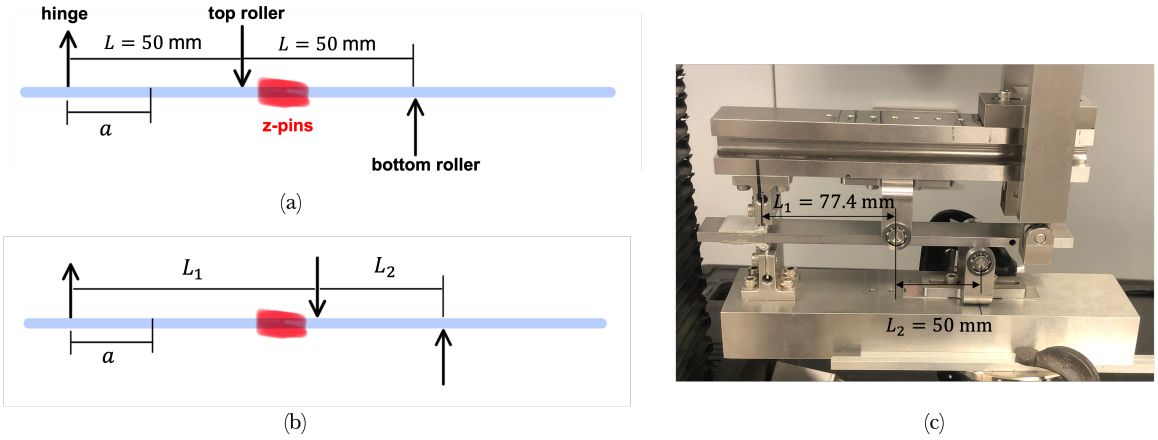

Figure 4.5: Schematics of the fixture connections relative to the z-pin field in the (a) standard MMB configuration acc. to ASTM D6671 and (b) altered test configuration. (c) Photo and dimensions of the test configuration.

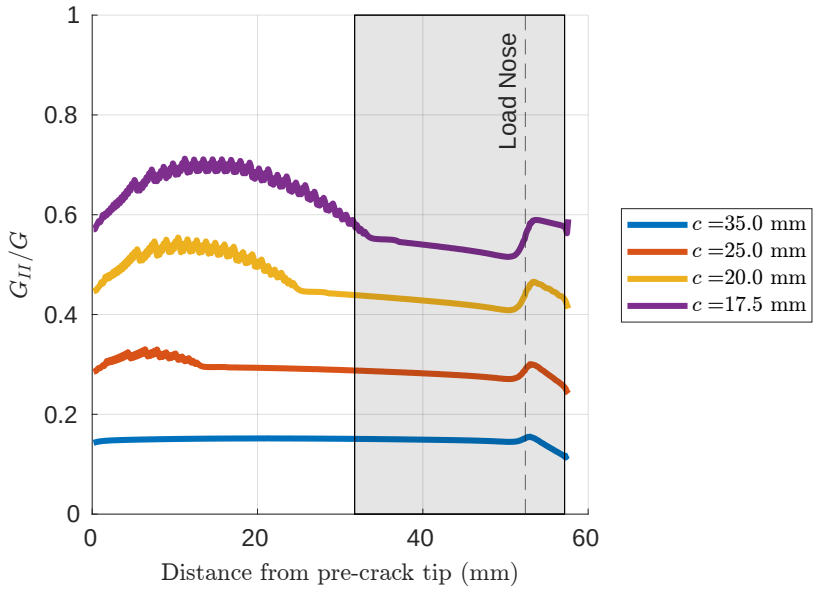

Figure 4.6: Mode-mix vs. delamination propagation for z-pinned MMB tests.

The interlaminar characterization tests were conducted on 1.0-22 kip hydraulic and electro-mechanical test frames with actuator displacement and load cell data recorded at 10 Hz in addition to video recording captured at 0.25 Hz to monitor crack growth visually on the edges of the specimens. Additional images of the ILF specimens were acquired post-mortem using a Dual Beam Focused Ion Beam - Scanning Electron Microscope (ThermoScientific Helios FIB-SEM).

The UD compression tests were conducted on a 2.2 kip hydraulic test frame according to the standard CLC test method [10]. Load and displacement from the test frame as well as strain readings from front and rear strain gages were recorded at 10 Hz. Post-mortem photographs were also taken.

4.2.2 Computational Method

4.2.3 Modeling Approach

Numerous benchmark examples for delamination propagation prediction under pure and mixed-mode conditions were studied in [95] and the results showed that the overall behavior of ILF configurations in 2D and 3D simulations matched. For this reason 2D finite element models were deemed sufficient for the calibration procedure. The composite arms of the specimens are meshed with Plane Strain Elements with Incompatible Mode (CPE4I in Abaqus) [96, 134], which are chosen to capture the in-plane bending behavior experienced in the tests. There are 4 elements through each arm thickness. The arms are assigned orthotropic elastic material behavior. The interface behavior is modeled using cohesive surface interaction with the finite-sliding and node-to-surface formulation. This approach naturally accommodates the large separations (on the order of h) and rotations of the specimen arms expected prior to complete z-pinned interface failure. Slave nodes are tracked along a master surface. While there is no computational expense associated with Gaussian integration (with continuum elements), "internal" contact elements are generated, adding to the total model DOF. There is flexibility in meshing between interfaces, unlike with conventional cohesive elements. Aspects like tracking thickness and sliding extension zone can also be controlled to account for large opening or sliding relative displacements (this is advantageous to enforce limited tracking if there is only small separation expected). A disadvantage to the computational expense is the interpolation of the slave node position on the master surface to track the relative displacement/separation between surfaces. The initial interface thickness is exactly the geometric zero, an appropriate scenario for TSL constitutive description. The unpinned interface region is modeled using a bilinear TSL. The linear softening begins upon satisfaction of the quadratic separation criterion. The z-pinned interface region is modeled using the trilinear TSL.

For implementation of the trilinear constitutive law using the built-in CZM in Abaqus, the cumulative damage variable evolution as a function of the difference in effective separation from the effective separation at damage onset must be provided (i.e., damage is a function of $\hat{\delta} - \hat{\delta}^0$). An important consideration in

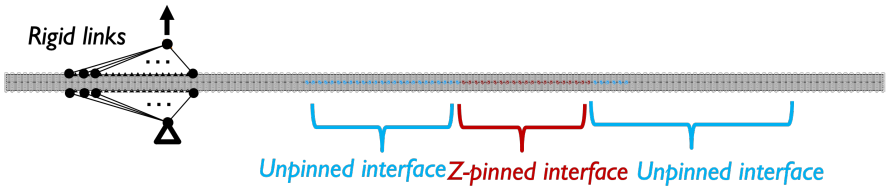

Figure 4.7: DCB model geometry and boundary conditions.

implementing the model this way is that the damage evolution is provided in a tabular format sampled from Eqn. 4.7. Abaqus linearly interpolates between damage values in the provided table(s) which due to the representation of damage as stiffness degradation results in a very quick initial damage evolution compared to the change in effective separation. The damage evolution is much slower for high values of damage (about 99% and larger). The consequence is that the damage table must be provided in a manner such that large errors do not result from the linear interpolation. A nonuniform sampling algorithm is employed which evaluates the errors between the linear interpolation and exact traction values. A traction error threshold of 0.1% error reduces the data from thousands of uniformly sampled points to hundreds. Using a user-subroutine to directly implement the model analytically in Abaqus was also explored. Numerical difficulties were encountered during preliminary work which were related to the onset of damage. The existing "black-box" capabilities of Abaqus were chosen to handle the convergence issues resulting from the highly nonlinear and quick change in cohesive stiffness.

4.2.3.1 Mode I Properties

The geometry and boundary conditions for the DCB simulations is shown in Fig. 4.7. Mimicking the steel block bonded to the top specimen arm, the load is introduced from a reference point connected by rigid links to surface nodes. The same method is applied to the fixed support of the bottom arm. Implicit analyses are performed and three uniform meshes with three different element lengths are tested for mesh convergence. Example results are shown in Fig.4.8. The element length for calibration should be no greater than 0.635 mm. The model did not experience numerical issues though the initial peak and softening slope were found to be sensitive to the load increment. This sensitivity was not observed to the same degree in the other models to be discussed.

4.2.3.2 Mode II Properties

The geometry of the specimen is the same as before but the boundary conditions are changed as shown in Fig. 4.9. Sections of the bottom specimen surfaces are assigned to contact pairs with the analytical rigid supports where hard contact is enforced. The load roller is mimicked by displacing the nodes centered

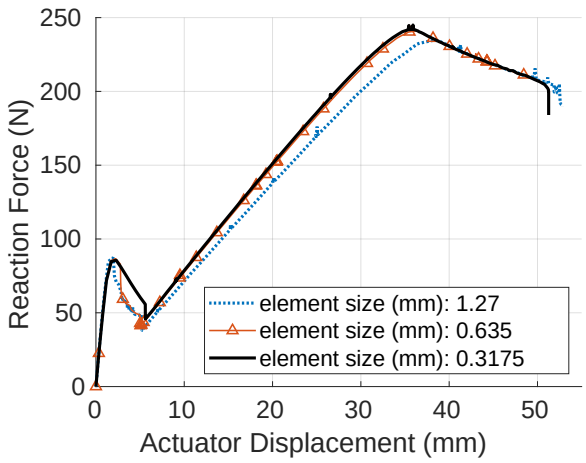

Figure 4.8: Mesh convergence of the DCB model.

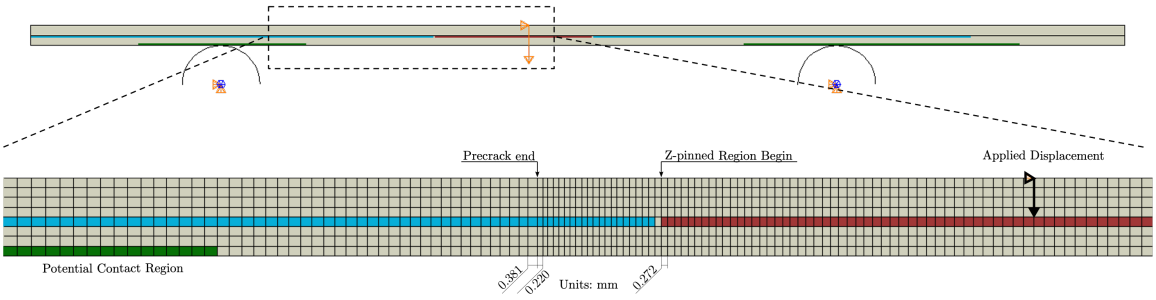

Figure 4.9: ENF model and mesh refinement details.

between the supports [117]. The interface behavior is modeled as in the DCB simulations. Mesh convergence was studied as before but the mesh was additionally refined ahead of the precrack tip to try to better resolve the initial peak. The mesh is biased a ratio of 0.9 resulting in element lengths range from 0.22 to 0.52 mm between the precrack and the end of the z-pinned region. A portion of this mesh is shown as shown in Fig. 4.9. The mesh sensitivity results are shown in Fig. 4.10. The load drop can be reduced with a very fine mesh, however convergence of the initial peak load is observed here with the minimum element size of 0.22 mm at the precrack end.

4.2.3.3 Mixed-Mode Properties

The uniform coarse mesh for the specimen is like presented in the previous sections. The lever fixture is modeled using rigid elements. The top piano hinge connection is modeled using multi-point constraint on the displacement degrees of freedom at the node at the end of the lever. The bottom piano hinge connection is modeled by constraining the displacements of the specimen corner. Two approaches were investigated for

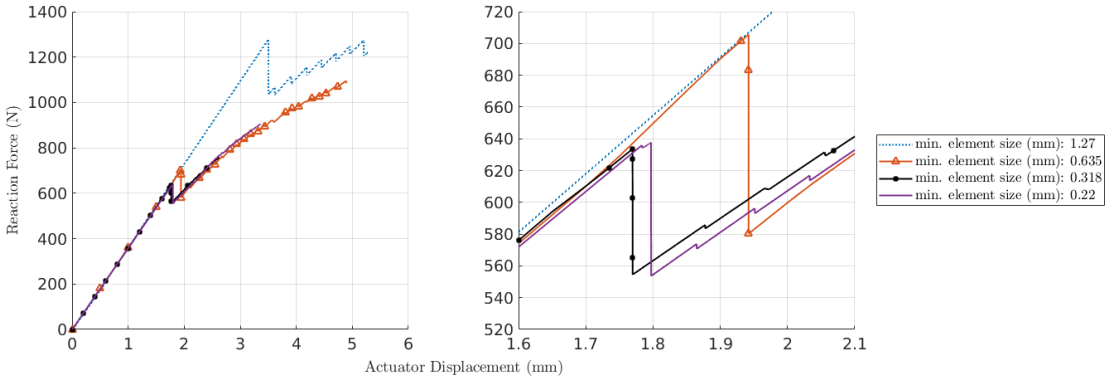

Figure 4.10: Mesh convergence of the ENF model.

modeling the top and bottom roller interactions as shown in Fig. 4.11. Model A is based on a geometric representation of the test fixture. The rollers are modeled using analytical rigid surfaces and contact conditions with the specimen. In Model B, the top roller (which introduces mode II loading) is modeled by equating the vertical displacement of a point on the specimen to the end of the fixture element along the centerline of the top roller. The sliding displacement of the specimen is unconstrained. The bottom roller support is modeled by pinning the specimen at a point corresponding to the centerline of the roller ($x = 2L$ in Fig. 4.11).

The interlaminar mode-mix ratio is evaluated numerically using the Virtual Crack Closure Technique (VCCT). VCCT is a linear elastic fracture mechanics-based approach to obtain the Mode I and Mode II strain energy release rate components required to advance a delamination crack [140]. This method has been used for determining the fracture toughness of composite laminates under various loading conditions [90, 94–96]. Figure 4.12 shows the load-displacement and interlaminar mode-mix results from the two models. Model B produces a nearly constant mode-mix as the delamination propagated between the pre-crack/Teflon end and a small distance ahead of the top roller/load nose while Model A resulted in a changing mode-mix and also a shallower post-peak slope. No difference was found when using a small (=0.01 [78]) and zero Coulomb friction coefficient between the rigid and specimen surfaces. Model B produces the expected behavior of the ASTM standard configuration and matched the results in [95]. Additonally, it was found that the slave-master surface assignment in the interface is also important; the bottom surface of the top arm should be the slave surface in order to agree with the benchmark results in [95]. Interestingly, this sensitivity was not observed in the ENF simulations.

The MMB simulations performed with both models experienced greater force equilibrium convergence difficulties than the DCB and ENF simulations. In addition to the Newton method with automatic time stepping, a line search algorithm was employed in solving the highly nonlinear problem. Following the

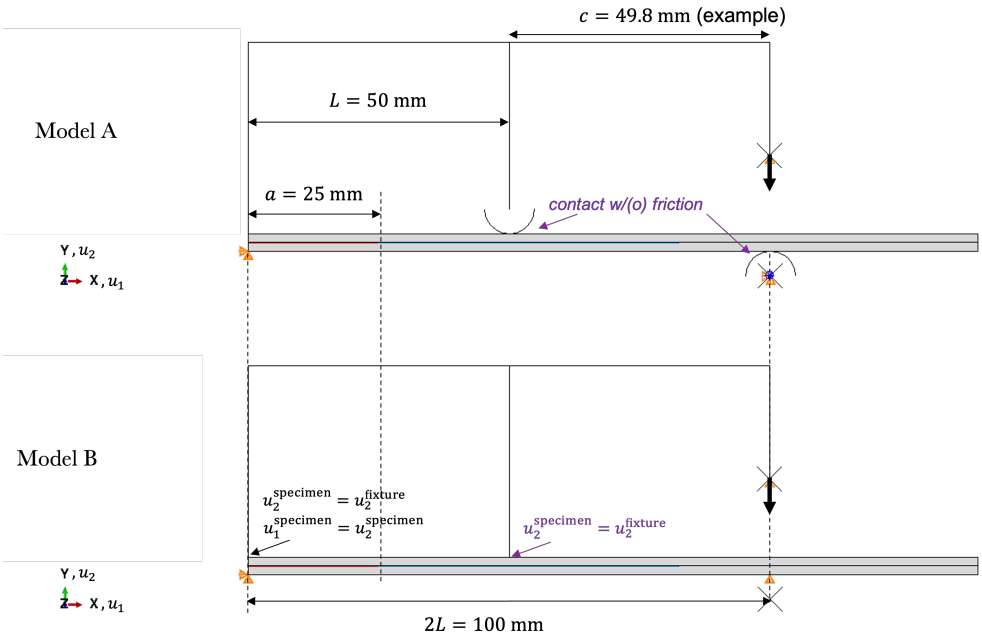

Figure 4.11: MMB model designs.

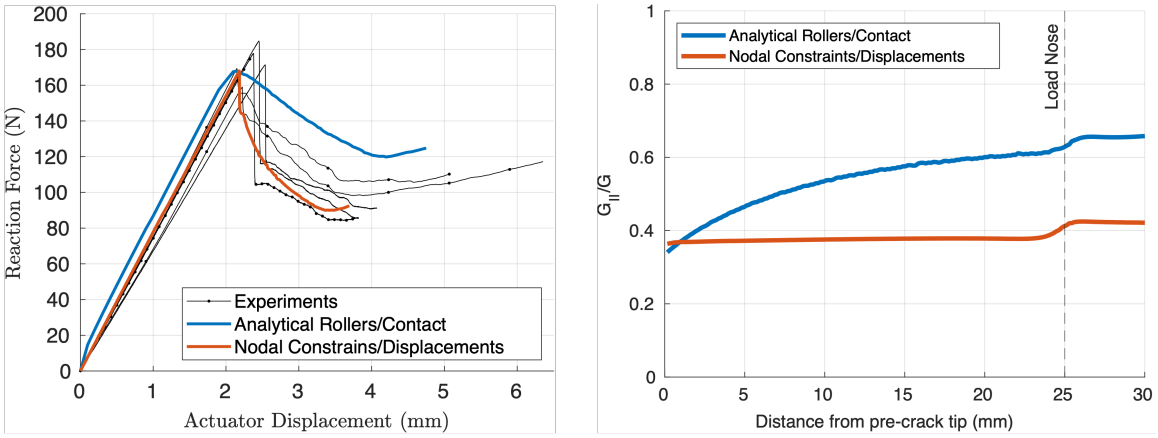

Figure 4.12: (a) Load vs. displacement and (b) interlaminar mode-mix vs. delamination length results for the unpinned MMB $G_{II}/G = 40\%$ configuration models.

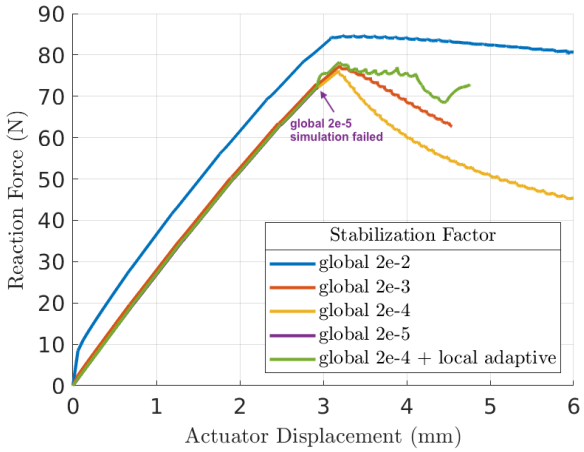

Figure 4.13: MMB load-displacement sensitivity to stabilization parameters.

solution guess using the updated tangent stiffness, the algorithm scales the correction to the displacement by a factor which minimizes the component of the residual vector in the direction of the correction vector. With this approach small increments $\mathcal{O}(10^{-9})$ mm were required to advance the simulation at times, and a solution was obtained using global stabilization. Global stabilization means that the global force equilibrium equations are supplemented with viscous forces, i.e., the external forces, P, and internal forces, I, are therefore considered in equilibrium during an unstable event using the following equation:

$$P - I - cM(\Delta u/\Delta t) = 0 \tag{4.16}$$

where, M is an artificial mass matrix calculated with unity density, c is the stabilization factor, Δu is the vector of nodal displacements, and Δt is the increment of time. The minimum stabilization factor was found by increasing from $2\text{x}10^{-8}$ in 10^{1} increments until the simulation advanced through peak load prediction and significant delamination propagation (the interfacial damage initiation criterion is satisfied at nodes close to the top roller). The stabilization factor value $2\text{x}10^{-4}$ was applied throughout the entire analysis step. Larger values result in over-prediction of the loads during delamination propagation as shin in Fig. 4.13. A simulations was also attempted with local adaptive stabilization and acceptable convergence controls which did not improve on the results as shown in Fig. 4.13.

The SLB model was developed in a similar manner to the MMB, with the geometry and boundary conditions shown in Fig. 4.14. The line search algorithm and stabilization parameters from the MMB simulations were employed. The same mesh as for the MMB model was used and the mode-mix was determined using VCCT. The mode-mix is predicted to be almost constant in the z-pin field prior to the delamination propagating under the load roller then it increases as shown in Fig.4.15.

Figure 4.14: SLB model geometry and boundary conditions.

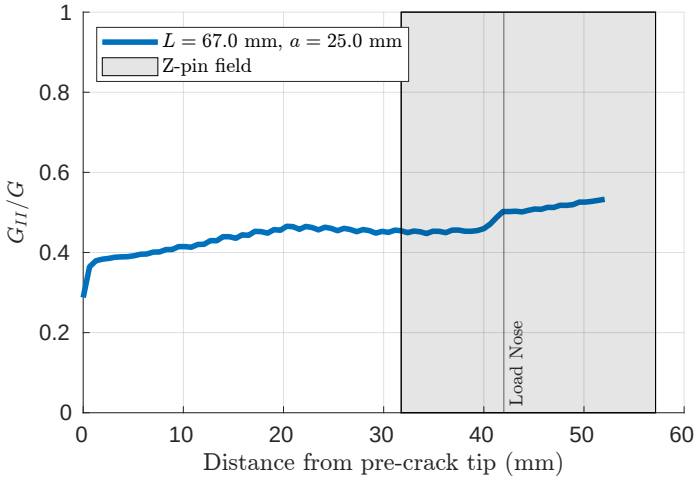

Figure 4.15: VCCT results for the SLB model.

4.2.4 Experimental Results

4.2.4.1 Unpinned Interlaminar Fracture Specimens

The overall behavior of the unpinned experiments is summarized as follows. The DCB tests exhibited somewhat stable crack growth after reaching a peak load which continued and was accompanied by a negative slope in the load-displacement response. The unpinned ENF tests (pre-crack, a=20 mm) and MMB tests exhibited unstable crack growth after reaching a peak load and a short amount of stable crack growth before test termination accompanied by a negative slope in the load-displacement response. The fracture toughness values for the unpinned delamination are calculated according to the procedures in the respective ASTM standards which relate overall compliance and crack growth to the fracture toughness. The fracture toughness calculations are shown in Fig. 4.16 for multiple conditions. The Mode I results include the non-precracked (NPC) toughness values calculated at the initial crack advancement from the pre-inserted Teflon as well as the mean propagation value. The mixed-mode results include the toughness values calculated at the critical load and delamination initiation observed in the MMB experiments as well as the mean propagation value. The Mode II results include toughness values for both of the non-precracked and precracked (PC) conditions. The precracked condition is measured after unload and reload following initial crack advancement. A good fit to the the delamination initiation and NPC condition data as well as the delamination propagation and PC condition data is obtained using with the Benzeggagh-Kenane relationship [18, 39] with exponent value equal to 2.50. The equation relates mode-mix to fracture toughness as follows:

$$G_{\mathrm{C}}^{\mathrm{unp}} = G_{\mathrm{IC}}^{\mathrm{unp}} + (G_{\mathrm{IIC}}^{\mathrm{unp}} - G_{\mathrm{IC}}^{\mathrm{unp}}) B^{\eta_{\mathrm{BK}}^{\mathrm{unp}}} \tag{4.17}$$

Other studies report exponent values between 1.4 and 2.0 for similar CFRPs [39, 109]. The reason for deviation in value calculated from the 20% mode-mix experiments is unclear. The fractured specimens did not show signs of uneven crack growth across the specimen width. The missing delamination propagation data for 60% mode-mix is due to unstable crack growth.

4.2.4.2 Z-pinned Interlaminar Fracture Specimens

The first part of the z-pinned tests proceed like the unpinned experiments where an initial peak load is reached followed by an unstable load drop as the crack advances through the unpinned region. The second part differs in that reloading follows the load drop as the delamination propagates through the z-pinned region. Ultimate failure time varies among the experiments.

The DCB test configuration results in Mode I opening as shown in Fig. 4.17. An in-situ photo of the DCB specimen in Fig. 4.18 shows what appears to be intact z-pin that have pulled out of half of the specimen

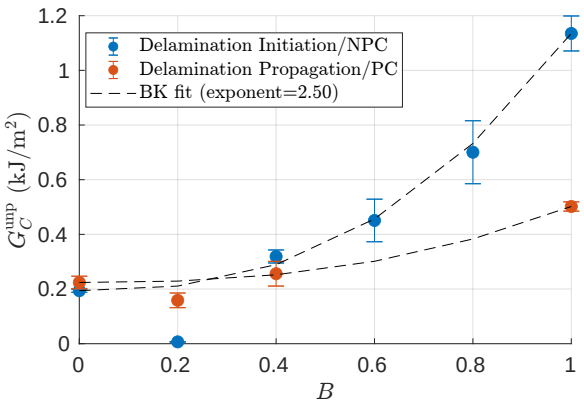

Figure 4.16: Unpinned interlaminar fracture toughness results.

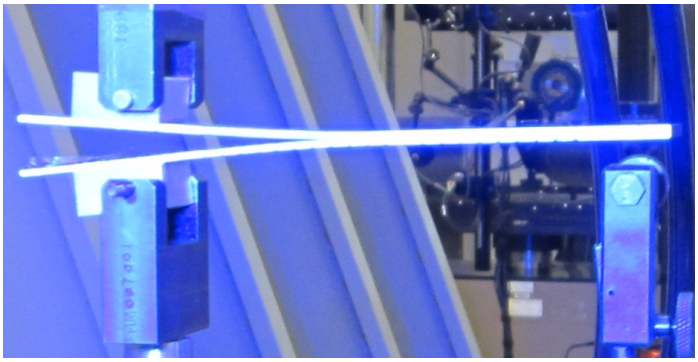

Figure 4.17: Specimen undergoing DCB test.

thickness (one arm). Post-mortem images of the specimens, focused on the region with z-pins are shown in Fig. 4.19 and also indicate that pull-out has occurred. Micrographs in Fig. 4.20 also indicate that the z-pins did not fracture and leave holes once pulled-out. The z-pinned experiment load-displacement curve is shown in Fig. 4.21, including markers at the approximate time when the (matrix) delamination crack is visually observed at each z-pin row. The slope after initial load drop has a positive sign and arrests the delamination growth until there is a large actuator displacement, while the unpinned experiment curves require much less displacement. This is in line with other experimental findings in the literature [125, 134]. The peak load is reached when there are still 3 z-pin rows not visible past the delamination crack (around 34 mm actuator displacement). Final failure of the specimen occurs when the delamination unstably propagates to the end, as indicated by the sudden loss of load in Fig. 4.21 around 55 mm actuator displacement. The force-displacement curve also include an unload-reload prior to delamination propagation according the standard test procedure.

An example of a loaded specimen during an ENF test is shown in Fig. 4.22. The ENF interface undergoes dominant sliding as shown in Fig. 4.23, where the separated sides of the laser engraved scale marks

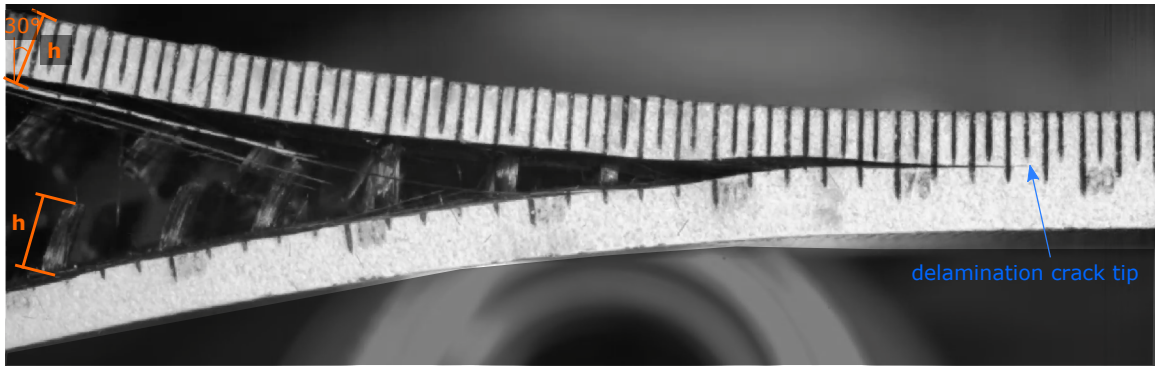

Figure 4.18: DCB image at failure (beginning of last load drop).

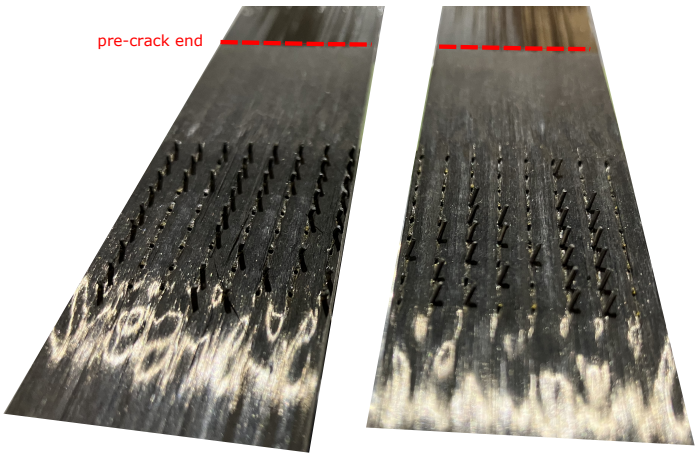

Figure 4.19: Post-mortem state of DCB specimen.

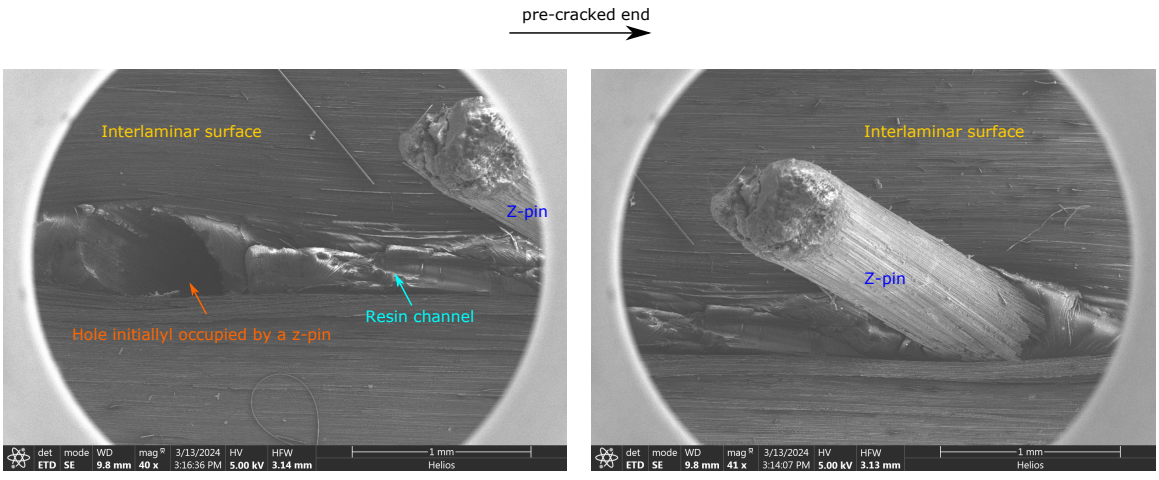

Figure 4.20: SEM images of z-pins and pull-out holes in the DCB specimen.

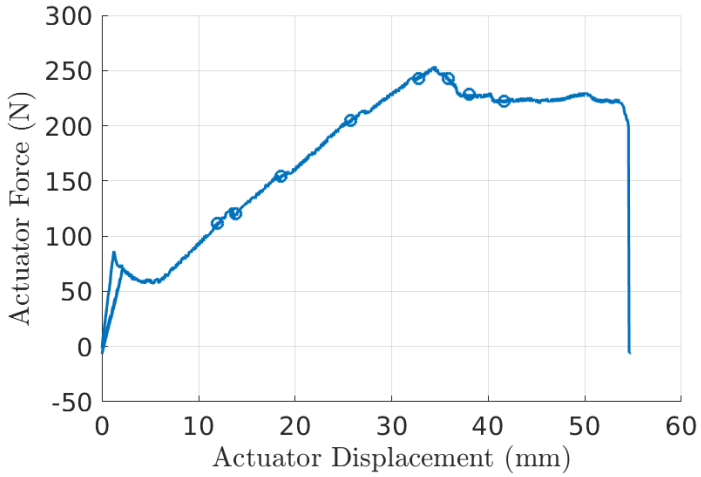

Figure 4.21: Load-displacement and delamination propagation (markers indicate delamination crack observed passing by a z-pin row) of the z-pinned DCB test.

have displaced relative to each other. There is not significant detectable normal opening separation between the upper and lower specimen arms. Since the ENF test did not result in completely fractured specimens, obtaining more detailed images to evaluate the state of the z-pins were not possible. Shearing of z-pins could have occurred because of sliding of up to 0.3 mm or greater as marked in Fig. 4.23, which is a large fraction of the z-pin diameter and would match failure mode observations in [127, 128]. The z-pinned experiment load-displacement curves are shown in Fig. 4.24, including markers at the approximate time when the delamination crack is visually observed at each z-pin row. The slope after initial load drop has a positive sign and arrests the delamination growth until the actuator displacement about doubles the displacement at delamination initiation in the unpinned region. The unpinned experiment curves require much less displacement for the delamination to reach the center roller. This is in line with other experimental results in the literature [125].

MMB experiments were successful with high fraction of Mode I/Mode II loading ($B = 0.148$ with $c = 35.0$mm and $B = 0.279$ with $c = 25.0$mm), with an example of a loaded specimen in Fig. 4.25. Figure 4.26 includes images obtained from the video footage which provide visual evidence of the mode-mix calculated. Yellow lines were added to help show the sliding displacement of originally aligned marks across the specimen delamination path. Figure 4.26a was expected to show less sliding than Figure 4.26b, and this appears to be the case. The z-pinned experiment load-displacement curves are shown in Fig. 4.27, including markers at the approximate time when the delamination crack is visually observed at each z-pin row (half of the curves are marked at the minimum load following the delamination onset at initial peak load. The positive (reload) slope in the load-displacement curve of Fig. 4.27 after the initial load drop is also observed in [109], where a large increase in displacement required for the delamination to pass through a z-pin field of

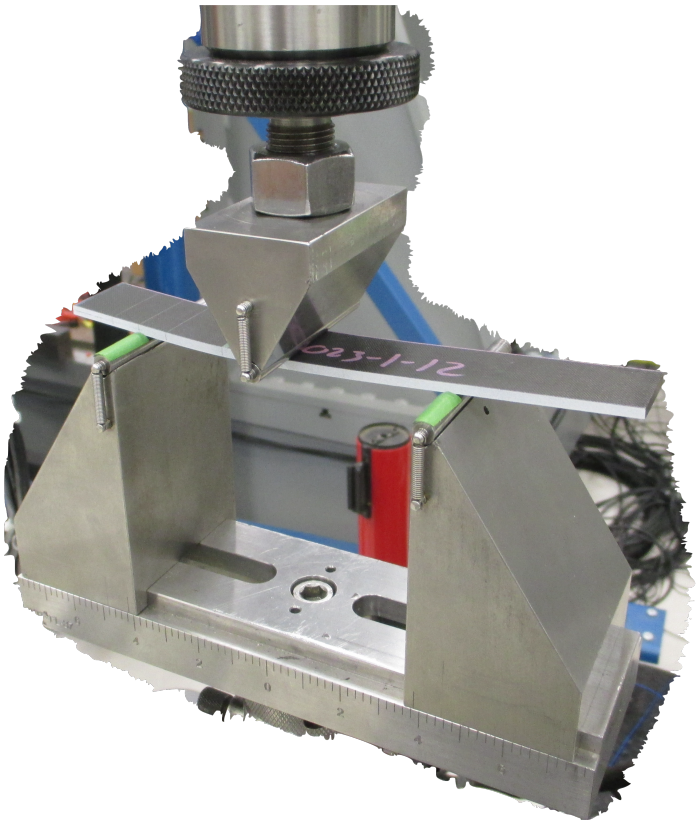

Figure 4.22: Specimen undergoing ENF test.

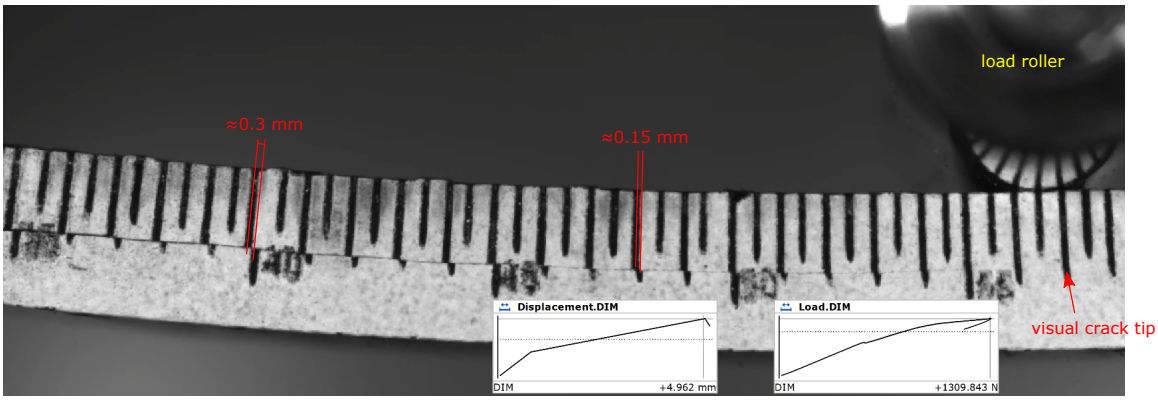

Figure 4.23: ENF image when delamination has reached the top roller.

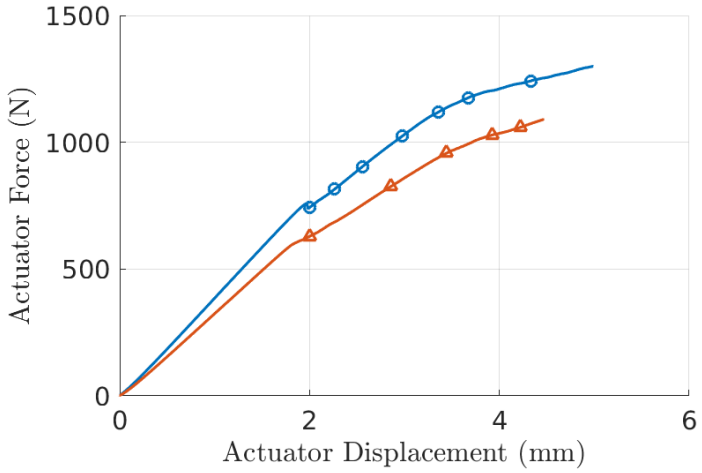

Figure 4.24: Load-displacement and delamination propagation of the z-pinned ENF tests.

23 mm length under $B = 0.25$ and $B = 0.47$ conditions. The tests conducted with higher fraction mode-mix (around $B = 0.50$ with $c = 20.0$mm and $B = 0.67$ with $c = 17.5$mm) initially exhibited failure of the bond between the hinge tabs and specimen prior to crack propagation. Since the hinges disbonded completely leaving no adhesive on composite specimen, a more aggressive surface preparation was performed and the tests repeated. With this preparation procedure the tests ran successfully. Crack propagation was stable in the $c = 35.0$ mm and $c = 25.0$ mm tests following an initial unstable crack growth into the z-pin field in half of the experiments. Crack propagation was completely unstable in the $c = 20.0$ mm and $c = 17.5$ mm tests. In the $c = 17.5$ mm test, the crack immediately propagates to the top roller after an approximate 61% load drop and very short reload. Since the MMB tests did not result in completely fractured specimens I was unable to obtain more detailed images to evaluate the state of the z-pins. It is hypothesized that the z-pins are in a loading condition similar to the DCB tests, however some bending could be present because of the relative sliding and opening present in Fig. 4.26. An additional observation is that the mixed-mode tests all showed some difference in the overall response and crack propagation behavior. This is thought to be caused by crack migration off of the midplane in the case of experiment 2 for both $B = 0.148$ and $B = 0.279$, and experiment 1 for $B = 0.453$.

The Single Leg Bend (SLB) tests exhibited stable crack propagation through the z-pin field prior to specimen arm fracture. Figure 4.28 shows a specimen prior to failure and during delamination propagation. The end of the tests were the result of the upper specimen arm fractures due to bending leaving a ledge like shown in Fig. 4.29a-b. Figure 4.29c shows a micrograph of the fracture region in one specimen which coincides with the first row of z-pins. The z-pins are mostly intact, however along the fracture "ledge", the higher magnification images show fiber cracking indicative of localized bending. The z-pinned experiment load-displacement

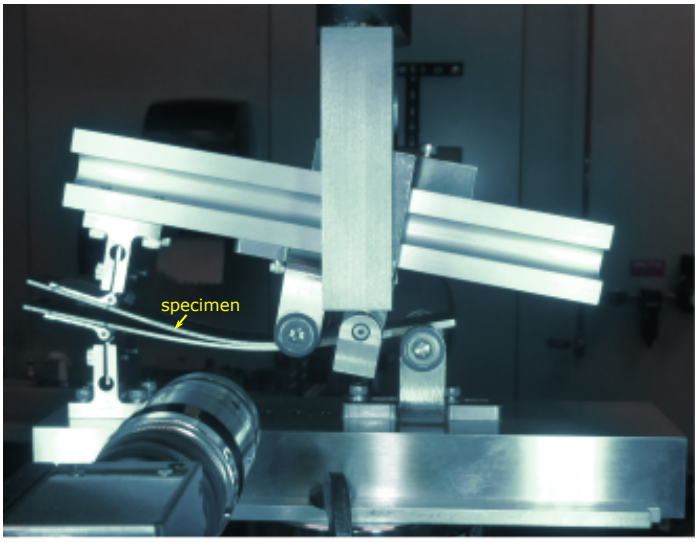

Figure 4.25: Specimen undergoing MMB test.

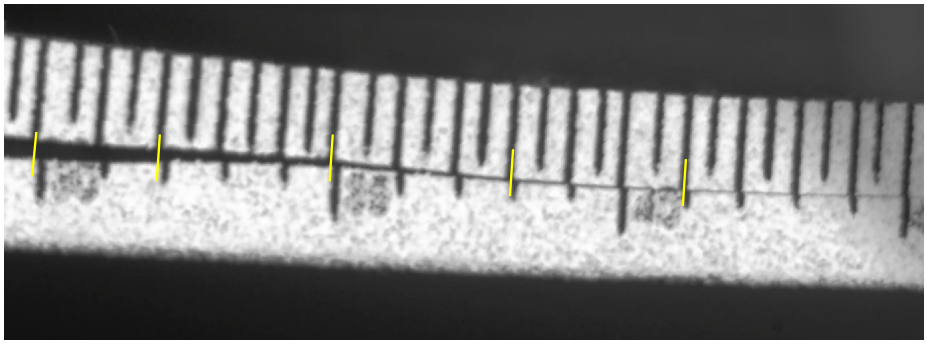

(a)

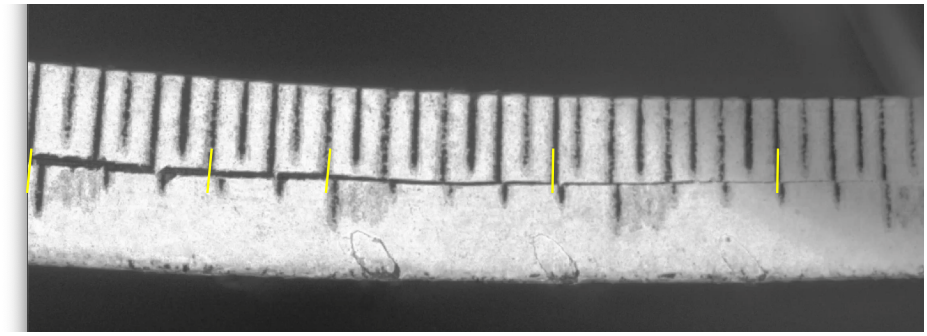

(b)

Figure 4.26: Images of z-pinned MMB tests when delamination has reached the top roller. Top: $B = 0.148$ and bottom: $B = 0.279$

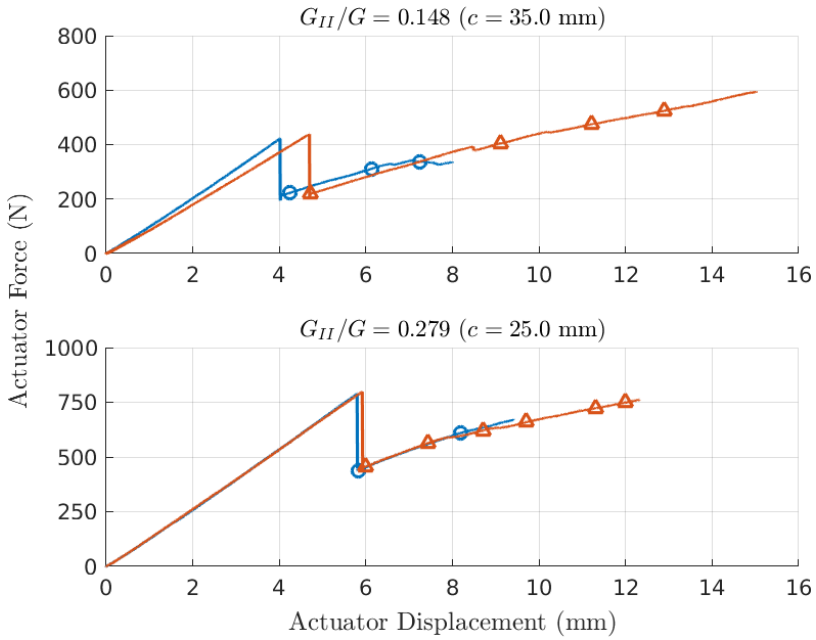

Figure 4.27: Load-displacement and delamination propagation of the z-pinned MMB tests.

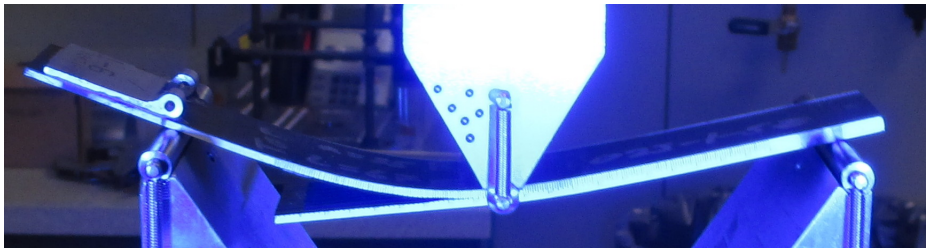

Figure 4.28: Images of SLB ($B = 0.453$) specimens during delamination propagation.

curves are shown in Fig. 4.30, including markers at the approximate time when the delamination crack is visually observed at each z-pin row. There is considerable difference in delamination progression with respect to applied load-displacement in the SLB experiments. The delamination propagates through 7 rows prior to specimen failure in one case and only 5 rows in the other. Z-pinned tests on SLB specimens have not been reported in the literature and there are no other results for comparison.

4.2.4.3 Z-pinned Unidirectional Compression Specimens

The stress-strain curves for UD z-pinned specimens are shown in Fig. 4.31. The mean chord modulus calculated at 1000-3000 μstrain is 131.5 GPa (Standard Deviation (SD): 1.6 GPa). The mean compressive strength calculated as the maximum load divided by the mean gage cross-sectional area is 922.2 MPa (SD: 75 MPa). 5 of the specimen strengths are within 5.3% while the sixth is 20% higher. The failure pattern of all of the specimens are acceptable per the definitions for unpinned laminates in [10]: Sec. 12. The modulus and strength

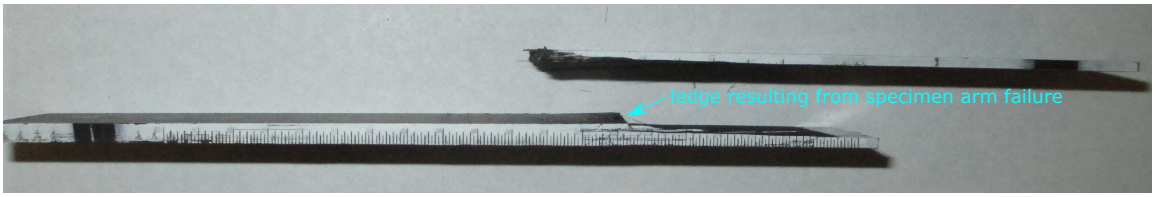

(a)

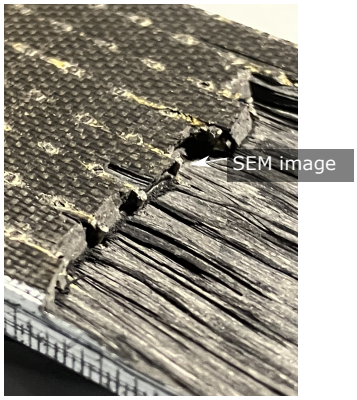

(b)

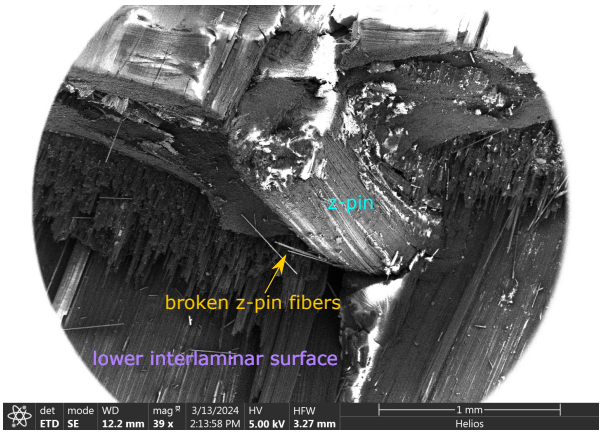

(c)

Figure 4.29: Post-mortem images an SLB specimen.

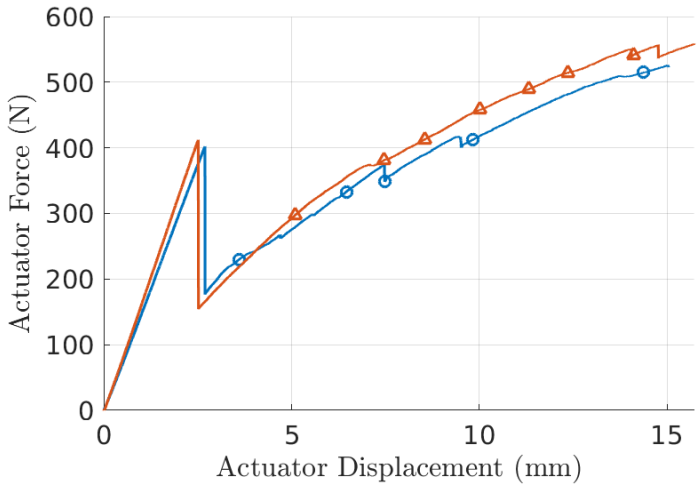

Figure 4.30: Load-displacement and delamination propagation of the z-pinned SLB tests.

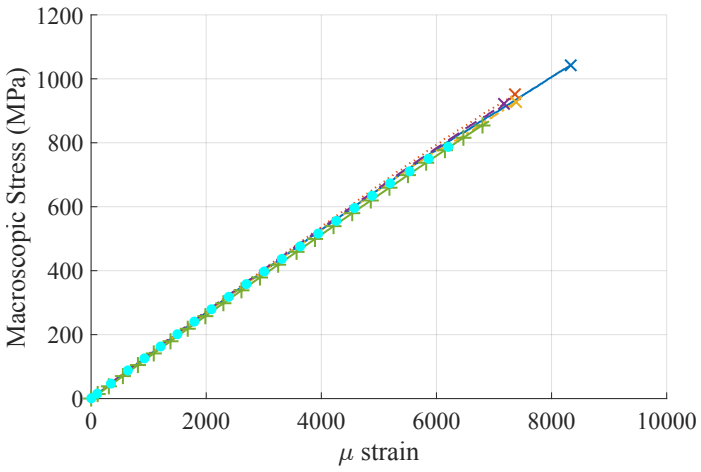

Figure 4.31: Stress-strain results from CLC tests on z-pinned UD specimens.

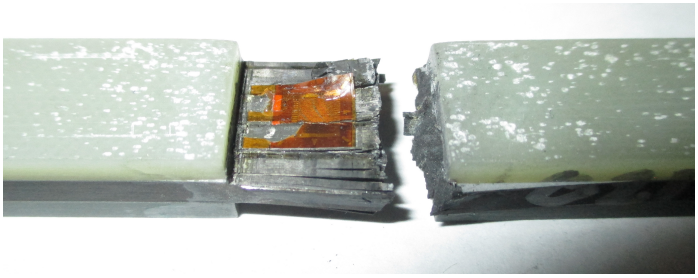

Figure 4.32: Example of post-mortem images from z-pinned UD CLC test specimens.

are both lower than previously reported values for IM7/977-3 in [46]. Other researchers have conducted experiments to investigate the difference in properties for laminates with and without z-pins and concluded that the z-pins have an effect of up to about a 10% reduction on the longitudinal properties, mainly due to the increased fiber waviness due to the presence of the z-pins [112, 151]. Implications of the z-pinning process on the lamina structure is also evident in micrographs of the ILF specimens. Figure 4.33 shows the influence of z-pins on the in-plane fiber waviness. Z-pin insertion pushes out fibers and results in tapered resin pockets as also observed in [112]. With the current z-pin configuration, the resin pockets form a channel except for at the ends of the z-pin field.

4.2.5 Calibration Simulation Results and Discussion

Calibration of $\hat{t}^I$ and $\hat{\delta}^f$ require $\hat{\delta}^0_{\mathrm{I}}$ and $\hat{\delta}^0_{\mathrm{II}}$ to already be determined. Therefore, calibration is undertaken by first performing parametric studies to obtain values for $\hat{\delta}^0$ under pure Mode I and Mode II conditions. The rest of the calibration procedure requires performing parametric studies on pairs of $\hat{t}^I$ and $\hat{\delta}^f$ in order to match the experimental results. The metrics for accepting calibration include quantitative evaluation of the best match between the simulation and experimental overall load-displacement curves for each test configuration as well

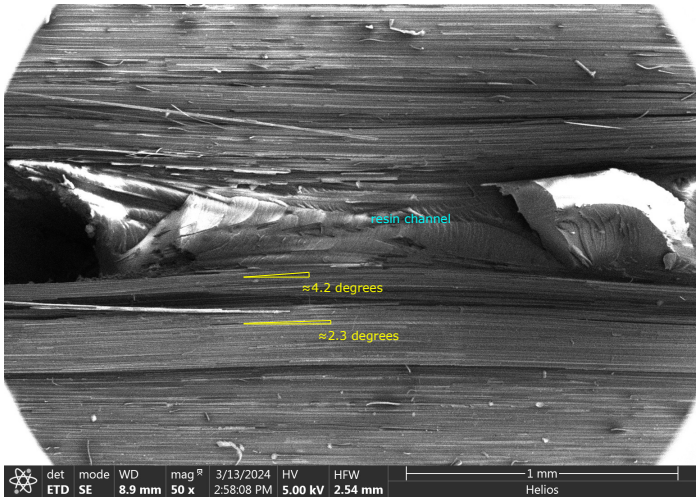

Figure 4.33: Example SEM image of fiber waviness channel.

Table 4.3: Experimental and simulation results used for calibrating $\hat{\delta}^0$.

	P^0_{DCB} (N)		P^0_{ENF} (N)	
	Mean (SD)	Target	Mean (SD)	Target
Experiment	75.3 (7.9)	86.3	629.5 (58.1)	595.3
Simulation		92.6		597.6

as the delamination growth rate sampled at key points in the test results. Calibrated property values are also compared to physical meaning and other values used in the modeling literature. The target values from the experiments are chosen from the valid z-pinned experiment results. The experimental (including results from unpinned specimens) and predicted values resulting from calibration for pure Mode I and Mode II conditions are listed in Table 4.4.

4.2.5.1 Mode I Properties

The z-pinned DCB test result was used to calibrate the Mode I separation at onset of delamination by matching the predicted initial peak load in the simulation to the experimental value. The value for $\hat{\delta}^0_{0.0} = \delta^0_{\mathrm{I}} = 9.0e-7$ mm resulted in an initial peak load predicted within 1% of the target value. The resulting matrix/unpinned interface strength is 9.0 MPa. Other researchers have chosen the mode I interlaminar strength value based on the transverse tensile strength and shear strengths (around 44-72 MPa [15, 114]) but a smaller value is commonly found necessary to match DCB experiments (e.g. 15.0 MPa [134] or 2.0 MPa [70]). In my simulations, using $\hat{\delta}^0_{0.0} = 36$ MPa$/k = 3.6e-6$ mm (4x the best fit value) over predicts the experimental initial peak load by about 4%. Using the transverse tensile strength for this material system as reported in [46] ($\hat{\delta}^0_{0.0} = 78.9$ MPa$/k = 7.89e-6$ mm) over predicts the experimental target load by 36%. The final value accepted in calibration is $\hat{\delta}^0_{0.0} = 4.32e-6$ mm, which is based on the average flatwise tension strength

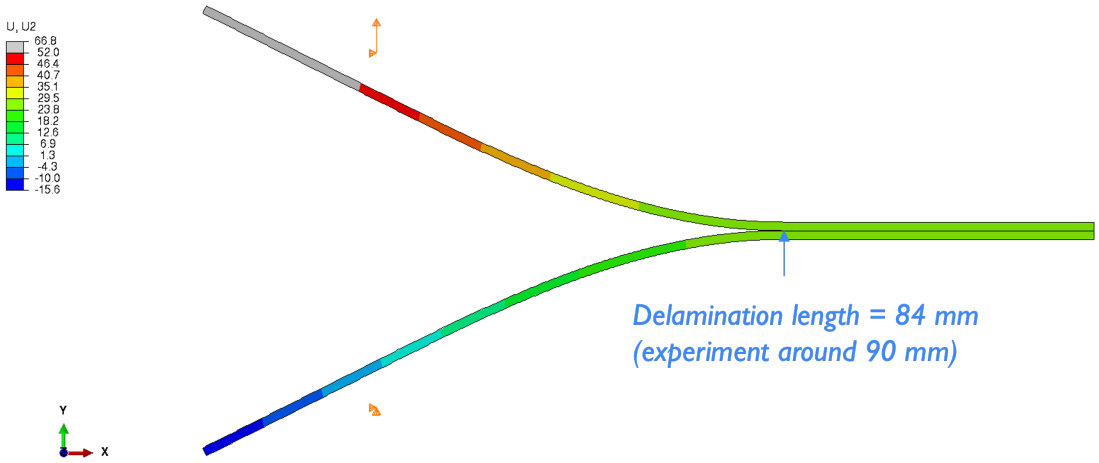

Figure 4.34: DCB simulation prediction at failure.

measured in an interlaboratory study reported in [13] for IM7/977-3 laminates. The simulation using this value over predicts the experiment initial peak load by 7.4% (92.6 N).

The overall load-displacement curve using the calibrated Mode I interface properties is shown in Fig. 4.35 alongside the experimental curve ($B = 0$). Under pure Mode I conditions, the traction at z-pin failure onset is expected to be determined only by shear strength along the z-pin - lamina interface which is related to the length of the z-pin resisting pull-out. The calibration resulted in $\hat{t}^I = 43.2$ MPa, which is equal to the matrix debonding strength calculated as $k\hat{\delta}^0_{0.0}$. This value is larger than the debond strength calculated from the FWT experimental results in [134] of 30 MPa for T650/BMI z-pins co-cured in 24-ply IM7/977-3 laminates (the same material and thickness as in the current study). The difference could be attributed to the epoxy matrix material in the current z-pins which coheres better to the 977-3 lamina matrix material. Setting $\hat{\delta}^f_{0.0} = h$, which matched the physical opening distance observed in experiments resulted in the best fit to the experimental curve. Intuitively, fixing $\hat{\delta}^f$ while increasing $\hat{t}^I$ results in a larger area under the TSL (the total apparent fracture energy) and this increases the load-displacement slope and displacement at failure in the virtual tests. The maximum load/inflection point is also increased. In the experiment, the maximum load is reached prior to the delamination propagating through the entire z-pinned region suggesting a "critical" number of z-pins engaged. The simulation predicts the tip of the matrix delamination length of around 79 mm at the peak load at a displacement of 37 mm and the crack in the experiment is at a location close to 75 mm. The typical opening behavior is shown in Fig.4.34.

Table 4.4: Experimental and simulation results used for calibrating $\hat{\delta}^0$.

	P^0_{DCB} (N)		P^0_{ENF} (N)	
	Mean (SD)	Target	Mean (SD)	Target
Experiment	75.3 (7.9)	86.3	629.5 (58.1)	595.3
Simulation		92.6		597.6

4.2.5.2 Mode II Properties

Two z-pinned test results were available for calibrating the mode II separation at onset of delamination. In the experiments, delamination onset is accompanied by a change in sign of the load-displacement slope. In the case of experiment 2, there is a clear initial peak load followed by a load drop over a very brief change in displacement because of unstable crack growth, however experiment 1 exhibits a less severe change in the load-displacement curve. The knee point of experiment 1 was determined by the so-called "Kneedle" algorithm (smoothing the raw experiment data around the overall change in slope and finding the largest distance to a chord taken between two points [142]). As shown in the mesh convergence results, the FE model predicts a sharp change in the sign of the load-displacement slope. Initially, the model matrix strength parameter, δ^0_{II}, is adjusted in order that the initial predicted peak load matches the mean of the knee point in the experiment 1 curve (595.3 N) and the initial peak load in the experiment 2 curve (757.1 N). The conjugate interface strength value calculated as $t^0_{\mathrm{II}} = k\delta^0_{\mathrm{II}} = 280.0$MPa is much higher than the values reported in literature for similar material systems [15, 26, 106]. For this reason the calibration is finally performed by matching the predicted initial peak load to the load at the knee point in experiment 1. The calibrated value which results in a prediction within 1% of the target value is $\hat{\delta}^0_{1.0} = \delta^0_{\mathrm{II}} = 9.02e-6$ mm.

The simulation load-displacement curve is terminated when the delamination has propagated to the load roller as shown in Fig.4.36. The ENF result is shown in Fig. 4.35 for the simulation with the minimum element length determined from the mesh convergence study for strength (0.22 mm). Failure onset under pure Mode II conditions was expected to be associated with shear resistance of the z-pins as well as the resistance of the laminate to ploughing. Setting $\hat{t}^I_{1.0} = 90.2$ MPa resulted in a good match to both the delamination position as a function of load and the load-displacement curve during reload. Separation at failure under pure Mode II conditions was expected to be determined by the shear strain at failure of the z-pin and the extent of laminate ploughed. In this case, the value for $\hat{\delta}^f_{1.0}$ would be smaller than $\hat{\delta}^f_{0.0}$. The physical separation observed in the experiments consisted of dominant sliding of approximately 0.4 mm and little or no normal separation. The calibration procedure resulted in $\hat{\delta}^f_{1.0} = 0.41$mm. The final load predicted with the accepted calibration is within 3% of the mean of the maximum loads recorded in the experiments (also terminated when the delamination has propagated to the load roller). During calibration, both of the parameters $\hat{\delta}^f_{0.0}$ and

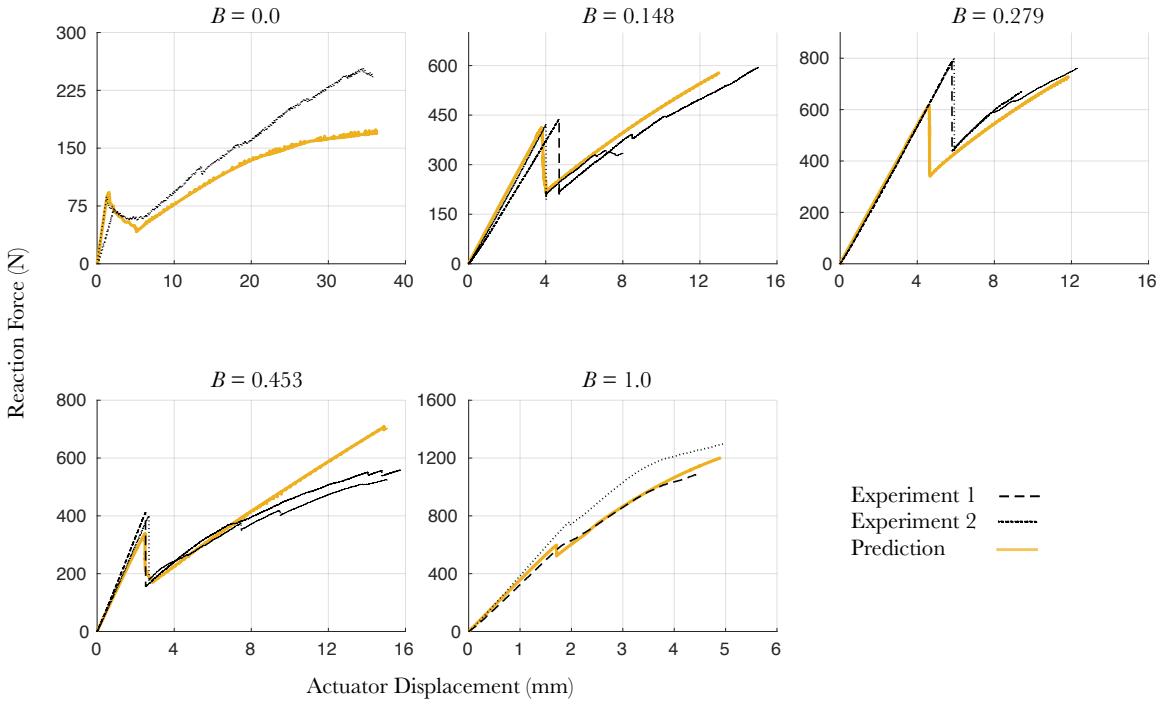

Figure 4.35: Load-displacement curves from valid experiments and calibrated simulations.

$\hat{t}^I_{1.0}$ influenced the reloading slope, suggesting that other combinations could give a very similar behavior. This a potential topic for additional consideration.

4.2.5.3 Mixed-Mode Properties

Simulations with mixed-mode conditions were performed to verify the pure Mode I and Mode II calibration using the unpinned MMB test results. The predicted load-displacement curves using the calibrated values for $\hat{\delta}^0_{\mathrm{I}}$ and $\hat{\delta}^0_{\mathrm{II}}$ are shown in Fig. 4.37 alongside the experimental results. Table 4.5 shows the mean and standard deviation of the initial peak loads in the unpinned MMB experiments compared to the predicted values to help verify the model calibration. The predicted initial peak load for the $B = 0.40$ and $B = 0.60$ are within 10% of the mean experimental values. The initial peak load for the $B = 0.20$ is overpredicted by about 29%, and the initial peak load for $B = 0.80$ is underpredicted by about 18%. These outcomes suggest that better agreement could be achieved by decreasing the value for $B = 0.0$, however another possible cause for the discrepancy for the $B = 0.20$ results could be related to the low fracture toughness value calculated in the experiments. The calibrated value for $B = 1.0$ could too small in accordance to the discussion in Section **??**. The full results from simulations for $B = 0.20,\ 0.40,\ 0.60$ were not available due to slow convergence, however, the predictions agree with the experiments. The magnitude of the load drop and slopes of the curve afterward

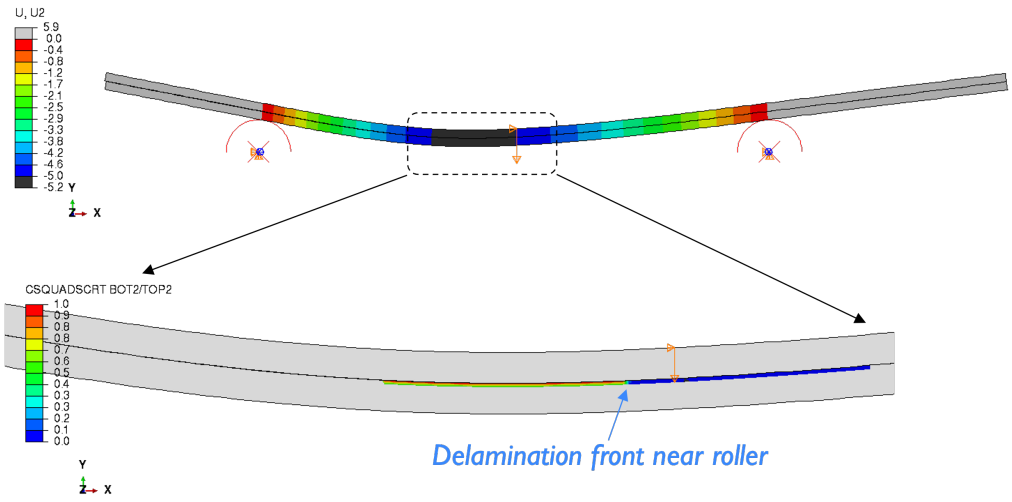

Figure 4.36: ENF simulation prediction at failure.

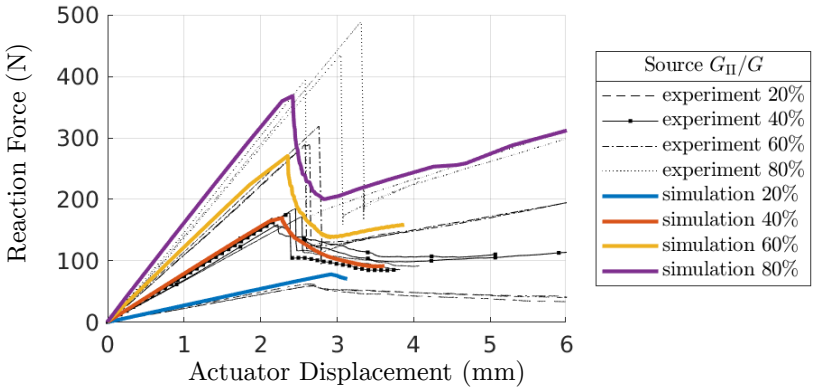

Figure 4.37: Experimental and simulation load-displacement curves for the unpinned MMB specimens.

agree with the experiments and verify the fracture toughness fit reported in Section 4.2.4.1.

For calibration of the softening and failure parameters, two simulations were considered: MMB and SLB configurations for $B = 0.148, 0.279, 0.453$. The calibrated results for these configurations are shown in Fig. 4.35. The calibration was accepted when predicted the load-displacement curves after the initial load drop (reload) and the delamination propagation agreed with experimental observations. Quantitative agreement in the load-displacement data was determined by comparing the equivalent load in the simulation curve to the experiment curve at every recorded displacement. The equivalent load was taken at the closest displacement point in the simulation curve. Comparing the data this way is chosen since the simulations were performed with automatic time stepping and the displacements in the simulation are not guaranteed to be the same as in the experiments. The total error measured by sum of squares of the difference between the equivalent and experimental loads is used to select the best match. Statistics of the relative error (calculated

Table 4.5: Experimental and simulation results for the initial peak of the unpinned MMB specimens.

B	Experiment Mean (SD)	Prediction
0.20	60.4 (1.5)	77.8
0.40	172.5 (9.6)	169.9
0.60	299.1 (17.0)	271.0
0.80	450.5 (34.0)	368.4

Table 4.6: Relative error statistics from the load-displacement curve calibration.

B	Absolute maximum	Mean	SD
0.148	0.0622	-0.0056	0.0213
0.279	0.0879	-0.0650	0.0149
0.453	0.3037	0.1497	0.0791

as $|(P_{exp} - P_{sim})/P_{exp})$ from the calibration results are reported in Table 4.6 (the mean of the relative error from both experiment curves is shown). The location of the matrix delamination front is defined as the where $\hat{\delta} > \hat{\delta}^I$. Discussion on the calibration results and corresponding errors for each mode-mix configuration are provided next.

Under mixed-mode conditions, the traction value at z-pin failure onset is expected to result from shear and bending stresses of the z-pins in addition to the z-pin - lamina interface strength. The separation at failure is a consequence of z-pin pull-out or z-pin fracture due to bending. At lower mode-mixes especially, failure by pull-out may occur prior to z-pin fracture based on other DCB and single-pin experimental observations where the local mode-mix is close to pure Mode I [54, 179]. The predicted overall behavior from calibration is slightly more nonlinear than the experiment curve which continues to a displacement about about 14 mm. The predicted peak load of the calibrated overall response for the $B = 0.148$ configuration matches well with the experiments. Maximum relative error of the predicted load-displacement curve is around 6%. The relatively large standard deviation of the error can come from the less smooth experimental curve which exhibits dips that are not present in the simulation curve. These dips are associated with the halt-propagate behavior of the crack advancement in the experiments. The location of the matrix delamination front is compared to visual observation of the crack front in the experimental results at 7.0 mm actuator displacement. This evaluation results in the calibrated parameters $\hat{\delta}^f = 0.82$mm, and $\hat{t}^I = 45.9$MPa. While I was not able to examine the test specimen fracture plane it is expected that the z-pin behavior is pull-out dominated. Other model parameter sets with smaller $\hat{t}^I$ resulted in a peak load and softening behavior that appeared more like the experiments but were rejected because the peak load occurred much too early. The accepted parameters resulted in a crack front near the end of the specimen at 2% of the experimental displacement at failure.

For $B = 0.279$, the predicted initial peak load (which is controlled by the matrix damage onset parameter)

Table 4.7: Lamina properties.

E_{11} (GPa)	E_{22} (GPa)	G_{12} (GPa)	G_{23} (GPa)	ν_{12}
144.0	8.7	5.0	3.9	0.32

is under predicted. The calibrated parameters $\hat{\delta}^f = 1.63$mm and $\hat{t}^I = 48.8$MPa result in a reloading curve which matches the nonlinearity of the experiments and visually observed crack advancement well. The overall load is underpredicted on average by about 6.5% and deviating up to 8.8%. In the single-pin pullout tests performed in Ref. [179], they find that for low mode-mixes ($B \leq 0.250$) that the z-pins fail strictly by pull-out, at a total displacement approximately equal to the z-pin half-length. The z-pins in the current study have a larger cross-section and therefore a larger bending resistance so the z-pin could resist the mode-mix conditions by pulling out and the calibrated value for $\hat{\delta}^f$ makes physical sense. Smaller values of $\hat{t}^I$ result in less stiff reloads while smaller values of $\hat{\delta}^f$ result in greater nonlinearity which deviates from the experimental slope.

For $B = 0.453$, the calibrated parameters are $\hat{\delta}^f = 0.82$mm, and $\hat{t}^I = 53.5$MPa. With these parameters, there is a good match to the initial reload slope, however the load-displacement response does not show the same degree of nonlinearity as the latter part of the experimental curves. Decreasing $\hat{\delta}^f$ and $\hat{t}^I$ both have a significant effect on the reloading stiffness (decreasing it) and very low values of $\hat{t}^I$ (e.g., 7 MPa) result in more significant nonlinearity similar to the experiments. These parameters are rejected for calibration because the crack advance is much quicker. The delamination propagates to the same point as observed in the experiments at approximately half the experimental displacement. The critical separation is indicative of the failure mechanism observed in the SEM images (Fig. 4.29). There appears to be bending, however the in situ test images show significant interface normal separation as the delamination advances. A larger length of the z-pins in this test/mode-mixity must resist shearing due to significant crack opening so there is a combination of pull-out and shearing forces on the z-pin.

The composite lamina properties are listed in Table 4.7, where 1 is the composite longitudinal direction. The values for E_{22}, G_{12}, and ν_{12} were chosen based on Ref. [46] while E_{11} was calibrated so that the initial slope in the DCB and ENF simulations fits the experiment. The slope in the experiments measured at 10-30% of the initial peak displacement was equal to 10% of the DCB experimental slope and 6% of the mean of the ENF experimental slopes. The elastic properties are considered the same in the 1-2 and 1-3 directions. These values were subsequently used for the mixed-mode configuration simulations as well. The parameter values for the trilinear TSL are in Table 4.8. The mixed-mode values for $\hat{\delta}^0$ are calculated using Eqn. 4.13. The separation at the change in softening slope, $\hat{\delta}^I$, is calculated with Eqn. 4.15 using $G_{\mathrm{IC}}^{(\mathrm{unp})} = G_C^{(\mathrm{unp})}(0.0)$, $G_{\mathrm{IIC}}^{(\mathrm{unp})} = G_C^{(\mathrm{unp})}(1.0)$, and $\eta_{\mathrm{BK}}^{\mathrm{unp}} = 2.50$ based on the unpinned delamination propagation/NPC data discussed

Table 4.8: Analytical and calibrated TSL parameters ($k = 10^7$ N/mm^3)

B	0.0	0.148	0.279	0.453	1.0
$\hat{\delta}^0$ (mm)	4.32e-6	4.59e-6	4.88e-6	5.36e-6	9.02e-6
$\hat{\delta}^I$ (mm)	0.0104	0.00986	0.00966	0.00980	0.0111
$\hat{t}^I$ (MPa)	43.2	45.9	48.7	53.5	90.2
$\hat{\delta}^f$ (mm)	1.63	0.82	1.63	0.82	0.41

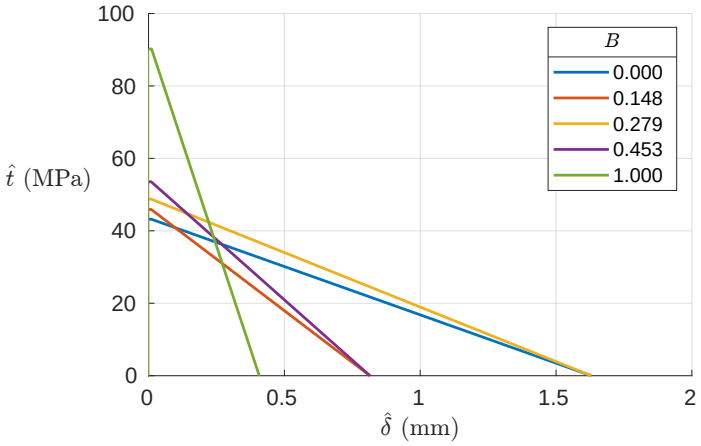

Figure 4.38: Calibrated TSLs.

in Section 4.2.4.1. The calibrated TSLs are shown in Fig. 4.38.

4.3 Conclusions

This chapter presented a trilinear cohesive zone model for predicting delamination in the presence of z-pins. The constitutive law represents the averaged response associated with matrix debonding and z-pin failure mechanisms. This averaged approach is advantageous over discrete z-pinned interface models because in the case of finite element models, the z-pinned interface does not require special meshing related to the z-pinning configuration, rather only the area of the z-pinned region must be considered. Experimental results from specimens in DCB, ENF, MMB, and SLB configurations were analyzed and provide information on the macroscopic response of z-pinned composites under pure Mode I, Mode II, and mixed-mode conditions. The experimental load-displacement responses and crack propagation observations were used to calibrate the trilinear cohesive zone model for 5 mode-mixities. The calibration procedure presented in this chapter contributes a novel approach to directly connects macroscopic interface behavior in the presence of z-pins to the CZM constitutive law properties under pure Mode I, pure Mode II, and mixed-mode conditions.

It was expected that the TSL would change shape across mode-mixes, potentially similar to those depicted in Fig. 4.1 due to the z-pin failure mechanisms experienced under different mode-mix conditions. The calibration resulted in a consistent TSL shape across mode-mixes, where the intermediate traction is equal to

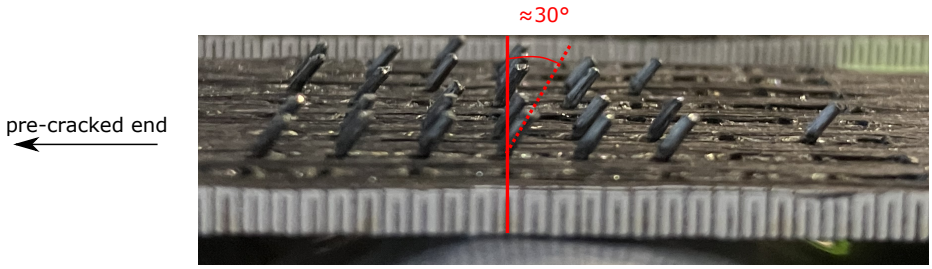

Figure 4.39: Post-mortem photograph of z-pins in DCB specimen.

the traction at onset of softening (i.e., there is not a softening of the traction between $\hat{\delta}^0$ and $\hat{\delta}^I$). Neglecting $B = 0.148$, the calibrated TSLs exhibit a trend of decreasing $\hat{\delta}^f$ similar to other studies and correspond to a transition from pull-out dominated failure to bending and shear failure between $B = 0.279$ and $B = 0.453$.

One potential explanation for the consistent shape resulting from the current calibration procedure could be the inclination of the z-pins in the experimental specimens. As mentioned in Section 4.2.4.2, the z-pins were consisted in a uniform manner at an inclination around 30 degrees from the through-thickness direction. This inclination is evident in post-mortem examination of a DCB specimen in Fig. 4.39, where the horizontal distance between the z-pin ends is approximately equal to the distance measured on the exterior surfaces of the specimens prior to testing. The z-pins were inclined away from the pre-cracked end (as is also shown in the in-situ image in Fig. 4.18), meaning that while the test fixture ensured Mode I loading, the ply separation process was resisted more than expected with orthogonal pullout. Post-mortem examination of specimens with SEM show that there is additional damage present in the z-pins following the DCB tests. Figure 4.40 shows broken fibers near and away from the interlaminar surface. The broken fibers away from the interlaminar surface are evidence of local tensile failure and indicate that the z-pins were subject to bending. The broken fibers near interlaminar surface includes additional failure mechanisms such as kink bands which are present due to local compression in bending. The addition of these failure mechanisms means the pullout failure could initiate with a higher apparent stress in the interface than the stress associated with only frictional pull-out, i.e., $\hat{t}^I > \hat{t}^0$. This effect would also be present in mixed-mode specimens which are also subject to some normal ply separation. Cox[48] investigates this so-called "snubbing" effect of angled z-pins and performs an analysis, concluding that "At larger displacements, representative of ultimate failure and rod pullout, snubbing becomes very important. Snubbing stabilizes the pullout process and, in representative cases, strongly affects the displacement and load at ultimate [failure]".

Figure 4.41 shows the calibrated model parameters against the approximated parameter curves derived from single z-pin analysis in Ref. [179] and used for model verification in Ref. [107]. In the present study, $\hat{t}^I$ monotonically increases ($=k\hat{\delta}^0$, following the quadratic damage initiation relationship and BK mixed-mode

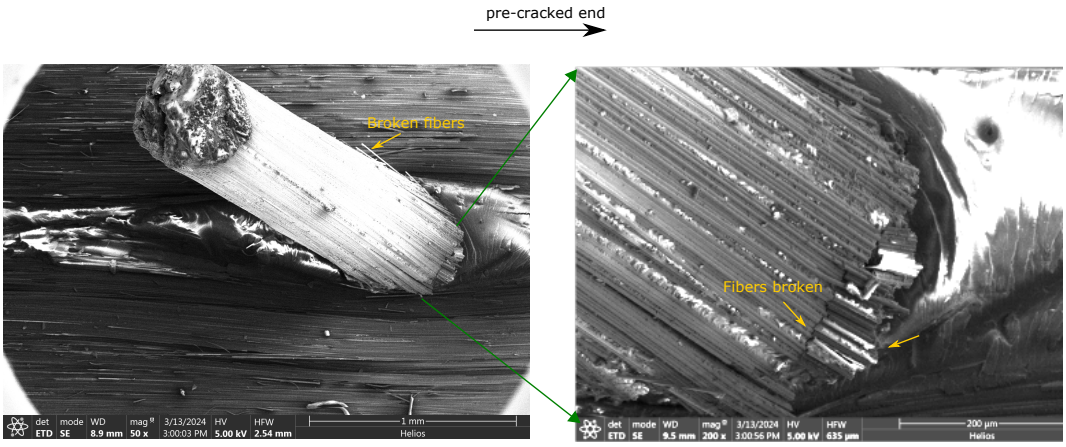

Figure 4.40: Damage features observed in SEM images of z-pins in DCB specimen.

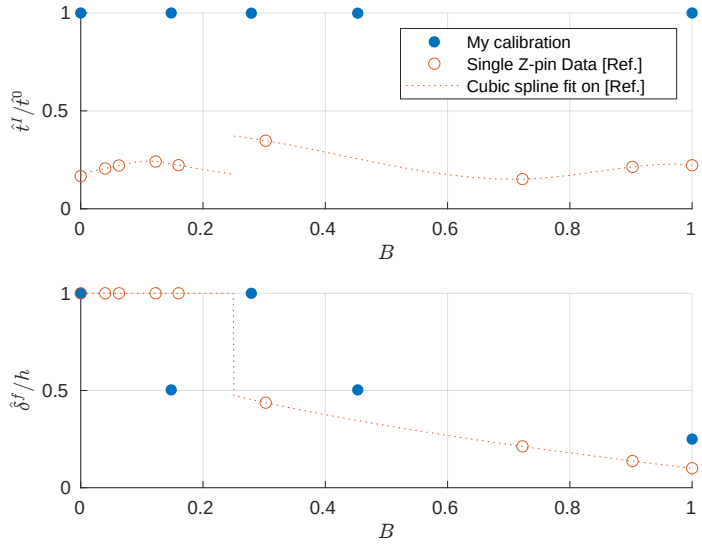

Figure 4.41: Calibrated TSL parameters compared to Ref. [179].

critical energy relationships). The values in the reference indicate a less clear trend and shows a distinct jump around $B = 0.25$ where some z-pins were failing by pull-out while others where ultimately fracturing. The referenced data comes from specimens that are different in thickness (8 mm), epoxy matrix material (8552), layup (quasi-isotropic), and z-pin diameter (0.28 mm) but are the only complete data set in the literature. An additional difference is that the influence of other z-pins is not included in the singe z-pin analysis, though it is clear that the crack opening and sliding is resisted by multiple z-pins in composite structures and a nonlocal effects could be present.

Additional simulations were performed on the test configurations in Mohamed et al [109] using the calibrated values ($\hat{t}^I = k\hat{\delta}^0$) and $\hat{\delta}^f$ based on the spline fit in Fig. 4.41. The overall load-displacement curve

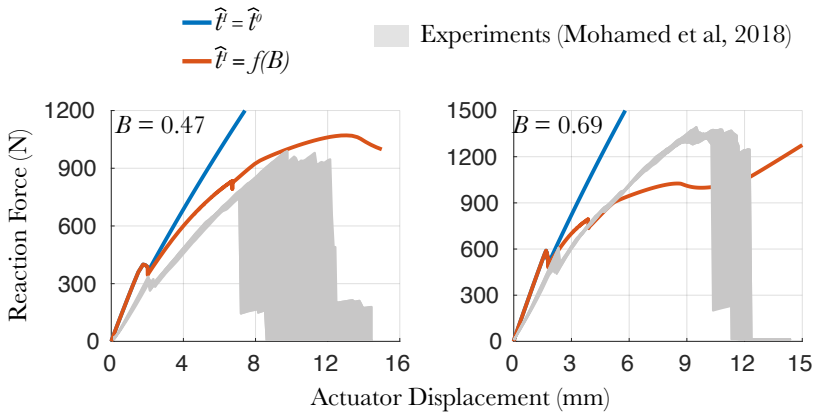

Figure 4.42: Current model prediction using calibrated property curve compared to experimental results for $B = 0.47$ and $B = 0.69$.

shows clearly overpredicts the range of experimental results for both $B = 0.47$ and $B = 0.69$. A second simulation is ran for both cases using the value for $\hat{t}^I = f(B)$ from the curve fit in Fig. 4.42. In this case the slope of the curve closely follows the experiments with some overprediction of the maximum load for $B = 0.47$. For $B = 0.69$, the curve is much more nonlinear than the experiments. The severe overpredictions indicate that the current calibration does not apply to the specimens in Ref. [109]. Although the material system and z-pins were different, one possible explanation could be the added influence of the z-pin inclination in our specimens. The inclination values resulting from the z-pinning methods reported in the literature are not consistent and generally less than the angle in the current specimens (e.g., in Ref. [113] report a majority of z-pins between 10 and 18 degrees from orthogonal). If this is the case then the specimens in Ref. [109] would have pins closer to orthogonal than the current specimens and there would be a less significant snubbing effect like previously described.

A complication during the calibration procedure is that running the calibration simulations is not trivial as the simulations consist of about 27000 degrees of freedom and take 2-3 hours on 4 CPUs of a shared memory compute cluster. A general observation from many calibration runs is that adjusting either $\hat{t}^I$ or $\hat{\delta}^f$ alone does not necessarily correlate to an expected change in the simulation load-displacement and delamination propagation speeds. A sensitivity study was not conducted on these parameters but could further aid understanding of the calibration results.

CHAPTER 5

Compression-after-impact (CAI) Investigations of Z-pinned Composite Laminates

The influence of z-pins on CAI response has been investigated in Refs. [67, 68, 135, 184] using standardized specimen designs according to the residual strength test method in [7]. The focus of these studies involves impact located on a rectangular z-pinned region ([135] also includes a slightly different configuration). The specimens include 16, 24, 32 and 48-ply laminates with cross-ply (0 and 90 degree plies) or multidirectional layups (0, $\pm$45, 90 degree plies). The results from these tests suggest that z-pinning have a direct influence on the projected impact damage overall area and consequently the CAI strength. Part of the work presented here incorporates existing computational methods to investigate CAI in z-pinned composites, which has not been reported before in the open literature.

One drawback of the existing standardized experimental methods is the limited volume of the test specimen. In order to improve understanding of the damage arrestment capabilities of z-pinning for structural configurations, specimens with different configurations are required. Practical considerations not thoroughly investigated in the literature include impact events not centered on z-pinned regions. To address this knowledge gap, an experimental campaign is designed using non-standard specimens which accommodate impact both within and without z-pinned regions. CAI tests are conducted using these non-standard specimens in order to further evaluate the effect of z-pinning on CAI strength and damage progression. The influence of impact location on the overall behavior is investigated using load-displacement results and observations from experimental image analysis of pre- and post-CAI specimen. Evaluation of the damage arrestment capability of z-pins is undertaken by performing interrupted tests followed by ultrasonic C-scan imaging.

5.1 Analysis of CAI Failure in Standard Specimens

5.1.1 Experiments

A team at the Air Force Research Laboratory performed experiments to characterize the effect of z-pinning on the damage resistance and compression strength of carbon-epoxy laminates subjected to low-velocity impact [135]. The work included non-destructive evaluation of damage due to impact and compression loading, as well as measuring the residual static strength of pinned and unpinned samples. Samples were cut from laminate panels consisting of 48 plies of the IM7/977-3 material system were fabricated by co-curing in an autoclave. The balanced quasi-isotropic layup is $[-45/0/+45/90]_{6S}$. One sample was configured with z-pins arranged in a square patch with sides oriented in the laminate principal directions. The reinforcement grid includes pins spaced to achieve 2 % areal density. The unpinned and pinned samples were subjected to impact

events according to ASTM D7136 [6]. A range of impact energies are chosen so as to induce delaminations in the center of the samples while avoiding large surface indentation or penetration. Some samples were drilled into and received a dye penetrant to aid in non-destructive evaluation of impact damage with X-ray imaging. Computed tomography scans of these samples were taken and compiled into a volume of planar "slices" through-the-thickness for visualization. Impacted samples were further cut for compression tests, and loaded into a support fixture in accordance with ASTM D7137 [7]. The samples were checked to ensure that no premature bending or buckling would occur, and were properly aligned. Displacement controlled loading was applied to one end of the samples while recording load and cross-head displacement. The maximum load and overall spread of delamination damage projected from ultrasonic C-scans were captured from samples impacted with 60-80 J.

5.1.2 Numerical Modeling

The CAI problem of z-pinned composite laminates is three-dimensional in nature, dependent on specifications of the laminate and results of the impact event under investigation. To examine the mechanical response under CAI conditions, a finite element model where the domain, material properties, constitutive laws governing behavior, and impact damage characteristics are defined to simulate experimental configurations. Abaqus/Standard is the FEA tool used for this model, utilizing automatic time incrementation and automatic stabilization computed at the beginning of the analysis step in order to advance through the solution of the nonlinear analysis.

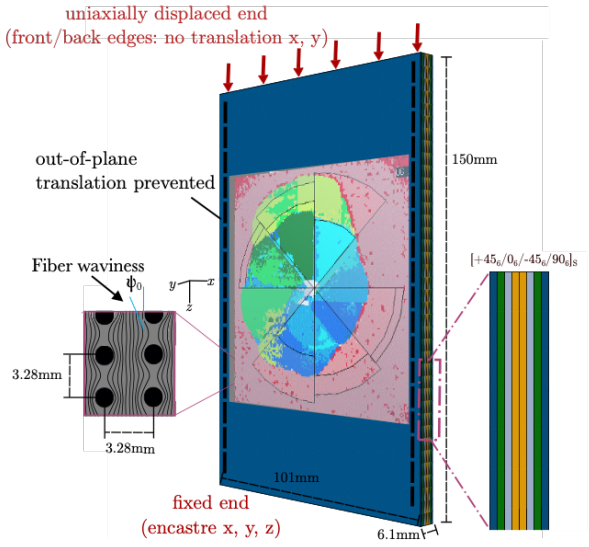

Figure 5.1: Geometry and boundary conditions, impact damage representation.

5.1.2.1 Numerical Domain

The samples tested at AFRL provide a case study for damage progression in a z-pinned composite laminate. The domain is constructed as shown in Fig. 5.1, where the plies, interfaces, and pinned regions are discretely defined within the geometry similar to the experimental samples. The thickness of the test specimen is maintained so that global buckling is not a concern, however the plies are aggregated by fiber orientation so as to reduce computational cost. This means that the actual number of plies and interfaces are reduced from the tested samples but exhibit a response close to that of a many-layered laminate - as also reported in Sun et al [158]. The geometry is discretized by solid, full-integration 8-node brick elements ranging in size from 2 mm around the perimeter to 1 mm along the extents of the initial damage regions. The cohesive zone is chosen to cover a large extent of the available interfaces so as to capture the complete progression of the delamination. Boundary conditions are applied to the outermost surfaces of the geometry with reference to the fixture used in the experimental setup and are represented schematically in Fig. 5.1. Out-of-plane translation is limited along the top edges and along approximate locations of the knife edge positions from the front and back faces as included in the ASTM experimental setup. CAI failure of the laminate is expected to include intra- and interlaminar failure; in particular, Refs. [56, 137] report that the progression of delamination enables sublaminate buckling. Consequently, models for predicting both in- and out-of plane behavior are selected from state-of-the-art methods employed in literature. Additionally, experimentally observed impact damage is idealized to set the initial state of this compression problem.

5.1.2.2 Interface Model

Interlaminar behavior is modeled at the interfaces between oriented plies, where quasi-brittle debonding resulting from multi-axis stresses as observed in CAI experiments of carbon-epoxy laminates is expected [40]. A cohesive zone model is employed to capture the interlaminar damage accumulated during the compression loading [39, 55]. Abaqus offers a contact interaction feature to model cohesive behavior of infinitesimal thickness bonds like those between the plies in a cured laminate. This capability was chosen and requires assignment of cohesive properties to the interaction between nodes on adjacent surfaces. The master-slave roles in the surface interactions are defined based on ply stiffness (0° plies exhibiting the greatest stiffness in the loading direction, followed by the off-axis then 90° plies). The cohesive behavior is expressed with a traction-separation relationship where the initiation and evolution of damage follow a bilinear law, simply depicted in one-dimension in Fig. 5.2. The separation state consists of a normal opening component, δ_I, and sliding displacements in two orthogonal directions, δ_s and δ_t. The normal and tangential directions have initial stiffnesses E_I and $E_I I$, respectively.

This traction-separation law is described by the following equations:

$$t_I = (1-D)E_I\delta_I \tag{5.1a}$$

$$t_s = (1-D)E_{II}\delta_s \tag{5.1b}$$

$$t_t = (1-D)E_{II}\delta_t \tag{5.1c}$$

The degradation of the cohesive stiffness is described as a function of the the current effective separation, $\delta_m = \sqrt{\langle\delta_I\rangle^2 + \delta_s^2 + \delta_t^2}$, separation history, and critical separations:

$$D = \frac{\delta_m^f(\delta_m^{\max} - \delta_m^0)}{\delta_m^{\max}(\delta_m^f - \delta_m^0)} \tag{5.2}$$

where δ_m^f is the effective separation at failure, $\delta_m^{\max}$ is the maximum value of the effective displacement attained during the loading history, and δ_m^0 is the effective separation at onset of softening. Damage increases monotonically.

The onset of softening is determined by a damage initiation criterion based on the traction components, i.e., $\phi(t_I, t_s, t_t) = 1$. A so-called maximum traction function is chosen where the values of the traction components are compared to the maximum traction that can be carried in each direction:

$$\phi = \max\left\{\frac{\langle t_I\rangle}{t_I^0}, \frac{t_s}{t_{II}^0}, \frac{t_t}{t_{III}^0}\right\} \tag{5.3}$$

The "0" superscript is the maximum traction value that can be sustained prior to bond softening in each direction. Since experiments show that z-pinning enhances interlaminar properties we consider that debonding of the reinforced laminate occurs due to modified property values of the traction-separation law. Furthermore, the maximum stress criterion remains convenient to model the effect of pin debonding and a linear degradation is suitable to model frictional pulling out as it bridges the interlaminar crack. The interface failure

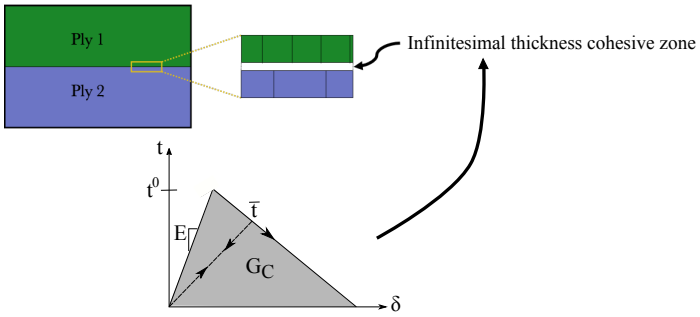

Figure 5.2: Interlaminar damage model (under a single mixed-mode condition).

criterion must account for mixed-mode loadings and z-pin failure mechanisms expected under CAI conditions. The energy power law form is taken in the CAI studies in Refs. [29, 154] and employed in the current model.

$$\left\{ \frac{G_I}{G_{IC}} + \frac{G_s}{G_{IIC}} + \frac{G_t}{G_{IIC}} \right\} = 1 \tag{5.4}$$

where G denotes the dissipated energy due to crack opening. The IC and IIC subscripts denote the critical fracture energy required for delamination under pure Mode I and Mode II conditions, respectively. The effective separation at failure is related to an equivalent critical energy under mixed-mode conditions by the expression $\delta_m^f = 2G_c/t_m$, where $t_m = \sqrt{\langle t_I \rangle^2 + t_s^2 + t_t^2}$ is evaluated when $\phi = 1$. The equivalent critical energy, G_c, is calculated for the current deformation state as:

$$G_c = \left[\frac{1}{G_I + G_s + G_t} \left(\frac{G_I}{G_{IC}} + \frac{G_s}{G_{IIC}} + \frac{G_t}{G_{IIIC}} \right) \right]^{-1} \tag{5.5}$$

The traction-separation response also follows a linear unloading and reloading path from the softening envelope defined by D to the zero traction-zero separation state. Mode I and Mode II energy components are calculated based on the current separation and current state of the damage variable as:

$$G_I = \int_0^{\delta_I} t_I(D)\, d\delta_I \tag{5.6}$$

$$G_s = \int_0^{\delta_s} t_s(D)\, d\delta_s \tag{5.7}$$

$$G_t = \int_0^{\delta_t} t_t(D)\, d\delta_t \tag{5.8}$$

The values of Table 5.1 are apparent fracture toughness associated with the effects of z-pins and chosen from the analyses presented in Refs. [25, 92, 134].

Table 5.1: Interlaminar material parameters

Parameter	Unpinned Region	Pinned Region	Unit
t_I^0	15	30	MPa
t_{II}^0	60	250	MPa
G_{IC}	0.218	3.800	J/m^2
G_{IIC}	0.650	1.648	J/m^2
E_I	8644	12000	MPa
E_{II}	4660	4194	MPa

5.1.2.3 Ply Model

In order to account for the influence of kink bands on the compressive behavior the model presented in Ch.2 is also employed in the current study. The formulation is exactly the same as previously presented (see also [60]. The user material capability of Abaqus allows application of the fiber kinking model and tracking of matrix damage with a state variable. Additionally, fiber waviness is introduced by varying the fiber direction (and thus, element) along the fiber orientation direction of plies, as expressed in Eqn. 5.9.

$$\psi(x,y,z) = \tan^{-1}\left(\tan\psi_0 \cdot \sin\left(\frac{\pi z}{l}\right)\right) \tag{5.9}$$

where the misalignment of the fibers is described by a maximum misalignment angle, ψ_0, and periodic wavelength, l at a given longitudinal position, z. The composite material property values are selected are based on previous work with the material system and experimental results in Bogdanor and Oskay [31], and listed in Table 5.2. The 3 component indicates the fiber axial direction; the superscripts f and m indicate properties for the fiber and matrix constituents, respectively.

Table 5.2: Elastic and damage parameters of the material constituents.

Elastic Parameters			Damage Parameters		
Parameter	Unit	Value	Parameter	Unit	Value
$E_1^{(f)}$	GPa	12.45	$a^{(\mathrm{m})}$	$\mathrm{MPa}^{-1/2}$	8.0
$E_3^{(f)}$	GPa	305.0	$b_n^{(\mathrm{m})}$	N/A	16.0
$G_{13}^{(f)}$	GPa	146.0	$b_s^{(\mathrm{m})}$	N/A	16.0
$\nu_{12}^{(f)}$	N/A	0.291	$\upsilon_0^{(\mathrm{m})}$	$\sqrt{\mathrm{MPa}}$	0.0
$\nu_{31}^{(f)}$	N/A	0.206	$c^{(\mathrm{m})}$	N/A	0.0
$E^{(\mathrm{m})}$	GPa	3.70	ψ_0	$^\circ$	2.0
$\nu^{(\mathrm{m})}$	N/A	0.377	l	mm	0.5

5.1.2.4 Impact Damage Representation

The third component of the CAI problem is incorporation of an initial damage state due to an impact event. Ultrasonic C-scan images from Ranatunga et al [135] are analyzed to determine the damage pattern resulting from low-velocity impact. Examination of time-of-flight scans from 7 impacted samples (of the same energy-level event) indicate a spiral pattern of oriented delamination regions through the thickness of the laminate. The delaminations increase in size moving from the interface most near the impacted face towards to rear-most interface. Additional examination of x-ray images indicate that the delaminations are bounded by severe matrix cracks (also described in [34]). Findings by Wallentine and Uchich [172] and Hull and Shi [84] elucidate the interactions of delamination and matrix cracking, therefore the delaminated regions are assumed to correspond to heavily damaged ply material also. This information is combined and applied to the laminate by removing material in simplified "petal"-shaped regions with dimensions corresponding to the

delaminations exhibited in the c-scan images, as shown in Fig. 5.1.

5.2 Results

Structural analysis is undertaken with a simulation of an unreinforced laminate with an initial damage state based on the image analysis of a particular impacted state represented as described in the previous section. The simulation load-displacement curve is displayed in Fig. 5.3a, wherein the laminate initially exhibits a linear response until a "knee-point". At this knee-point the load-end displacement response becomes non-linear as delamination spreads. Delamination progresses between plies from the outer extents of the impact damage region, and in the direction corresponding to the fiber orientation in adjacent plies. Peak load is indicated by a significant drop in load and nearly matches that of the experiments. At peak load, the projected delamination pattern covers the width of the laminate, where as demonstrated in Fig. 5.3b, significant sublaminate buckling follows delamination of the outer plies. Delamination progresses majorly at the interfaces which were initially damaged, and in the direction of fiber orientations in adjacent plies as displayed in Fig. 5.4. The largest continuous delamination zones occur between the $+45^\circ/0^\circ$ interfaces, while no delamination progression is observed at the middle interfaces of the laminate where little impact damage was represented. The damage state at peak load is also characterized by kink band formation as displayed in Fig. 5.5. We observe that kink bands have formed across the width of the ligaments created by the impact damage, and correspond to delaminated regions of the outer plies. At the middle interface, however, we also observe matrix damage in the longitudinal direction extending from the epicenter of the impact damage.

A second simulation is undertaken for a z-pinned laminate using enhanced interlaminar properties. The enhanced properties entail considerably larger critical fracture energies for both normal and sliding separation

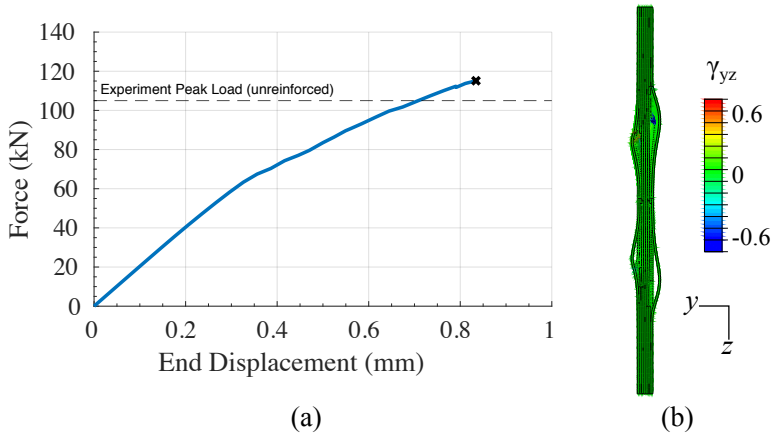

Figure 5.3: (a) Predicted CAI response; (b) Cross-section view at mid-width of the specimen at peak load.

corresponding to the crack-bridging and pin pull-out effects in a z-pinned laminate. The damage initiation stress is slightly increased along with the normal stiffness, which accounts for the effect of co-curing the pins in the laminate, where thermal stresses act to toughen the initial interlaminar response. The tangential stiffness is slightly reduced, corresponding to Mode II experimental observations. The response curve for the z-pinned configuration is shown in Fig. 5.6, where the load continues to increase after reaching a mild plateau prior to the end displacement at which the unreinforced laminate reaches a peak load; sudden failure is not evident. However, the laminate load-displacement curve matches that of the unreinforced configuration until the knee-point, and continues to exhibit a linear response with further end displacement. Like in the unreinforced laminate case, the behavior becomes nonlinear as delaminations extend from the initial damage regions. The delaminations grow from the impact damage regions however to a much reduced extent

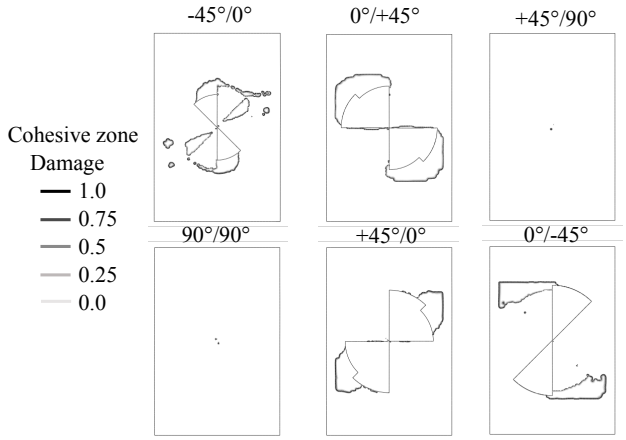

Figure 5.4: Progression of delaminations in the interfaces of the unreinforced laminate at peak load.

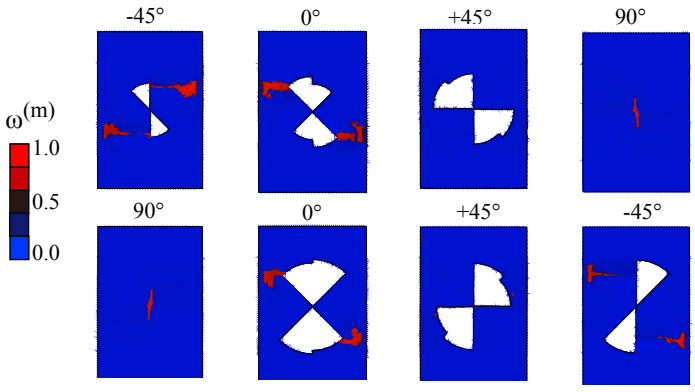

Figure 5.5: Progression of kink bands in each ply of the unreinforced configuration at peak load.

compared to the unreinforced laminate. In addition we observe that kink bands form at a lower load and throughout the laminate. In both cases, the kink bands are prominent in the 0° plies across the width towards the laminate edges and the outer -45° plies in the same general path, corresponding to the progression of delamination (Fig. 5.7).

5.2.1 Discussion

In comparing the progression of delamination in the two laminate configurations we see that the same peak load is achieved with a smaller extent of delamination in the laminate with enhanced interlaminar properties. The cumulative delamination region enlarges only slightly with increasing end-displacement past an apparent peak load. Figure 5.7 shows only a small and less uniform change in the delamination regions over a 0.2 mm end displacement in all but the rear $+45^\circ/0^\circ$ and $0^\circ/-45^\circ$ interfaces. These interfaces are nearest the non-impacted side and included the largest initial damage regions. It seems that the front half of the laminate remains stiffer than the rear half, and so the load is able to transfer and proceed to damage the weaker remaining material. Overall, the enhanced interlaminar properties appear to arrest delamination where the initial damage state is not severe, and consequently produce a more stable CAI collapse. The predicted CAI strength is underpredicts the experiment result. Although the traction-separation relationship employed in this investigation reveals the general effects of enhanced interlaminar properties, the reduced strength suggests that the damage model does not fully capture the physical energy dissipation in the case of a z-pinned lamiante. As explored by other researchers, a more complex constitutive relationship (e.g. a tri-linear traction-separation law) simulates z-pin crack-bridging in the case of mixed-mode loadings [108]. Moreover, analysis of cohesive zone nodal displacements reveals that tangential sliding matches the delamination pattern better than normal separations and so capturing mixed-mode behavior is necessary. Not only do the interlaminar properties affect the CAI outcome but we see that the initial damage state greatly influences the progression of damage in the laminate.

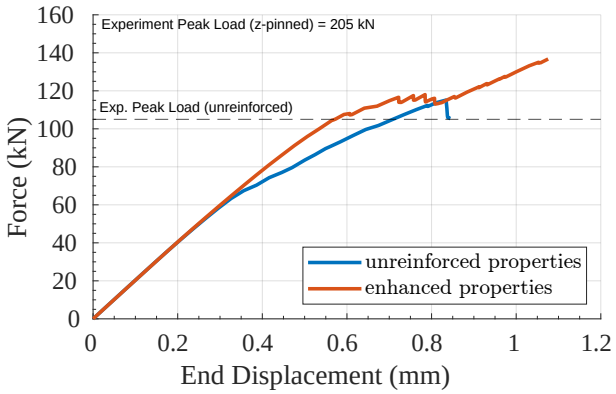

Figure 5.6: Simulation response curves compared to experiment peak load values.

Though the predominant damage mechanism in the simulations appears to be delamination, there is interaction of this damage mode with ply failure due to kink bands. In the unreinforced laminate, the kink bands form due to sublaminate buckling which is a result of delaminated regions. The laminate with enhanced interlaminar properties exhibits initial kink band formation at a load point earlier than in the unreinforced laminate response, however there is not as significant of a knee point, thus demonstrating less severe delamination and subsequent sublaminar failure. Kink bands propagate to the edges of the z-pinned laminate in a path perpendicular to the loading direction, driven by collapse of the 0° plies. No sudden drop in load bearing capability is observed, and in fact delamination does not progress in interfaces of both the front and rear halves of the laminate like in the unpinned configuration. Compared to the progression of damage in the unreinforced laminate, which includes a visibly broad crack front, the laminate with enhanced interlaminar properties exhibits a smaller region of severe out-of-plane deformation of the outermost plies while the apparent strength and toughness is increased. Analysis of the deformation of the unreinforced and z-pinned laminates shows a more concentrated deformation region in the outer plies of the enhanced laminate. Figure 5.7b displays this concentrated shape of sublaminate buckling in the laminate with enhanced interfaces. While the deformation

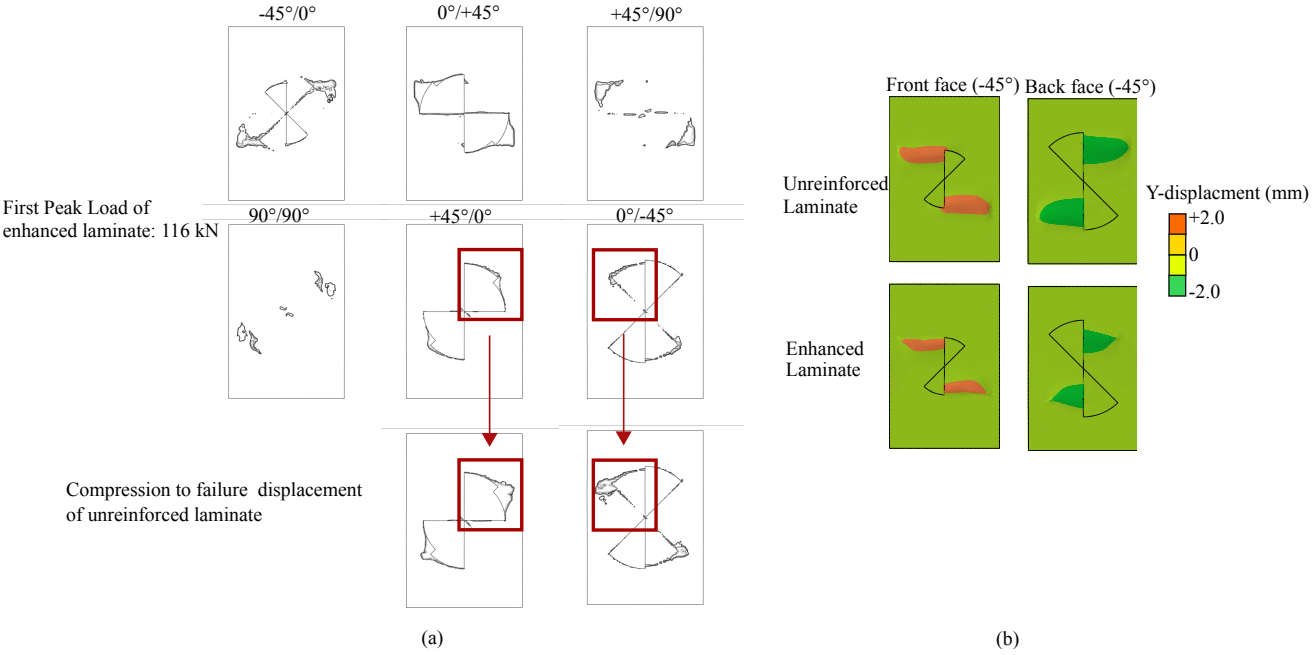

Figure 5.7: (a) The spread of delamination stagnates at all but two interfaces in the z-pinned configuration; (b) out-of-plane deformation fields of the laminates after 0.8mm end displacement.

pattern is similar to the experiments in Ref. [158], both unpinned and z-pinned samples exhibit concentrated sublaminate buckling and fiber fracture at mid-height of the laminate in Refs. [56] and [184], respectively. The impact damage images used in this analysis do not clearly show major ply damage and delamination concentrated at the epicenter of the impact, however modifying the initial damage state to include a cylinder

or cone of damage through the thickness like used in Refs. [119, 177] could lead to a similar result.

5.2.2 Conclusions

In this study, models for tracking multiple failure mechanisms was used to simulate CAI failure of a z-pinned laminate. Cohesive zone modeling with existing tools takes into account the apparent effects of z-pinning on interlaminar properties. State-of-the-art techniques were employed in finite element analyses including a surface-to-surface cohesive zone model to describe progressive delamination in z-pinned and unreinforced laminate regions, with the exact formulation chosen based on other published findings. A recently developed multiscale compression damage model for the plies and an idealized impact damage pattern from experimental observations were applied to predict the failure process in a particular z-pinned laminate configuration. The simulation results provide evidence of damage arrestment due to z-pinning. The simulations indicate significant ply damage along with delaminations in the CAI response. Analyses that neglect modeling of ply failure in the CAI response may not completely describe the failure process. Consequently, an accurate approach to modeling the CAI problem requires integrating mechanistic damage models which can predict the complex interactions driving damage.

5.3 Experimental Analysis of CAI Failure in Non-standard Specimens

5.3.1 Materials, Specimens, and Test Methods

Rectangular panels of dimension 355.6 mm x 330.2 mm were hand-laid with 32 plies of UD IM7/977-3 prepreg tape using standard procedures and tools in an OEM-spec clean room. Plies were tacked together using a non-stick roller and debulked under vacuum at approximately 120 degree Fahrenheit every ply to build the layup $[-45/0/+45/90]_{4S}$. The panels were sent to a third party where T650-42/epoxy z-pins with 0.51 mm diameter were inserted with a mechanical gurney at 64 pins/in^2 in the region indicated in Fig. 5.8. Following z-pinning the panels were autoclave cured using the same parameters as for the UD panels. Ultrasonic scanning was performed on the panels in an immersion tank. The panels were non-destructively inspected for defects using back-wall and through-thickness C-scan images.

Impact experiments were conducted using a drop-weight approach. The drop tower and associated equipment are shown in Fig. 5.9a. The laminate panel was clamped using the frame shown in Fig. 5.9b. Impacts were located in three different locations with respect to the z-pin field as marked in Fig. 5.8 using the rounded-head impactor shown in Fig. 5.9c. The impact energy was set using the drop-height and mass of the impactor. Ultrasonic scans were taken post-impact to help characterize the initial state for CAI tests. Both handheld and computer-controlled scanning devices were used to capture images. The maximum extent of damage is measured using through-transmission and back-wall scans while time-of-flight/gated scans show damage

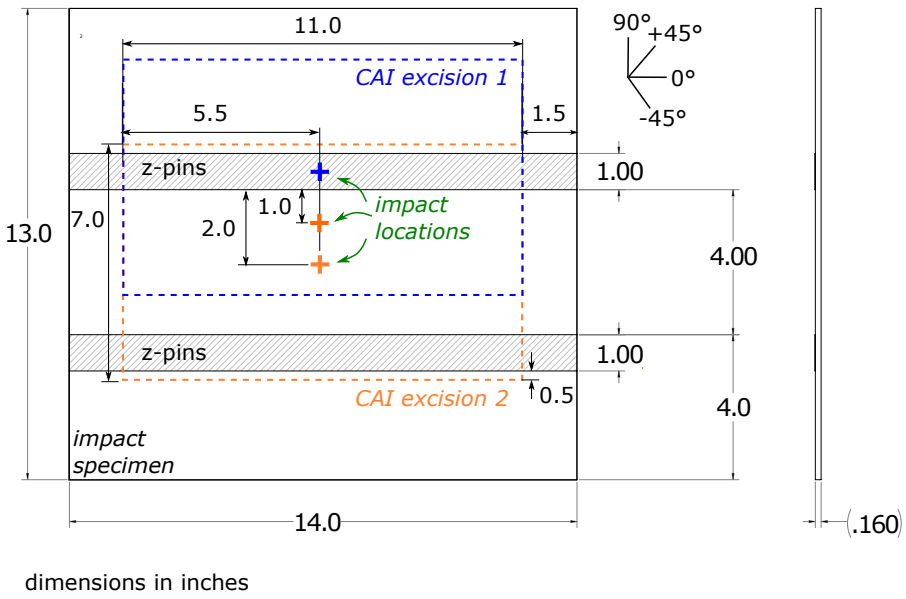

Figure 5.8: Laminate panel dimensions, impact locations and CAI specimen excision plans.

profiles at 8 intervals through the thickness (approximately 0.5 mm depth ranges). Following impact and ultrasound scanning, the specimens were prepared for CAI testing by excising panels with waterjet cutting, and edges were then ground.

Screening CAI tests were performed on unpinned 12 inch by 12 inch specimens of the same layup using an anti-buckling fixture and corresponding boundary conditions like described in [7] (knife-edges near lateral edges). The specimen failure was the result of global buckling away from the impact damage. Recent experiments have also shown that specimen dimensions influence the overall CAI behavior of laminates without z-pins [100] and for large unsupported areas, the primary failure mechanism is global buckling.This type of failure is not delamination-driven and therefore not useful for investigating the effects of z-pinning on CAI failure. To address this undesirable behavior a different anti-buckling fixture was selected based on previous AFRL projects with an aerospace industry OEM. Platens apply vertical loading to the test fixture as shown in Fig.5.10a. The test fixture design is such that the specimen is contacted on its bottom and top surfaces during loading and faceplates constrain out-of-plane displacements. The faceplates include small cutouts for strain gages to check alignment and a central window to not interfere with the existing damage as shown in Fig. 5.10b.

The CAI investigations entail two sets of tests. The first set of tests was conducted to study the effect of impact location on the overall CAI behavior - in particular strength. For this purpose, 60 J impacts were located in one of two positions: centered between the z-pinned regions and centered in one of the z-pinned regions. The plan labeled CAI excision 1 was used to create specimens with impact located on the z-pinned

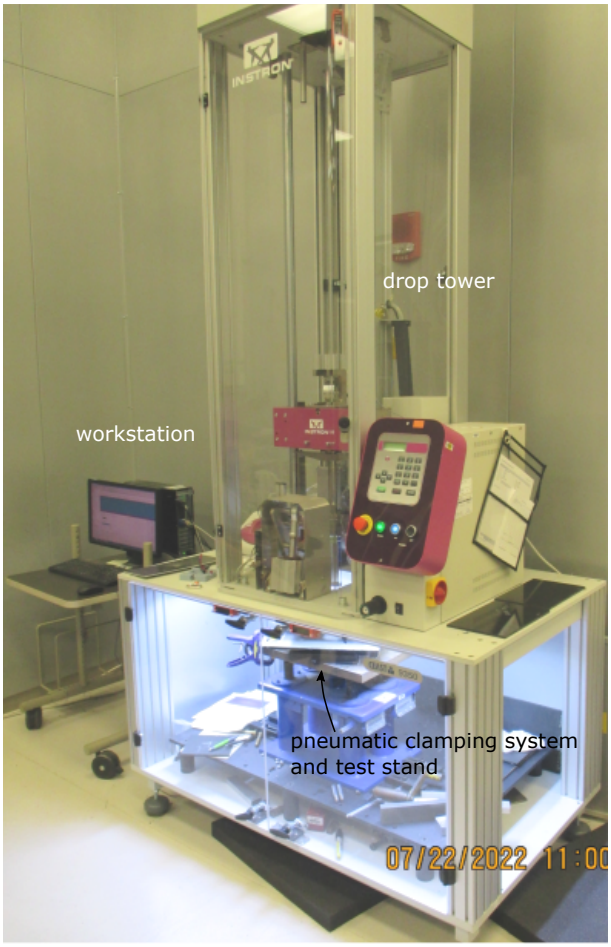

(a)

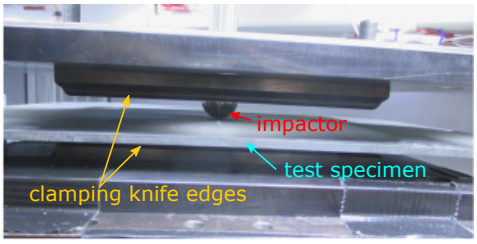

(b)

(c)

Figure 5.9: (a) Drop tower, workstation, and test stand, (b) clamping frame, and (c) impactor.

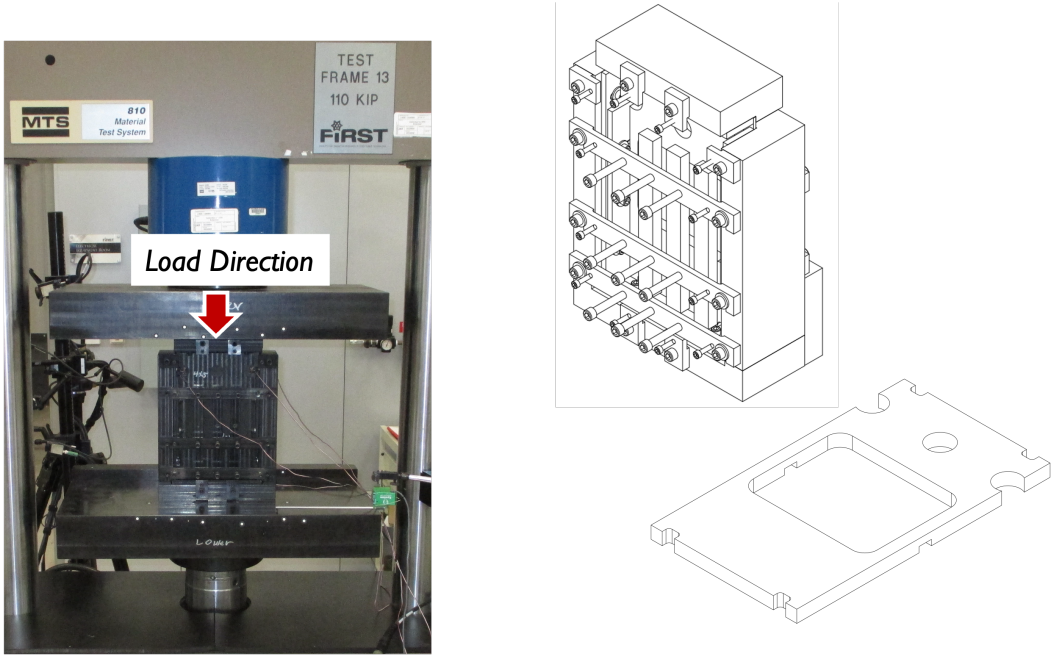

(a) (b)

Figure 5.10: (a) CAI fixture loaded on test frame; (b) schematic of fixture and faceplate.

region and the plan labeled CAI excision 2 was used to create specimens with impact centered between the z-pinned regions. These plans are designed to center the impact locations for the CAI tests.

The second set of CAI tests were performed on specimens with impact “eccentrically-located”. Impacts of 70 J were centered 1 inch from the z-pinned region and remained off-center during CAI testing using the cut plan labeled CAI excision 2. Six specimens were loaded until failure. Tests interrupted prior to ultimate failure were performed on additional specimens to provide new damage progression information. The actuator displacement was used to determined the points at which to interrupt additional tests. Interrupted tests were performed to 87%, 98%, 99%, and 99.5% of mean displacement at ultimate load from specimens loaded until failure. After a test was interrupted, loading was removed from the test fixture and the specimen was then removed from the test fixture for ultrasonic scanning. Sequential tests were performed on the same specimens by ascending % of mean displacement at ultimate load. The quantities of specimens and test sequences are reported in Fig.5.11.

5.3.2 Results and Discussion

The overall load displacement curves for the specimens subjected 60 J impact are shown in Fig.5.12. The responses are fairly linear and there is not a drastic difference in the behaviors exhibited by the specimens with impact centered between the z-pin fields (denoted ”C”) and on a z-pin field (denoted ”Z”). The mean maxi-

Qty.	87%	98%	99%	99.5%	ultimate
1	x		x		x
2			x	x	x
2		x	x		x
6					x

Figure 5.11: Damage progression CAI test matrix.

mum load for the C specimens is 168.2 kN, standard deviation (SD): 255 N. The mean for the Z specimens is 177.7 kN (SD: 2.85 kN). This is different than other experimental results for 32-ply specimens subjected to same energy impact but with and without z-pins arranged in a grid [135, 184]. In those cases, the maximum load was about 40% larger. The projected damage area was not consistently different between the C and Z impacts, so this could be a factor explaining the current results. NDI was undertaken using ultrasonic C-scans and visual observation of the CAI specimens after testing. Images for the C specimens are shown in Fig.5.13. The ultrasonic scan in Fig.5.13b shows some delamination growth from the centered impact location above mid-height, however the primary failure path aligns with the center of the impact (the smaller almost circular region in Fig.5.13a). The photos in Fig.5.13c show exterior cracking on the faces of the specimen as well as the edges aligning with the main delamination path shown in Fig.5.13b. The photo shows how the delamination reaches the edges of the specimen.

Images for specimen Z are shown in Fig.5.14. The post-CAI ultrasonic scan in Fig.5.14b shows evidence of a broader delamination region with width approximately equal the width of the impact damage footprint. The photos in Fig.5.14c show evidence of local buckling on the face of the specimen. Images also show the presence of broad delaminations on the edges, most distinctly near the mid-thickness of the specimen.

The shapes of the delamination regions in the C specimen indicates that delamination spread in the lateral direction from the entire footprint of the impact damage until the z-pinned region. Delamination as well as through-thickness lamina cracking still propagate to the edges of the laminate but in a confined region aligning with the center of impact (which is also mid-height of the specimen. This is in contrast to the Z specimen where the delamination path has nearly consistent breadth across the entire transverse direction. The end displacement at failure is larger in the Z specimens, which is likely due to the buckling of the outer sublaminates as opposed to the more brittle cracking present in the C specimens. Gated ultrasound scans confirm the most broad delaminations present in Fig. 5.14 exist around 2 mm depth though broad delaminations are also present in the back half of the laminate.

The overall load-displacement response of eccentric impact CAI tests ran to failure are shown in Fig. 5.15. The responses are fairly linear until 1.2 mm displacement where some nonlinearity is apparent in some of

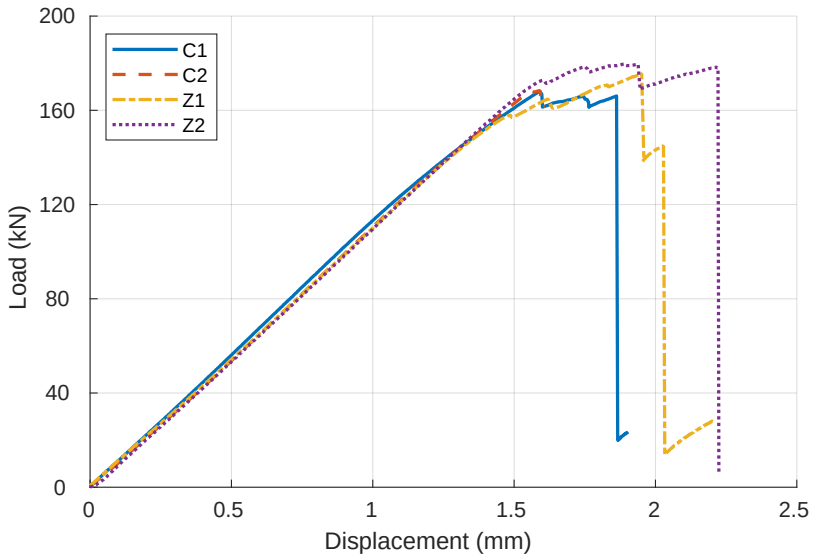

Figure 5.12: CAI load displacement curves for specimens with impact in between (C) and on (Z) the z-pin fields.

the curves and are similar to the responses of specimens C and Z. Audible cracking is also observed starting around this displacement. The mean maximum load is 169 kN and standard deviation is 10.9 kN. The mean ultimate load is 156.9 kN and standard deviation is 13.4 kN. The mean displacement to failure was $w_{max} = 1.625$ mm. The progression of damage is studied using images from sequential tests as shown in Fig. 5.16. The extent of damage in the previous state is shown by a white outline on each of the post-loading images. There is obvious growth of the delamination footprint at $87\% w_{max}$ in the region between the z-pinned fields, in the longitudinal as well as transverse directions. There does not seem to be substantial delamination growth in the z-pin field with existing impact damage at this loading. There is more delamination growth in the central unpinned region and some growth into the opposite z-pin field at $99\% w_{max}$. The overall damage footprint is tapered in the transverse direction in the scan taken after ultimate load – similar to the damage footprint in Figure 81b.

Damage regions were also extracted from gated ultrasound images pre- and post-CAI for a different specimen with a similar impact damage projection. These are shown in Fig.5.17 and show a nearly circular footprint of impact damage up to a depth of around 1.8 mm. The thickness resolution of the images do not allow an interface by interface examination, however there appears to be all interfaces represented in the scans (i.e., -45/0, 0/+45, +45/90 interfaces). There was no detectable delamination in the same approximate depths post-CAI. The images from approximately 1.8-4.8 mm indicate that the interfaces which showed an initially large damage footprint were the primary locations of delamination growth. The images around 2.1-3.1 mm depth show the largest breadth of damage at the edges of the laminate post-CAI. The breadth of damage in

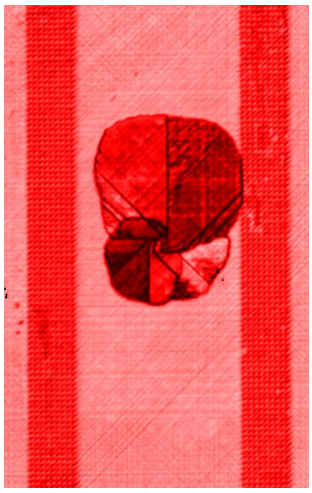

(a)

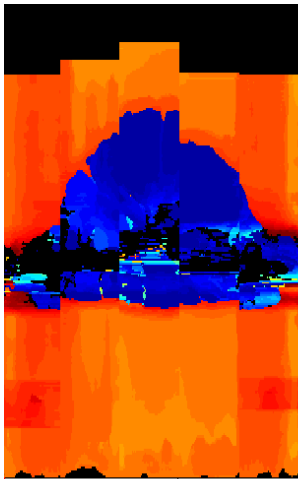

(b)

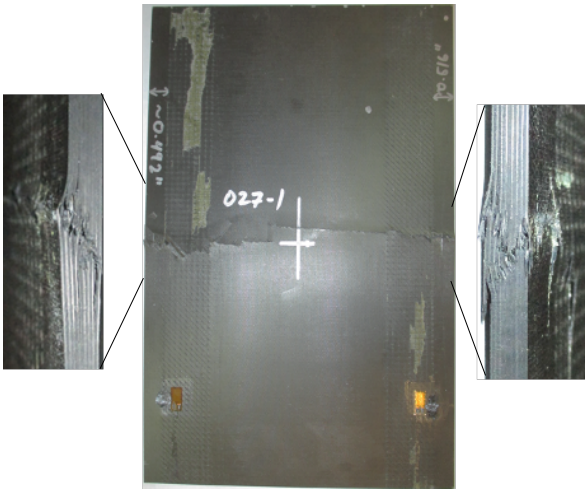

(c)

Figure 5.13: (a) Pre- and (b) post-CAI ultrasonic C-scans. (c) Post-CAI photos of specimens with impact centered between the z-pinned regions.

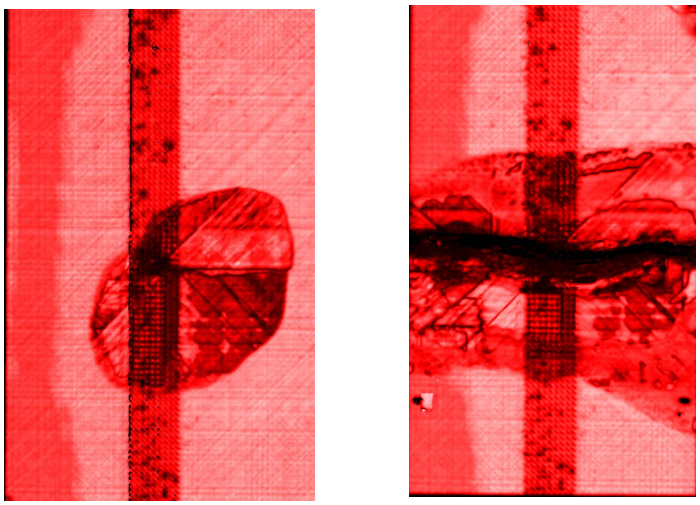

(a) (b)

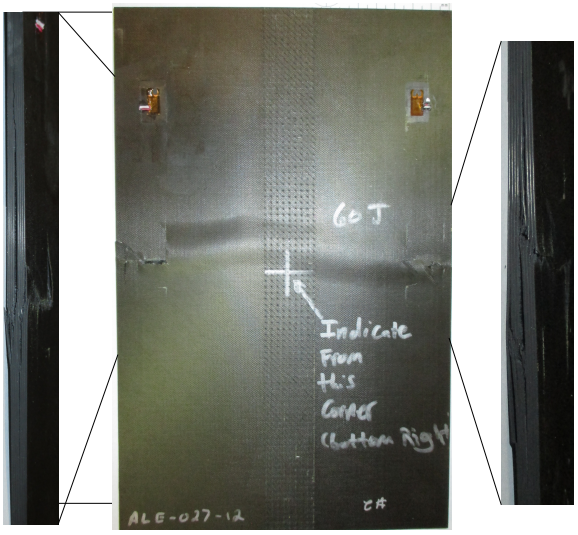

(c)

Figure 5.14: (a) Pre- and (b) post-CAI ultrasonic C-scans. (c) Post-CAI photos of specimens with impact centered on the z-pinned region.

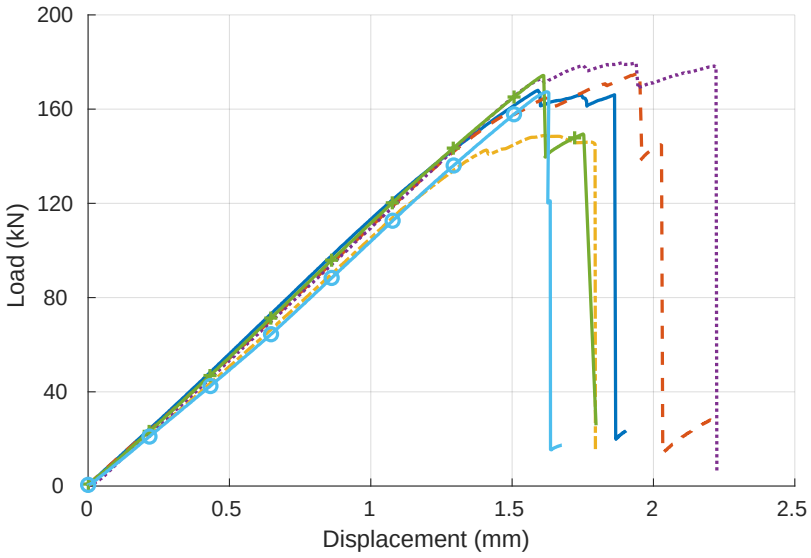

Figure 5.15: Load-displacement results for the z-pinned CAI experiments.

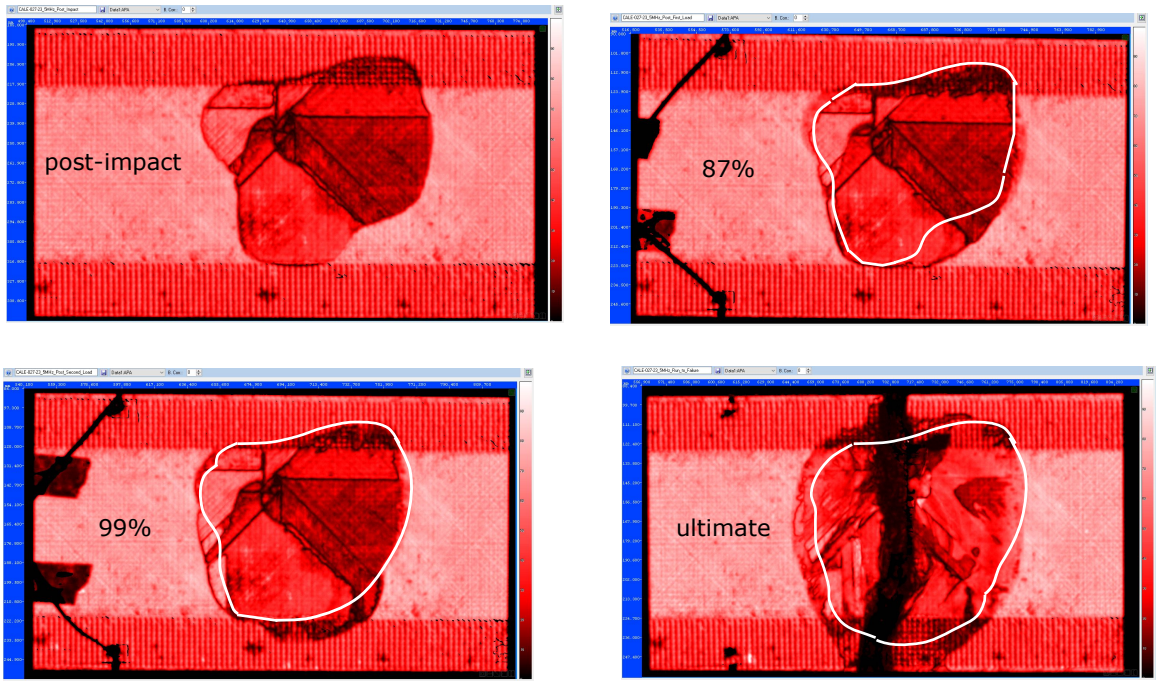

Figure 5.16: Back wall ultrasonic C-scans from sequential tests loaded to 87%w_{max}, 99%w_{max}, and to ultimate failure.

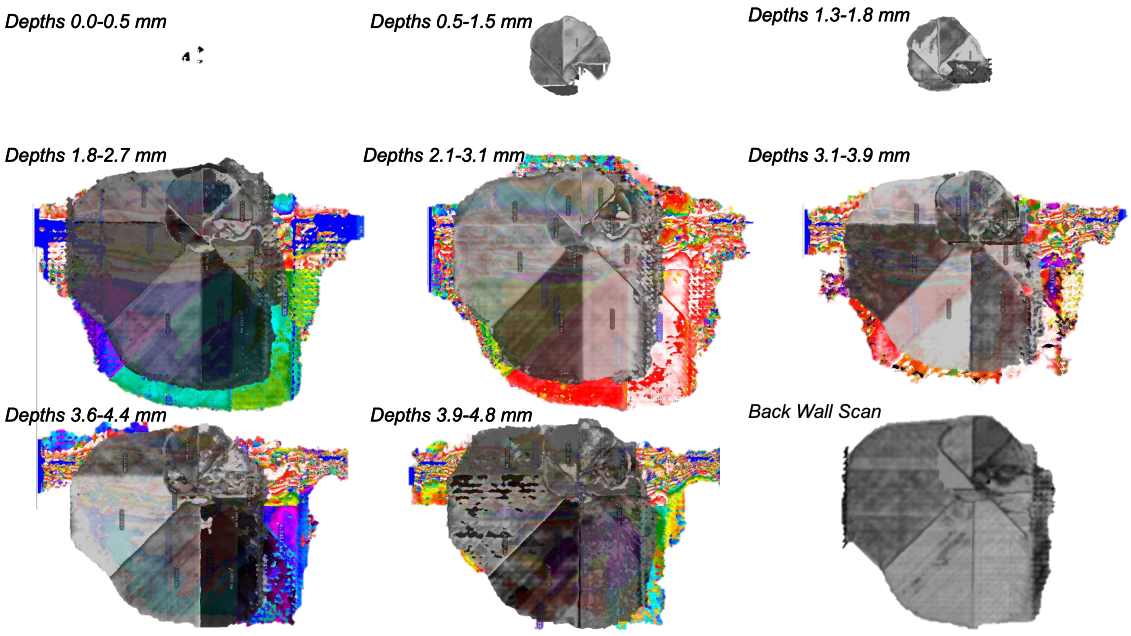

Figure 5.17: Gated ultrasonic C-scans from a specimen loaded to ultimate failure. The impact damage is overlaid in black and white on the colored post-CAI damage.

general measures larger at the edge opposite the impact site. Delamination apparently did not grow quickly in the z-pinned region which had existing delamination due to impact since the overall failure pattern is not biased.

5.3.3 Conclusions

The experimental results and analysis from the CAI study on the non-standard test configuration provide two sets of information. The first aspect comparing the results from laminates with impact on and between z-pinned regions agrees with results of other studies where overall impact damage size has a strong influence on the residual strength. In the current study, the peak load from CAI specimens impacted on or between z-pinned regions were indistinguishable. The overall damage footprint post-CAI is different in the specimens, however, and results from ultrasonic C-scan images show how a broad delamination region does not propagate through the z-pinned regions causing ultimate failure. The ultimate failure in the specimen impacted on the z-pinned region is characterized by a broad delamination of near uniform height (longitudinal direction) near the mid-plane of the specimen and extending to the edges of the laminate. The effect of this delamination

is the formation of two effective sublaminates which buckle and the ultimate load is delayed with respect to actuator displacement – which was also observed in previous studies with the standard test configuration and impact on a z-pinned region.

CHAPTER 6

Recommendations for Future Work

The kink band problem is not unique to the unidirectional, or prepreg tape, composite with CFRP material properties investigated here. Future work to facilitate design of materials could include validating the model against different material systems. Experimental results of a unidirectionally reinforced metal matrix composites (MMC) also present kink band failure (see e.g., [182]) and the authors are not aware of mesoscale investigations with MMC material properties. Additionally, the proposed methodology is applicable to other long fiber reinforced composites including 2D/3D fiber preform reinforced composites where kink band failure occurs (see e.g., [88]) by appropriately defining the local fiber orientation in the part. Woven preforms can also be investigated by the proposed approach, but that requires a change in the microstructure and the associated reduced order model.

Because of the multitude of failure modes and size of the DENC model, parametric analyses were not performed (e.g. with fiber waviness characteristics or matrix shear nonlinearity) or predicting of the progression of delamination. The experimental data show a strong variation of matrix cracking pattern ahead of the notch tip in addition to splitting and kink band onset time. A probabilistic sampling of material properties that reflect material heterogeneity and uncertainty in model parameters could provide insight to the sources of variation of experiment load-strain results. Future work could include parametric studies to investigate different sources for the macroscopic nonlinearity in the overall load-strain results, and incorporate delamination progression well.

The trilinear cohesive zone model could benefit from additional calibration using results from experiments with the same material system conducted with a larger mode-mix. The design of the z-pinned specimens could be improved to better take advantage of the SLB and MMB experimental configurations. Experiments could also be conducted with z-pins inserted closer to orthogonal and higher resolution (or closer) in-situ imaging to try to capture some the z-pin behavior. Additional understanding of z-pin failure mechanisms under mixed-mode and pure Mode II loading could come from X-ray CT imaging of the current specimens. The model can be improved by sensitivity studies, which would help understand how the critical points in the TSL affect the overall load response and delamination crack propagation.

A second CAI model is proposed to further analyze the non-standard experimental configuration. Similar to the DENC analysis, the size of the CAI model poses computational challenges. Suggestions for continuing this work to speed up the simulations while using a more refined mesh include performing explicit analyses. This change in approach requires model changes compared to the current analyses. These changes include

how the CZM can be implemented using Abaqus (e.g., the contact pair algorithm is not compatible with cohesive properties so the general contact algorithm must be used). The usual work to minimize energy in the dynamic analysis are also needed (e.g., choosing the appropriate mass scaling to achieve a reasonable computation time). Additional model improvements should also include representation of impact damage based on experimental images through a mesh mapping procedure and deploying the calibrated trilinear z-pinned interface model.

REFERENCES

[1]G. Allegri, M. Yasaee, I. Partridge, and S. Hallett. A novel model of delamination bridging via z-pins in composite laminates. *International Journal of Solids and Structures*, 51(19):3314–3332, 2014.

[2]G. Allegri and X. Zhang. On the delamination and debond suppression in structural joints by z-fibre pinning. *Composites Part A: Applied Science and Manufacturing*, 38:1107–1115, 4 2007.

[3]O. Allix and L. Blanchard. Mesomodeling of delamination: towards industrial applications. *Composites Science and Technology*, 66(6):731 – 744, 2006. Advances in statics and dynamics of delamination.

[4]F. Andrade, J. C. de Sá, and F. A. Pires. Assessment and comparison of non-local integral models for ductile damage. *International Journal of Damage Mechanics*, 23(2):261–296, 2014.

[5]A. S. Argon. Fracture of Composites. *Treatise on Materials Science and Technology*, 1:79–114, 1972.

[6]ASTM. D7136m-15, standard test method for measuring the damage resistance of a fiber-reinforced polymer matrix composite to a drop-weight impact event. Technical report, ASTM International, 2017.

[7]ASTM. D7137m-17, standard test method for compressive residual strength properties of damaged polymer matrix composite plates. Technical report, ASTM International, 2017.

[8]ASTM. D7905m-19e1, standard test method for determination of the mode ii interlaminar fracture toughness of unidirectional fiber-reinforced polymer matrix composites. Technical report, ASTM International, 2019.

[9]ASTM. D5379m-19e1, shear properties of composite materials by the v-notched beam method. Standard, ASTM International, 2021.

[10]ASTM. D6641m-16e2, compressive properties of polymer matrix composite materials using a combined loading compression (clc) test fixture. Standard, ASTM International, 2021.

[11]ASTM. D5528m-21, determination of the mode i interlaminar fracture toughness of unidirectional fiber-reinforced polymer matrix composites. Standard, ASTM International, 2022.

[12]ASTM. D6671m-22, standard test method for mixed mode i-mode ii interlaminar fracture toughness of unidirectional fiber reinforced polymer matrix composites. Technical report, ASTM International, 2022.

[13]ASTM. D7291m-22, standard test method for through-thickness "flatwise" tensile strength and elastic modulus of a fiber-reinforced polymer matrix composite material. Technical report, ASTM International, 2022.

[14]A. Bacigalupo and L. Gambarotta. Second-order computational homogenization of heterogeneous materials with periodic microstructure. *ZAMM - Journal of Applied Mathematics and Mechanics / Zeitschrift für Angewandte Mathematik und Mechanik*, 90(10-11):796–811, 2010.

[15]A. H. Baluch, O. Falcó, J. L. Jiménez, B. H. Tijs, and C. S. Lopes. An efficient numerical approach to the prediction of laminate tolerance to barely visible impact damage. *Composite Structures*, 225:111017, 2019.

[16]S. Basu, A. M. Waas, and D. R. Ambur. Compressive failure of fiber composites under multi-axial loading. *Journal of the Mechanics and Physics of Solids*, 54(3):611 – 634, 2006.

[17]A. Bensoussan. *Asymptotic analysis for periodic structures / Alain Bensoussan, Jacques-Louis Lions, George Papanicolaou.* Studies in mathematics and its applications ; 5. North-Holland Pub. Co., Amsterdam ;, 1978.

[18]M. Benzeggagh and M. Kenane. Measurement of mixed-mode delamination fracture toughness of unidirectional glass/epoxy composites with mixed-mode bending apparatus. *Composites science and technology*, 56(4):439–449, 1996.

[19]A. C. Bergan and S. C. Garcea. In-situ observations of longitudinal compression damage in carbon-epoxy cross ply laminates using fast synchrotron radiation computed tomography. Technical report, NASA, 2017.

[20]A. C. Bergan, M. Herráez, C. González, and C. S. Lopes. A constitutive model for fiber kinking: Formulation, finite element implementation, and verification. *Composites Part A: Applied Science and Manufacturing*, 129:105682, 2020.

[21]A. C. Bergan and F. A. Leone. A continuum damage mechanics model to predict kink-band propagation using deformation gradient tensor decomposition. Technical report, NASA, 2016.

[22]A. C. Bergan, S. J. Murphy, and L. F. Miles. Analysis of open hole compression specimens using the compdam continuum damage mechanics model. Technical memorandum, NASA, 2020.

[23]A. C. Bergan and J. C. Wade. Validation of a mesoscale fiber kinking model through test and analysis of double edge notch compression specimens. Technical report, NASA, 2019.

[24]F. Bianchi, T. M. Koh, X. Zhang, I. K. Partridge, and A. P. Mouritz. Finite element modelling of z-pinned composite t-joints. *Composites Science and Technology*, 73:48–56, 11 2012.

[25]F. Bianchi and X. Zhang. A cohesive zone model for predicting delamination suppression in z-pinned laminates. *Composites Science and Technology*, 71(16):1898 – 1907, 2011.

[26]F. Bianchi and X. Zhang. Predicting mode-ii delamination suppression in z-pinned laminates. *Composites Science and Technology*, 72:924–932, 5 2012.

[27]M. Bishara, R. Rolfes, and O. Allix. Revealing complex aspects of compressive failure of polymer composites – part i: Fiber kinking at microscale. *Composite Structures*, 169:105 – 115, 2017. In Honor of Prof. Leissa.

[28]M. Bishara, M. Vogler, and R. Rolfes. Revealing complex aspects of compressive failure of polymer composites - part ii: Failure interactions in multidirectional laminates and validation. *Composite Structures*, 169, 10 2016.

[29]M. Blacklock, M. W. Joosten, K. Pingkarawat, and A. P. Mouritz. Prediction of mode i delamination resistance of z-pinned laminates using the embedded finite element technique. *Composites Part A: Applied Science and Manufacturing*, 91:283 – 291, 2016.

[30]M. J. Bogdanor, S. B. Clay, and C. Oskay. Interacting damage mechanisms in laminated composites subjected to high amplitude fatigue. *Journal of Engineering Mechanics*, 2019.

[31]M. J. Bogdanor and C. Oskay. Prediction of progressive damage and strength of im7/977-3 composites using the eigendeformation-based homogenization approach: Static loading. *Journal of Composite Materials*, 51(10):1455–1472, 2017.

[32]B. Budiansky. Micromechanics. *Computers & Structures*, 16(1):3 – 12, 1983.

[33]B. Budiansky and N. Fleck. Compressive failure of fibre composites. *Journal of the Mechanics and Physics of Solids*, 41(1):183,211, 1993.

[34]D. J. Bull, S. M. Spearing, and I. Sinclair. Observations of damage development from compression-after-impact experiments using ex situ micro-focus computed tomography. *Composites Science and Technology*, 97:106–114, 6 2014.

[35]L. W. Byrd and V. Birman. The estimate of the effect of z-pins on the strain release rate, fracture and fatigue in a composite co-cured z-pinned double cantilever beam. *Composite Structures*, 68:53–63, 4 2005.

[36]P. Camanho, A. Arteiro, A. Melro, G. Catalanotti, and M. Vogler. Three-dimensional invariant-based failure criteria for fibre-reinforced composites. *International Journal of Solids and Structures*, 55:92–107, 2015. Special Issue Computational and Experimental Mechanics of Advanced Materials A workshop held at King Abdullah University of Science and Technology Jeddah, Kingdom of Saudi Arabia July 1-3, 2013.

[37]P. Camanho, M. Bessa, G. Catalanotti, M. Vogler, and R. Rolfes. Modeling the inelastic deformation and fracture of polymer composites – part ii: Smeared crack model. *Mechanics of materials*, 59:36–49, 2013.

[38]P. Camanho and C. Dávila. Mixed-Mode Decohesion Finite Elements for the Simulation of Delamination in Composite Materials. Technical report, NASA, 2002.

[39]P. P. Camanho, C. G. Davila, and M. F. de Moura. Numerical simulation of mixed-mode progressive delamination in composite materials. *Journal of Composite Materials*, 37(16):1415–1438, 2003.

[40]W. J. Cantwell and A. Morton. The impact resistance of composite materials-a review, 2022.

[41]F. Caputo, A. De Luca, and R. Sepe. Numerical study of the structural behaviour of impacted composite laminates subjected to compression load. *Composites Part B: Engineering*, 79:456 – 465, 2015.

[42]D. D. Cartié, B. N. Cox, and N. A. Fleck. Mechanisms of crack bridging by composite and metallic rods. *Composites Part A: Applied Science and Manufacturing*, 35:1325–1336, 11 2004.

[43]D. D. Cartié, M. Troulis, and I. K. Partridge. Delamination of z-pinned carbon fibre reinforced laminates. *Composites Science and Technology*, 66(6):855–861, 2006. Advances in statics and dynamics of delamination.

[44]P. Chang, A. P. Mouritz, and B. N. Cox. Flexural properties of z-pinned laminates. *Composites Part A: Applied Science and Manufacturing*, 38:244–251, 2 2007.

[45]S. Clay, W. Ault, A. Faupel, C. Oskay, P. Knoth, N. N. Shemesh, R. Haj-Ali, U. Breiman, I. Meshi, and O. Shor. Experimental characterization of compression failure mechanism initiation and growth in notched carbon fiber reinforced composite specimens. *Composites Part A: Applied Science and Manufacturing*, 176:107865, 2024.

[46]S. B. Clay and P. M. Knoth. Experimental results of quasi-static testing for calibration and validation of composite progressive damage analysis methods. *Journal of Composite Materials*, 51(10):1333–1353, 2017.

[47]A. Cottone, T. Turetta, and G. Giambanco. Delamination study of through-thickness reinforced composite laminates via two-phase interface model. *Composites Part A: Applied Science and Manufacturing*, 38(9):1985 – 1995, 2007.

[48]B. N. Cox. Snubbing effects in the pullout of a fibrous rod from a laminate. *Mechanics of Advanced Materials and Structures*, 12:85–98, 2005.

[49]R. Crouch and C. Oskay. Symmetric mesomechanical model for failure analysis of heterogeneous materials. *International Journal for Multiscale Computational Engineering*, 8(5):447–461, 2010.

[50]R. D. Crouch, S. B. Clay, and C. Oskay. Experimental and computational investigation of progressive damage accumulation in cfrp composites. *Compos. Part B: Eng.*, 48:59–67, 2013.

[51]R. D. Crouch, C. Oskay, and S. B. Clay. Multiple spatio-temporal scale modeling of composites subjected to cyclic loading. *Comp. Mech.*, 51:93–107, 2013.

[52]H. Cui, Y. Li, S. Koussios, and A. Beukers. Mixed mode cohesive law for z-pinned composite analyses. *Computational Materials Science*, 75:60–68, 2013.

[53]X. Cui, E. Fang, and J. Lua. A discrete crack network toolkit for abaqus for damage and residual strength prediction of laminated composites. *Journal of Composite Materials*, 51(10):1355–1378, 2017.

[54]V. Dantuluri, S. Maiti, P. H. Geubelle, R. Patel, and H. Kilic. Cohesive modeling of delamination in z-pin reinforced composite laminates. *Composites Science and Technology*, 67(3):616–631, 2007.

[55]R. de Borst. Numerical aspects of cohesive-zone models. *Engineering Fracture Mechanics*, 70(14):1743–1757, 2003.

[56]M. de Freitas and L. Reis. Failure mechanisms on composite specimens subjected to compression after impact. *Composite Structures*, 42(4):365–373, 1998. International Workshop on Experimental Techniques in the Analysis of Composite Structures.

[57]L. Dickinson, G. Farley, and M. Hinders. Translaminar reinforced composites: A review. *J. Composites Tech. Res.*, 21:3–15, 01 1999.

[58]G. J. Dvorak and Y. Benveniste. On transformation strains and uniform fields in multiphase elastic media. *Proceedings of the Royal Society of London. Series A: Mathematical and Physical Sciences*, 437(1900):291–310, 1992.

[59]A. Ellison and H. Kim. Computed tomography informed composite damage state model generation. *Journal of Composite Materials*, 52:3523–3538, 10 2018.

[60]A. Faupel, I. Meshi, and C. Oskay. Reduced order multiscale model for compression kink-band failure in composites. *Journal of Composite Materials*, 56(22):3385–3400, 2022.

[61]A. Faupel and C. Oskay. Modeling the compression-after-impact behavior of a z-pinned composite laminate. In *AIAA Scitech 2021 Forum*, 2021.

[62]A. Faupel and C. Oskay. Multiscale modeling of failure mechanisms in multidirectional double-edge notch compression specimens. In *American Society for Composites (ASC) 38th Annual Technical Conference*, September 2023.

[63]A. Faupel and C. Oskay. Computational analysis of the failure mechanisms of a laminated composite in double-edge notch compression configuration. *Composite Structures*, page 118281, 2024.

[64]J. G. Finlay and A. M. Waas. A model for the response of unreinforced and z-pin reinforced composite pi joints. *Composite Structures*, page 118150, 2024.

[65]J. Fish and K. Shek. Multiscale analysis of composite materials and structures. *Composites Science and Technology*, 60(12):2547–2556, 2000.

[66]N. A. Fleck, L. Deng, and B. Budiansky. Prediction of Kink Width in Compressed Fiber Composites. *Journal of Applied Mechanics*, 62(2):329–337, 06 1995.

[67]L. Francesconi and F. Aymerich. *Impact and post-impact behavior of composite laminates reinforced by Z-Pins*, pages 159–167. Springer New York LLC, 2019.

[68]L. Francesconi, G. Loi, and F. Aymerich. Impact and compression-after-impact performance of a thin z-pinned composite laminate. *Journal of Materials Engineering and Performance*, 2023.

[69]M. Geers, R. de Borst, W. Brekelmans, and R. Peerlings. Strain-based transient-gradient damage model for failure analyses. *Computer Methods in Applied Mechanics and Engineering*, 160(1):133–153, 1998.

[70]E. Giannaros, A. Kotzakolios, G. Sotiriadis, and V. Kostopoulos. A multi-stage material model calibration procedure for enhancing numerical solution fidelity in the case of impact loading of composites. *Journal of Composite Materials*, 55:39–56, 1 2021.

[71]E. González, P. Maimí, E. Martín-Santos, A. Soto, P. Cruz, F. Martín de la Escalera, and J. Sainz de Aja. Simulating drop-weight impact and compression after impact tests on composite laminates using conventional shell finite elements. *International Journal of Solids and Structures*, 144-145:230–247, 2018.

[72]M. Grassi and X. Zhang. Finite element analyses of mode i interlaminar delamination in z-fibre reinforced composite laminates. *Composites Science and Technology*, 63(12):1815 – 1832, 2003.

[73]J. Guedes and N. Kikuchi. Preprocessing and postprocessing for materials based on the homogenization method with adaptive finite element methods. *Computer Methods in Applied Mechanics and Engineering*, 83(2):143–198, 1990.

[74]D. Guédra-Degeorges. Recent advances to assess mono- and multi-delaminations behaviour of aerospace composites. *Composites Science and Technology*, 66(6):796 – 806, 2006. Advances in statics and dynamics of delamination.

[75]R. Gutkin, S. Pinho, P. Robinson, and P. Curtis. On the transition from shear-driven fibre compressive failure to fibre kinking in notched cfrp laminates under longitudinal compression. *Composites Science and Technology*, 70(8):1223–1231, 2010.

[76]S. Hallett, B. Green, W. Jiang, and M. Wisnom. An experimental and numerical investigation into the damage mechanisms in notched composites. *Composites Part A: Applied Science and Manufacturing*, 40(5):613–624, 2009.

[77]K. Hauser. 3d rotations. In *Robotic Systems*. University of Illinois, 2020.

[78]R. Healey, N. M. Chowdhury, W. K. Chiu, and J. Wang. Experimental and numerical determination of mode ii fracture toughness of woven composites verified through unidirectional composite test data. *Polymers and Polymer Composites*, 27:557–566, 11 2019.

[79]K. Hoos, E. V. Iarve, M. Braginsky, E. Zhou, and D. H. Mollenhauer. Static strength prediction in laminated composites by using discrete damage modeling. *Journal of composite materials*, 51(10):1473–1492, 2017.

[80]R. Hu and C. Oskay. Nonlocal homogenization model for wave dispersion and attenuation in elastic and viscoelastic periodic layered media. *Journal of applied mechanics*, 84, 2017.

[81]R. Hu and C. Oskay. Multiscale nonlocal effective medium model for in-plane elastic wave dispersion and attenuation in periodic composites. *Journal of the mechanics and physics of solids*, 124:220–243, 2019.

[82]R. Hu, C. Prakash, V. Tomar, M. Harr, I. E. Gunduz, and C. Oskay. Experimentally-validated mesoscale modeling of the coupled mechanical–thermal response of ap–htpb energetic material under dynamic loading. *International Journal of Fracture*, 203:277–298, 1 2017.

[83]T. Hui and C. Oskay. Computational modeling of polyurea-coated composites subjected to blast loads. *J. Compos. Mater.*, 46:2167–2178, 2012.

[84]D. Hull and Y. B. Shi. Damage mechanism characterization in composite damage tolerance investigations. *Composite Structures*, 23(2):99 – 120, 1993.

[85]M. Idiart, H. Moulinec, P. Ponte Castañeda, and P. Suquet. Macroscopic behavior and field fluctuations in viscoplastic composites: Second-order estimates versus full-field simulations. *Journal of the Mechanics and Physics of Solids*, 54(5):1029–1063, 2006.

[86]P. Jelf and N. Fleck. Compression failure mechanisms in unidirectional composites. *Journal of Composite Materials*, 26(18):2706–2726, 1992.

[87]Y. Jiao and J. Fish. Adaptive delamination analysis. *International Journal for Numerical Methods in Engineering*, 104:1008–1037, 12 2015.

[88]R. Joffe, D. Mattsson, J. Modniks, and J. Varna. Compressive failure analysis of non-crimp fabric composites with large out-of-plane misalignment of fiber bundles. *Composites Part A: Applied Science and Manufacturing*, 36(8):1030–1046, 2005. ACMC/SAMPE Conference on Marine Composites (MarComp) 2003.

[89]A. Kaddour and M. Hinton. Input data for test cases used in benchmarking triaxial failure theories of composites. *Journal of Composite Materials*, 46(19-20):2295–2312, 2012.

[90]S. Karmakov, F. Cepero-Mejías, and J. L. Curiel-Sosa. Numerical analysis of the delamination in cfrp laminates: Vcct and xfem assessment. *Composites Part C: Open Access*, 2, 10 2020.

[91]M. Kortschot, P. Beaumont, and M. Ashby. Damage mechanics of composite materials. iii: Prediction of damage growth and notched strength. *Composites Science and Technology*, 40(2):147–165, 1991.

[92]V. Kostopoulos, N. Sarantinos, and S. Tsantzalis. Review of through-the-thickness reinforced z-pinned composites. *Journal of Composites Science*, 4:31, 3 2020.

[93]I. Kowalski. Characterizing tlie tensile stress-strain nonlinearity of polyacrylonitrile-based carbon fibers, 1988.

[94]R. Krueger. An approach to assess delamination propagation simulation capabilities in commercial finite element codes, 2008.

[95]R. Krueger. Development and application of benchmark examples for mixed-mode i/ii quasi-static delamination propagation predictions, 2012.

[96]R. Krueger. A summary of benchmark examples to assess the performance of quasi-static delamination propagation prediction capabilities in finite element codes. *Journal of Composite Materials*, 49:3297–3316, 11 2015.

[97]S. Kyriakides, R. Arseculeratne, E. Perry, and K. Liechti. On the compressive failure of fiber reinforced composites. *International Journal of Solids and Structures*, 32(6):689 – 738, 1995. Time Dependent Problems in Mechanics.

[98]M. Le, H. Bainier, D. Néron, C. Ha-Minh, and P. Ladevèze. On matrix cracking and splits modeling in laminated composites. *Composites Part A: Applied Science and Manufacturing*, 115:294–301, 2018.

[99]J. Lee and C. Soutis. A study on the compressive strength of thick carbon fibre–epoxy laminates. *Composites Science and Technology*, 67(10):2015–2026, 2007.

[100]S. Lin, V. Ranatunga, and A. M. Waas. Experimental study on the panel size effects of the low velocity impact (lvi) and compression after impact (cai) of laminated composites, part ii: Cai. *Composite Structures*, 295, 9 2022.

[101]S. Lin and A. M. Waas. Accelerating computational analyses of low velocity impact and compression after impact of laminated composite materials. *Composite Structures*, 260, 3 2021.

[102]D. Liu, N. Fleck, and M. Sutcliffe. Compressive strength of fibre composites with random fibre waviness. *Journal of the Mechanics and Physics of Solids*, 52(7):1481 – 1505, 2004.

[103]X. Lu, M. Ridha, V. Tan, and T. Tay. Adaptive discrete-smeared crack (a-disc) model for multi-scale progressive damage in composites. *Composites Part A: Applied Science and Manufacturing*, 125:105513, 2019.

[104]K. Macturk, R. Eby, and W. Adams. Characterization of compressive properties of high-performance polymer fibres with a new microcompression apparatus. *Polymer (Guildford)*, 32:1782–1787, 1991.

[105]R. Massabò and B. N. Cox. Unusual characteristics of mixed-mode delamination fracture in the presence of large-scale bridging. *Mechanics of Composite Materials and Structures*, 8:61–80, 2001.

[106]M. McElroy, W. Jackson, R. Olsson, P. Hellström, S. Tsampas, and M. Pankow. Interaction of delaminations and matrix cracks in a cfrp plate, part i: A test method for model validation. *Composites Part A: Applied Science and Manufacturing*, 103:314–326, 12 2017.

[107]A. R. Melro, J. Serra, G. Allegri, and S. R. Hallett. An energy-equivalent bridging map formulation for modelling delamination in through-thickness reinforced composite laminates. *International Journal of Solids and Structures*, 202:153–165, 2020.

[108]A. R. Melro, J. Serra, G. Allegri, and S. R. Hallett. An energy-equivalent bridging map formulation for modelling delamination in through-thickness reinforced composite laminates. *International Journal of Solids and Structures*, 202:153 – 165, 2020.

[109]G. Mohamed, G. Allegri, M. Yasaee, and S. R. Hallett. Cohesive element formulation for z-pin delamination bridging in fibre reinforced laminates. *International Journal of Solids and Structures*, 132-133:232–244, 2 2018.

[110]P. Moran, X. Liu, and C. Shih. Kink band formation and band broadening in fiber composites under compressive loading. *Acta Metallurgica et Materialia*, 43(8):2943 – 2958, 1995.

[111]P. Moran and C. Shih. Kink band propagation and broadening in ductile matrix fiber composites: Experiments and analysis. *International journal of solids and structures*, 35(15):1709–1722, 1998.

[112]A. Mouritz. Compression properties of z-pinned composite laminates. *Composites Science and Technology*, 67(15):3110 – 3120, 2007.

[113]A. Mouritz and T. Koh. Re-evaluation of mode i bridging traction modelling for z-pinned laminates based on experimental analysis. *Composites Part B: Engineering*, 56:797 – 807, 2014.

[114]P. Naghipour, S. M. Arnold, E. J. Pineda, B. Stier, L. Hansen, B. A. Bednarcyk, and A. M. Waas. Multiscale static analysis of notched and unnotched laminates using the generalized method of cells. *Journal of Composite Materials*, 51:1433–1454, 5 2017.

[115]F. Naya, M. Herráez, C. Lopes, C. González, S. V. der Veen, and F. Pons. Computational micromechanics of fiber kinking in unidirectional frp under different environmental conditions. *Composites Science and Technology*, 144:26 – 35, 2017.

[116]M. H. Nguyen and A. M. Waas. Detailed experimental and numerical investigation of single-edge notched tensile cross-ply laminates. *Composite Structures*, 279:114731, 2022.

[117]N. Nguyen and A. M. Waas. A novel mixed-mode cohesive formulation for crack growth analysis. *Composite Structures*, 156:253–262, 11 2016.

[118]D. Nolan, C. Lally, and J. McGarry. Understanding the deformation gradient in abaqus and key guidelines for anisotropic hyperelastic user material subroutines (umats). *Journal of the Mechanical Behavior of Biomedical Materials*, 126:104940, 2022.

[119]R. Olsson. Modelling of impact damage zones in composite laminates for strength after impact. *The Aeronautical Journal (1968)*, 116(1186):1349–1365, 2012.

[120]C. Oskay. Two-level multiscale enrichment methodology for modeling of heterogeneous plates. *International Journal for Numerical Methods in Engineering*, 80(9):1143–1170, 2009.

[121]C. Oskay and J. Fish. Eigendeformation-based reduced order homogenization for failure analysis of heterogeneous materials. *Computer Methods in Applied Mechanics and Engineering*, 196:1216–1243, 2007.

[122]C. Oskay and G. Pal. A multiscale failure model for analysis of thin heterogeneous plates. *Int. J. Damage Mechanics*, 19:575–611, 2010.

[123]C. Oskay, Z. Su, and B. Kapusuzoglu. Discrete eigenseparation-based reduced order homogenization method for failure modeling of composite materials. *Computer Methods in Applied Mechanics and Engineering*, 359:112656, 2020.

[124]B. Paluch. Analysis of geometric imperfections affecting the fibers in unidirectional composites. *Journal of Composite Materials*, 30(4):454–485, 1996.

[125]I. K. Partridge and D. D. Cartié. Delamination resistant laminates by z-fiber® pinning: Part i manufacture and fracture performance. *Composites Part A: Applied Science and Manufacturing*, 36(1):55–64, 2005.

[126]F. Pegorin, K. Pingkarawat, S. Daynes, and A. Mouritz. Influence of z-pin length on the delamination fracture toughness and fatigue resistance of pinned composites. *Composites Part B: Engineering*, 78:298–307, 2015.

[127]F. Pegorin, K. Pingkarawat, S. Daynes, and A. P. Mouritz. Mode ii interlaminar fatigue properties of z-pinned carbon fibre reinforced epoxy composites. *Composites Part A: Applied Science and Manufacturing*, 67:8–15, 12 2014.

[128]F. Pegorin, K. Pingkarawat, and A. P. Mouritz. Mixed-mode i/ii delamination fatigue strengthening of polymer composites using z-pins. *Composites Part B: Engineering*, 123:219–226, 8 2017.

[129]S. Pinho, R. Darvizeh, P. Robinson, C. Schuecker, and P. Camanho. Material and structural response of polymer-matrix fibre-reinforced composites. *Journal of Composite Materials*, 46(19-20):2313–2341, 2012.

[130]S. T. Pinho, P. Robinson, and L. Iannucci. Fracture toughness of the tensile and compressive fibre failure modes in laminated composites. *Composites Science and Technology*, 66:2069–2079, 10 2006.

[131]L. H. Poh and G. Sun. Localizing gradient damage model with decreasing interactions. *International Journal for Numerical Methods in Engineering*, 110(6):503–522, 2017.

[132]P. Prabhakar and A. M. Waas. Micromechanical modeling to determine the compressive strength and failure mode interaction of multidirectional laminates. *Composites. Part A, Applied science and manufacturing*, 50:11–21, 2013.

[133]M. R. Wisnom and F.-K. Chang. Modelling of splitting and delamination in notched cross-ply laminates. *Composites Science and Technology*, 60(15):2849–2856, 2000.

[134]V. Ranatunga and S. B. Clay. Cohesive modeling of damage growth in z-pinned laminates under mode-i loading. *Journal of Composite Materials*, 47(26):3269–3283, 2013.

[135]V. Ranatunga, S. M. Crampton, and S. B. Clay. Assessment of damage tolerance and static residual strength of z-pin reinforced composites. In *AIAA Scitech 2019 Forum*, volume AIAA 2019-1044, STR-08:Composite Interlaminar Enhancement Methods and Modeling I, 2019.

[136]J. R. Reeder and J. R. Crews. Mixed-mode bending method for delamination testing, 1990.

[137]L. Reis and M. Freitas. Damage growth analysis of low velocity impacted composite panels. *Composite Structures*, 38:509–515, 1997.

[138]B. Rosen. Mechanics of composite strengthening. Technical report, NASA, 1965.

[139]K. Rugg, B. Cox, and R. Massabò. Mixed mode delamination of polymer composite laminates reinforced through the thickness by z-fibers. *Composites. Part A, Applied science and manufacturing*, 33(2):177–190, 2002.

[140]E. F. Rybicki and M. F. Kanninen. A finite element calculation of stress intensity factors by a modified crack closure integral. *Engineering Fracture Mechanics*, 9:931–938, 1977.

[141]H. Sam Huang and A. M. Waas. Quasi-static mode ii fracture tests and simulations of z-pinned woven composites. *Engineering Fracture Mechanics*, 126:155–165, 2014.

[142]V. Satopaa, J. Albrecht, D. Irwin, and B. Raghavan. Finding a "kneedle" in a haystack: Detecting knee points in system behavior. In *2011 31st International Conference on Distributed Computing Systems Workshops*, pages 166–171, 2011.

[143]R. Schapery. Prediction of compressive strength and kink bands in composites using a work potential. *International Journal of Solids and Structures*, 32(6):739 – 765, 1995. Time Dependent Problems in Mechanics.

[144]A. Seupel, G. Hütter, and M. Kuna. An efficient fe-implementation of implicit gradient-enhanced damage models to simulate ductile failure. *Engineering Fracture Mechanics*, 199:41 – 60, 2018.

[145]A. H. Shinohara, T. Sato, F. Saito, T. Tomioka, and Y. Arai. A novel method for measuring direct compressive properties of carbon fibres using a micro-mechanical compression tester, 1993.

[146]C. Skamniotis, M. Elliott, and M. Charalambides. On modelling the constitutive and damage behaviour of highly non-linear bio-composites – mesh sensitivity of the viscoplastic-damage law computations. *International journal of plasticity*, 114:40–62, 2019.

[147]A. Soto, E. V. González, P. Maimí, J. A. Mayugo, P. R. Pasquali, and P. P. Camanho. A methodology to simulate low velocity impact and compression after impact in large composite stiffened panels. *Composite Structures*, 204:223–238, 11 2018.

[148]C. Soutis, P. T. Curtis, and N. A. Fleck. Compressive failure of notched carbon fibre composites. *Proceedings: Mathematical and Physical Sciences*, 440(1909):241–256, 1993.

[149]C. Soutis, N. A. Fleck, and P. T. Curtis. Butterworth-heinemann ltd composites, 1991.

[150]P. Sparks and C. Oskay. The method of failure paths for reduced-order computational homogenization. *International Journal for Multiscale Computational Engineering*, 14(5):515–534, 2016.

[151]C. A. Steeves and N. A. Fleck. In-plane properties of composite laminates with through-thickness pin reinforcement. *International Journal of Solids and Structures*, 43(10):3197 – 3212, 2006.

[152]Z. Su and C. Oskay. Mesh size objective fatigue damage propagation in laminated composites using the multiscale discrete damage theory. *Computational Mechanics*, 67(3):969–987, Mar 2021.

[153]Z. Su and C. Oskay. Modeling arbitrarily oriented and reorienting multiscale cracks in composite materials with adaptive multiscale discrete damage theory. *Computational mechanics*, 70(5):1041–1058, 2022.

[154]H. Suemasu, W. Sasaki, T. Ishikawa, and Y. Aoki. A numerical study on compressive behavior of composite plates with multiple circular delaminations considering delamination propagation. *Composites Science and Technology*, 68(12):2562 – 2567, 2008. Deformation and Fracture of Composites: Analytical, Numerical and Experimental Techniques, with regular papers.

[155]H. Suemasu, H. Takahashi, and T. Ishikawa. On failure mechanisms of composite laminates with an open hole subjected to compressive load. *Composites Science and Technology*, 66:634–641, 5 2006.

[156]Q. Sun, H. Guo, G. Zhou, Z. Meng, Z. Chen, H. Kang, S. Keten, and X. Su. Experimental and computational analysis of failure mechanisms in unidirectional carbon fiber reinforced polymer laminates under longitudinal compression loading. *Composite Structures*, 203:335–348, 2018.

[157]X. C. Sun and S. R. Hallett. Barely visible impact damage in scaled composite laminates: Experiments and numerical simulations. *International Journal of Impact Engineering*, 109:178–195, 11 2017.

[158]X. C. Sun and S. R. Hallett. Failure mechanisms and damage evolution of laminated composites under compression after impact (cai): Experimental and numerical study. *Composites Part A: Applied Science and Manufacturing*, 104:41–59, 1 2018.

[159]M. Sutcliffe, S. Lemanski, and A. Scott. Measurement of fibre waviness in industrial composite components. *Composites Science and Technology*, 72(16):2016 – 2023, 2012.

[160]R. D. Sweeting and R. S. Thomson. The effect of thermal mismatch on z-pinned laminated composite structures. *Composite structures*, 66:189–195, 2004.

[161]W. T., P. Minguet, B. Flynn, D. Carbery, G. Swanson, and L. Ilcewicz. Advanced technology composite fuselage-structural performance advanced technology composite fuselage-structural performance advanced technology composite fuselage-structural performance. Technical report, NASA, 1997.

[162]J. Tan, V. Deshpande, and N. Fleck. Failure mechanisms of a notched cfrp laminate under multi-axial loading. *Composites Part A: Applied Science and Manufacturing*, 77:56–66, 2015.

[163]W. Tan, B. G. Falzon, L. N. Chiu, and M. Price. Predicting low velocity impact damage and compression-after-impact (cai) behaviour of composite laminates. *Composites Part A: Applied Science and Manufacturing*, 71:212–226, 2015.

[164]J. Toral Vazquez, B. Castanié, J.-J. Barrau, and N. Swiergiel. Multi-level analysis of low-cost z-pinned composite joints: Part 2: Joint behaviour. *Composites Part A: Applied Science and Manufacturing*, 42(12):2082–2092, 2011.

[165]A. Turon, P. P. Camanho, J. Costa, and J. Renart. Accurate simulation of delamination growth under mixed-mode loading using cohesive elements: Definition of interlaminar strengths and elastic stiffness. *Composite Structures*, 92:1857–1864, 7 2010.

[166]A. Turon, C. G. Dávila, P. P. Camanho, and J. Costa. An engineering solution for mesh size effects in the simulation of delamination using cohesive zone models. *Engineering Fracture Mechanics*, 74:1665–1682, 7 2007.

[167]F. van der Meer, C. Oliver, and L. Sluys. Computational analysis of progressive failure in a notched laminate including shear nonlinearity and fiber failure. *Composites Science and Technology*, 70(4):692–700, 2010.

[168]L. L. Vignoli, M. A. Savi, P. M. Pacheco, and A. L. Kalamkarov. Micromechanical analysis of longitudinal and shear strength of composite laminae. *Journal of Composite Materials*, 54:4853–4873, 12 2020.

[169]T. Vogler, S.-Y. Hsu, and S. Kyriakides. On the initiation and growth of kink bands in fiber composites. part ii: analysis. *International Journal of Solids and Structures*, 38(15):2653,2682, 2001.

[170]T. Vogler and S. Kyriakides. Initiation and axial propagation of kink bands in fiber composites. *Acta Materialia*, 45(6):2443 – 2454, 1997.

[171]A. M. Waas, C. D. Babcock, and W. G. Knauss. An experimental study of compression failure of fibrous laminated composites in the presence of stress gradients. *International journal of solids and structures*, 26:1071–1098, 1990.

[172]S. M. Wallentine and M. D. Uchic. A study on ground truth data for impact damaged polymer matrix composites. In *AIP Conference Proceedings*, volume 1949. American Institute of Physics Inc., 4 2018.

[173]Y. Wang, T. L. Burnett, Y. Chai, C. Soutis, P. J. Hogg, and P. J. Withers. X-ray computed tomography study of kink bands in unidirectional composites. *Composite Structures*, 160:917 – 924, 2017.

[174]D. Wilhelmsson, R. Talreja, R. Gutkin, and L. Asp. Compressive strength assessment of fibre composites based on a defect severity model. *Composites Science and Technology*, 181:107685, 2019.

[175]M. R. Wisnom, S. R. Hallett, and C. Soutis. Scaling effects in notched composites. *Journal of Composite Materials*, 44:195–210, 1 2010.

[176]S. Xie, J. Zhang, Z.-S. Guo, and H. Hu. Prediction of compressive strength of z-pinned unidirectional composite laminates. *Journal of Composite Materials*, 46(4):383–390, 2012.

[177]H. Yan, C. Oskay, A. Krishnan, and L. R. Xu. Compression-after-impact response of woven fiber-reinforced composites. *Composites Science and Technology*, 70:2128–2136, 11 2010.

[178]H. Yan, C. Oskay, A. Krishnan, and L. R. Xu. Compression-after-impact response of woven fiber-reinforced composites. *Composites Science and Technology*, 70(14):2128 – 2136, 2010.

[179]M. Yasaee, J. Lander, G. Allegri, and S. Hallett. Experimental characterisation of mixed mode traction–displacement relationships for a single carbon composite z-pin. *Composites Science and Technology*, 94:123–131, 2014.

[180]C. Yerramalli and A. Waas. The effect of fiber diameter on the compressive strength of composites - a 3d finite element based study. *Computer Modeling in Engineering and Sciences*, 6:1–16, 01 2004.

[181]B. Zhang, G. Allegri, M. Yasaee, and S. Hallett. Micro-mechanical finite element analysis of z-pins under mixed-mode loading. *Composites Part A: Applied Science and Manufacturing*, 78:424 – 435, 2015.

[182]H. Zhang, K. Cho, C. F. Yen, and K. Ravi-Chandar. Dynamic crushing of unidirectionally reinforced metal matrix composite. *Strain*, 50(6):517–526, 2014.

[183]S. Zhang and C. Oskay. Reduced order variational multiscale enrichment method for thermo-mechanical problems. *Computational mechanics*, 59:887–907, 2017.

[184]X. Zhang, L. Hounslow, and M. Grassi. Improvement of low-velocity impact and compression-after-impact performance by z-fibre pinning, 2006.

[185]X. Zhang and C. Oskay. Eigenstrain based reduced order homogenization for polycrystalline materials. *Computer Methods in Applied Mechanics and Engineering*, 297:408 – 436, 2015.

[186]S. Zhou, Y. Sun, B. Chen, and T.-E. Tay. Progressive damage simulation of open-hole composite laminates under compression based on different failure criteria. *Journal of Composite Materials*, 51(9):1239–1251, 2017.